

THE SYNTHESIS AND CHARACTERIZATION OF
DOXORUBICIN AND BORTEZOMIB LOADED MAGNETIC NANOPARTICLES FOR
TARGETING TUMOR CELLS

A THESIS SUBMITTED TO
THE GRADUATE SCHOOL OF NATURAL AND APPLIED SCIENCES
OF
MIDDLE EAST TECHNICAL UNIVERSITY

BY

GÖZDE ÜNSOY

IN PARTIAL FULFILLMENT OF THE REQUIREMENTS
FOR
THE DEGREE OF DOCTOR OF PHILOSOPHY
IN
BIOTECHNOLOGY

SEPTEMBER, 2013

Approval of the thesis:

**THE SYNTHESIS AND CHARACTERIZATION OF
DOXORUBICIN AND BORTEZOMIB LOADED MAGNETIC NANOPARTICLES
FOR TARGETING TUMOR CELLS**

submitted by **GÖZDE ÜNSOY** in partial fulfillment of the requirements for the degree of
Doctor of Philosophy in Department of Biotechnology, Middle East Technical University
by,

Prof. Dr. Canan Özgen
Dean, Graduate School of Natural and Applied Sciences _____

Prof. Dr. Nesrin Hasırcı
Head of Department, **Biotechnology** _____

Prof. Dr. Ufuk Gündüz
Supervisor, **Department of Biotechnology, METU** _____

Assoc. Prof. Dr. Güven Gürer Budak
Co-Supervisor, **Nanomedicine Center, Gazi University** _____

Examining Committee Members:

Assoc. Prof. Dr. Sreeparna Banerjee
Department of Biotechnology, METU _____

Prof. Dr. Ufuk Gündüz
Department of Biotechnology, METU _____

Assoc. Prof. Dr. Ayşen Tezcaner
Department of Engineering Sciences, METU _____

Assoc. Prof. Dr. Çağdaş Son
Department of Biological Sciences, METU _____

Assoc. Prof. Dr. Bora Maviş
Dept. of Mechanical Engineering, Hacettepe University _____

Date: 4th September 2013

I hereby declare that all information in this document has been obtained and presented in accordance with academic rules and ethical conduct. I also declare that, as required by these rules and conduct, I have fully cited and referenced all material and results that are not original to this work.

Name,Lastname: Gözde ÜNSOY

Signature:

ABSTRACT

THE SYNTHESIS AND CHARACTERIZATION OF DOXORUBICIN AND BORTEZOMIB LOADED MAGNETIC NANOPARTICLES FOR TARGETING TUMOR CELLS

ÜNSOY, Gözde

Ph.D., Department of Biotechnology

Supervisor: Prof. Dr. Ufuk GÜNDÜZ

Co-Supervisor: Assoc. Prof. Dr. Güven Gürer BUDAK

September 2013, 128 pages

Chitosan superparamagnetic nanoparticles, loaded with Doxorubicin and Bortezomib were synthesized for treatment of breast and cervical cancers by targeted drug delivery. *In vitro* cytotoxicity analyses revealed that the efficacy of drugs was highly increased when applied as loaded on nanoparticles.

Chitosan superparamagnetic iron oxide nanoparticles (CSMNPs) were in-situ synthesized at different sizes by ionic crosslinking method. The characterization of nanoparticles was performed by XRD, XPS/ESCA, FTIR, TEM, DLS, TGA, VSM and zeta potential analyses. The XRD and XPS analyses proved that synthesized iron-oxide was magnetite (Fe_3O_4). Chitosan coating on the surface of magnetite was confirmed by FTIR. Average core size of CSMNPs were between 2-8 nm in TEM and hydrodynamic diameters were between 58-103 nm in DLS. TEM results demonstrated a spherical morphology. TGA results indicated that chitosan content of CSMNPs were between 15-23%. CSMNPs were found superparamagnetic by VSM analyses. The cellular uptake of nanoparticles was visualized by fluorescence microscopy and cytotoxicity was determined by XTT analyses on MCF-7, MCF-7/Dox, SiHa and HeLa cell lines. Doxorubicin and Bortezomib loading, release and stability efficiencies of CSMNPs were analyzed by considering the different parameters.

CSMNPs are not cytotoxic without the drug load. When these drugs are loaded on CSMNPs, the antiproliferative efficiencies of drugs increases and resistance to these drugs is eliminated. IC_{50} values of drugs remarkably decreases when the drugs are given to the cells as loaded on CSMNPs. Proapoptotic *Puma* and *Noxa* genes were up regulated while antiapoptotic *Bcl-2*, *Survivin* and *cIAP-2* genes were down regulated in drug loaded CSMNP treated cells. Consequently, CSMNPs synthesized at various sizes would be effectively used for the pH dependent release of Doxorubicin and Bortezomib. Results of this study can provide new insights in the development of pH responsive magnetic targeted drug delivery systems to overcome the side effects and resistance problem of conventional chemotherapy.

Keywords: Targeted Drug Delivery, Magnetic Nanoparticle, Chitosan, Bortezomib, Doxorubicin.

ÖZ

KANSER HÜCRELERİNİN HEDEFLENMESİ İÇİN DOKSORUBİSİN VE BORTEZOMİB YÜKLÜ MANYETİK NANOPARÇACIKLARIN SENTEZLENMESİ VE KARAKTERİZASYONU

ÜNSOY, Gözde
Doktora, Biyoteknoloji Bölümü
Tez Yöneticisi: Prof. Dr. Ufuk GÜNDÜZ
Ortak Tez Yöneticisi: Doç. Dr. Güven Gürer BUDAK

Eylül 2013, 128 sayfa

Hedeflenmiş ilaç salımı ile meme ve rahim ağzı kanserlerinin tedavisinde kullanılmak üzere, Doksorubisin ve Bortezomib yüklü kitosan manyetik nanoparçacıklar sentezlendi. Farklı boyutlardaki kitosan superparamanyetikdemir oksit nanoparçacıklar (CS MNP-S_{1,2,3,4}) aynı anda iyonik çaprazbağlama metodu ile sentezlendi. Nanoparçacıkların karakterizasyonu XRD, XPS/ESCA, FTIR, TEM, DLS, TGA, VSM ve zeta potansiyel analizleri ile yapıldı. XRD ve XPS analizleri sentezlenen demir oksit nanoparçacıkların manyetit (Fe₃O₄) olduğunu kanıtladı. Manyetit çekirdek üzerindeki kitosan kaplamanın varlığı FTIR analizi ile doğrulandı. TEM analizinde CS MNP'lerin küresel yapıda oldukları ve manyetit çekirdeklerin çaplarının 2-8 nm aralığında olduğu gözlemlendi. DLS analizinde CS MNP'lerin hidrodinamik çapları 58-103 nm aralığında ölçüldü. TGA sonuçları CS MNP'lerin % 15-23 arasında kitosan içerdiğini ispatladı. CS MNP'lerin superparamanyetik özellikte oldukları VSM ile bulundu. Nanoparçacıkların hücre içine alımları MCF-7, MCF-7/Dox, SiHa ve HeLa hücre hatlarında florasan mikroskobu ile gözlemlendi ve sitotoksosite analizleri XTT ile belirlendi. CS MNP'lere Doxorubicin ve Bortezomib ilaçları yüklenerek, farklı koşullardaki stabilite ve ilaç salım hızları belirlendi.

İlaç yüklü CS MNP'ler hücrelere verildikleri zaman, ilacın tesirinin önemli ölçüde arttığı ve IC₅₀ değerlerinin kayda değer ölçüde azaldığı *in vitro* sitotoksosite analizleri ile tespit edildi. İlaçlar CS MNP'ler üzerine yüklendiğinde, dirençliliğin engellendiği ve ilacın hücre çoğalmasını önleme etkinliğinin arttığı belirlendi. Bununla birlikte, ilaçsız CS MNP'lerin sitotoksik etkilerinin olmadığı görüldü. Hücrelere ilaç yüklü CS MNP'ler verildiğinde antiapoptotik *Bcl-2*, *Survivin* ve *cIAP-2* gen ifadeleri azalırken, apoptotik *Puma* ve *Noxa* gen ifadelerinde belirgin bir artış olduğu saptandı. Sonuçlar, sentezlenen Doxorubicin ve Bortezomib yüklü CS MNP'lerin kanser tedavisinde ilaçların hedefli salımı uygulamalarında kullanılabilecek özellikte olduklarını gösterdi.

Anahtar Kelimeler: Hedeflenmiş İlaç Salımı, Manyetik Nanoparçacık, Kitosan, Bortezomib, Doxorubicin.

*To my valuable parents Güneş Baydar & Zeki Baydar,
beloved husband Ali Erdoğan Ünsoy, and precious son Mehmet Görkem Ünsoy.*

ACKNOWLEDGEMENTS

First of all, I would like to express my deepest gratitude to my supervisor Prof. Dr. Ufuk Gündüz for her great academic guidance, advices, support and encouragement throughout this study. I feel great appreciation to Prof. Dr. Güngör Gündüz for his valuable contributions and support. I also thank to my co-supervisor Assoc. Prof. Dr. Güven Gürer Budak for his support and encouragement in this research.

I would like to thank Assoc. Prof. Dr. Bora Maviş for his valuable support in FTIR analysis. Examining committee members Assoc. Prof. Dr. Sreeparna Banerjee, Assoc. Prof. Dr. Ayşen Tezcaner and Assoc. Prof. Dr. Çağdaş Son are also greatly acknowledged for their kind participation and valuable comments during this research.

I am grateful to Rouhollah Khodadust, Serap Yalçın and Pelin Mutlu for their friendship, kind and pleasant collaboration in this study.

Aktan Alpsoy, Tuğba Keskin, Gülistan Tansık, Murat Erdem, Çağrı Urfalı, Neşe Çakmak, Negar Taghavi, Maryam Parsian, Esra Kaplan, Arzu Yakar, other members of Lab 206 and also our special project students are greatly acknowledged for their friendship and contributions throughout my study.

I would like to express my great appreciation to my mother Güneş Baydar and father Zeki Baydar for their endless love, trust and support in every step of my life.

I would like to express my special thanks to my dear husband Ali Erdoğan Ünsoy for his endless love, support and encouragement; also to my lovely son Mehmet Görkem Ünsoy for his precious existence in our life.

This study was supported by the research fund of TÜBİTAK Grant No: TBAG-109T949 and METU Research Foundation Project Grant No: BAP-07-02-2010-06, BAP-07-02-2012-001, BAP-08-11-2012-012, BAP-08-11-2013-018.

In addition, Janssen & Cilag is acknowledged for providing Bortezomib in my project.

TABLE OF CONTENTS

ABSTRACT	v
ÖZ.....	vi
ACKNOWLEDGEMENTS.....	viii
TABLE OF CONTENTS.....	ix
LIST OF FIGURES.....	xiii
LIST OF TABLES.....	xviii
CHAPTERS	
1. INTRODUCTION.....	1
1.1. Cancer	1
1.1.1. Breast Cancer.....	1
1.1.2. Cervical Cancer	3
1.2. Cancer Chemotherapeutics	6
1.2.1. Doxorubicin (Adriamycin®)	6
1.2.2. Bortezomib (Velcade®).....	9
1.3. Targeted Drug Delivery Systems.....	12
1.3.1. Magnetic Nanoparticles in Targeted Drug Delivery	14
1.3.2. Chitosan as Surface Coating Material	19
1.3.3. Chitosan for Surface Coating of Magnetic Nanoparticles	21
1.3.4. Cellular Uptake of Nanoparticles	22
1.3.5. Toxicity of Nanoparticles	23
2. MATERIALS AND METHODS.....	25
2.1. Materials	25
2.2. Methods	26
2.2.1 Synthesis of Bare Magnetic Nanoparticles (MNPs)	26
2.2.2 In Situ Synthesis of Chitosan coated Magnetic Nanoparticles	27
2.2.3 Characterization of Bare and Chitosan Magnetic Nanoparticles.....	29
2.2.3.1 X-Ray Diffraction (XRD)	29
2.2.3.2 X-Ray Photoelectron Spectroscopy (XPS, ESCA)	29

2.2.3.3	Fourier Transform Infrared (FTIR) Spectroscopy	30
2.2.3.4	Transmission Electron Microscopy (TEM)	30
2.2.3.5	Freeze Drying	30
2.2.3.6	Scanning Electron Microscopy (SEM)	30
2.2.3.7	Dynamic Light Scattering (DLS)	30
2.2.3.8	Zeta (ζ) Potential	31
2.2.3.9	Vibrating Sample Magnetometer (VSM)	31
2.2.3.10	Cellular Uptake of FITC Modified CS MNPs	31
2.2.3.11	Cytotoxicity of Bare and CS MNPs	31
2.2.4	Drug Loading, Release and Stability of CS MNPs	31
2.2.4.1	Doxorubicin Loading	32
2.2.4.1.1	Loading of Doxorubicin on CS MNPs	32
2.2.4.1.1	Stability of Doxorubicin loaded CS MNPs	33
2.2.4.1.2	Release of Doxorubicin from CS MNPs	34
2.2.4.1.3	Cellular Uptake of Doxorubicin Loaded CS MNPs	34
2.2.4.1.4	Cytotoxicity of Doxorubicin loaded CS MNPs	34
2.2.4.2	Bortezomib Loading	34
2.2.4.2.1	Loading of Bortezomib on CS MNPs	34
2.2.4.2.2	Stability of Bortezomib on CS MNPs	35
2.2.4.2.3	Release of Bortezomib from CS MNPs	36
2.2.4.2.4	Cytotoxicity of Bortezomib loaded CS MNPs	36
2.2.5	Cell Culture	36
2.2.5.1	Cell Lines and Culture Conditions	36
2.2.5.2	Harvesting Cells and Subculturing	37
2.2.5.3	Freezing Cells and Thawing Frozen Cells	37
2.2.6	Cell Proliferation Assays	38
2.2.6.1	Viable Cell Counting	38
2.2.6.2	Cell Proliferation Assay with XTT Reagent	38
2.2.6.3	Statistical Analysis	39
2.2.7	Effect of Drug Loaded CS MNPs on Apoptotic Gene Expressions	39
2.2.7.1	Isolation of Total RNA	40
2.2.7.2	Quantification of the Isolated RNA	40
2.2.7.3	Agarose Gel Electrophoresis of RNA	40

2.2.7.4	DNase Treatment of RNA	41
2.2.7.5	cDNA Synthesis	41
2.2.7.6	Quantitative Real-Time Polymerase Chain Reaction (qPCR).....	41
3.	RESULTS AND DISCUSSION.....	43
3.1.	Characterization of Bare and CS MNPs.....	43
3.1.1.	X-Ray Diffraction (XRD).....	44
3.1.2.	X-Ray Photoelectron (XPS)	46
3.1.3.	Fourier transform infrared spectroscopy (FTIR)	48
3.1.4.	Transmission Electron Microscopy (TEM)	49
3.1.5.	Freeze Drying of CS MNPs.....	52
3.1.6.	Scanning Electron Microscopy (SEM).....	52
3.1.7.	Dynamic Light Scattering (DLS)	55
3.1.8.	Zeta (ζ) Potential	59
3.1.9.	Vibrating Sample Magnetometer (VSM)	60
3.1.10.	Thermogravimetric Analysis (TGA and TGA-FTIR)	61
3.1.11.	Cellular Uptake of Fluorescent Modified CS MNPs	62
3.1.12.	Cytotoxicity of Bare and CS MNPs	63
3.2.	Drug Loading, Release, Stability, Cellular Uptake and Cytotoxicity of CS MNPs	66
3.3.1.	Doxorubicin	67
3.2.1.1.	Standard curve of Doxorubicin	67
3.2.1.2.	Doxorubicin Loading on CS MNPs	67
3.2.1.3.	FTIR Analyses of Doxorubicin Loaded CS MNPs	69
3.2.1.4.	Stability of Doxorubicin loaded CS MNPs	70
3.2.1.5.	Doxorubicin Release From CS MNPs.....	71
3.2.1.6.	Cellular Uptake of Doxorubicin-loaded Nanoparticles	74
3.2.1.7.	Cytotoxicity Analyses of Doxorubicin Loaded CS MNPs.....	77
3.3.2.	Bortezomib Loading on CS MNPs	80
3.2.2.1.	Standard curve of Bortezomib	80
3.2.2.2.	Bortezomib Loading on Synthesized CS MNPs	80
3.2.2.3.	FTIR Analyses of Bortezomib Loaded CS MNPs	85
3.2.2.4.	Stability of Bortezomib Loaded Nanoparticles	86
3.2.2.5.	Bortezomib Release From the Nanoparticles	87
3.2.2.6.	Cellular Uptake of Bortezomib Loaded CS MNPs	88

3.2.2.7. Cell Proliferation Assay With XTT Reagent	90
3.3. Effect of Drug Loaded CS MNPs on Apoptotic Gene Expressions	94
3.3.1. Expression Levels of Doxorubicin CS MNP Treated Breast Cancer Cells.....	95
3.3.2. Expression Levels of Bortezomib CS MNP Treated Cervical Cancer Cells	97
4. CONCLUSIONS	99
REFERENCES.....	103
CIRRICULUM VITAE.....	123

LIST OF FIGURES

FIGURES

Figure 1.1. Breast cancer types and pathogenesis. (2012-2013 McMaster Pathophysiology Review (MPR) http://www.pathophys.org/breast-cancer/).....	2
Figure 1.2. HPV-mediated progression to cervical cancer. (Woodman <i>et al.</i> , 2007).	4
Figure 1.3. Doxorubicin (Pajeva <i>et al.</i> , 2004).	6
Figure 1.4. Cell death mechanisms of anthracyclines (Chabner and Longo <i>et al.</i> , 2005).....	7
Figure 1.5. Bortezomib (Chen <i>et al.</i> , 2011).	9
Figure 1.6. The proteasome inhibitor, Bortezomib. (Paramore and Frantz, 2003).	10
Figure 1.7. Apoptosis induction by DR results in the activation of extrinsic and intrinsic apoptotic pathways. (Hougardy <i>et al.</i> ,2005).	11
Figure 1.8. Schematic representation of functionalized, polymer coated magnetic (iron oxide) nanoparticles (Sun <i>et al.</i> ,2008).	13
Figure 1.9. Passive and active targeting. (Zhao <i>et al.</i> , 2012).	14
Figure 1.10. Anti-cancer drug loaded nanoparticles are magnetically guided with intravenous administration of magnetic nanoparticles (Biophan Technologies, 2013).	16
Figure 1.11. Active Magnetic Drug Targeting (MDT) magnetic drug carriers disintegrate in the target zone and release the drug (Bakarat <i>et al.</i> ,2009).	17
Figure 1.12. Schematic representation of tissue specific delivery of superparamagnetic MNPs (Park <i>et al.</i> , 2010).	18
Figure 1.13. Chitosan (Molecular formula; C ₆ H ₁₁ NO ₄).	20
Figure 1.14. Schema showing the interaction between the chitosan and the crosslinker, TPP molecules.	21
Figure 1.15. Schematic representation of the cellular uptake and drug release from chitosan nanoparticles. (Park <i>et al.</i> , 2010).	23
Figure 1.16. Diagram showing evolution of blood residence time with particle size (Macaroff <i>et al.</i> , 2006).	24

Figure 2.1. The scheme of the experimental setup for Bare MNP synthesis (Keskin, 2012).	26
Figure 2.2. The scheme of the experimental setup for CS MNP synthesis (Keskin, 2012)..	27
Figure 2.3. pH effect on ionotropic cross-linking and deprotonation (Pati <i>et al.</i> , 2011).....	28
Figure 2.4. Chemical structures of Doxorubicin (a) and Bortezomib (b).....	32
Figure 2.5. Schematic representation of Doxorubicin loaded CS MNPs.	33
Figure 2.6. Schematic representation of Bortezomib loaded CS MNPs.	35
Figure 2.7. Schematic representation of XTT cell proliferation design on 96 well plate.....	39
Figure 3.1. XRD patterns of Fe ₃ O ₄ nanoparticles synthesized at different tempratures.	44
Figure 3.2. XRD patterns of bare and chitosan coated magnetic nanoparticles.....	44
Figure 3.3. X-ray photoelectron spectra of the synthesized magnetic nanoparticles.	47
Figure 3.4. FTIR spectra of the chitosan and synthesized magnetic nanoparticles.....	48
Figure 3.5. TEM images of synthesized bare magnetic nanoparticles.	49
Figure 3.6. TEM images of synthesized chitosan coated magnetic nanoparticles	50
Figure 3.7. Particle size distribution graph of CS MNPs according to TEM images.....	52
Figure 3.8. SEM images of synthesized bare MNPs.....	53
Figure 3.9. DLS diagrams of synthesized chitosan coated MNPs	56
Figure 3.10. Particle size distribution of CS MNPs according to DLS results.	58
Figure 3.11. DLS diagrams of synthesized bare MNPs shows that the average diameter of particles is 18 nm.	58
Figure 3.12. Zeta potential measurements of CS MNPs (a) and bare MNPs (b).	59
Figure 3.13. Magnetization graph of chitosan coated MNPs (S1-S4).....	60
Figure 3.14. The hysteresis curve of bare and chitosan coated MNPs.....	60
Figure 3.15. Thermal gravimetric analysis curve of bare and chitosan coated MNPs.	61
Figure 3.16. Cellular uptake of florescent CS MNP-S ₁ by MCF-7 cells.....	62

Figure 3.17. Cell proliferation vs MNP concentration graphs of bare (a) and chitosan coated MNP-S ₁ (b) on HeLa cells.	63
Figure 3.18. Cell proliferation vs MNP concentration graphs of bare (a) and chitosan coated MNP-S ₁ (b) on SiHa cells.	64
Figure 3.19. Cell proliferation vs MNP concentration graphs of bare (a) and chitosan coated MNP-S ₁ (b) on MCF-7 cells.	65
Figure 3.20. Cell proliferation vs MNP concentration graphs of bare (a) and chitosan coated MNP-S ₁ (b) on MCF-7/Dox cells.	66
Figure 3.21. Standard curve of Doxorubicin at 481 nm.	67
Figure 3.22. Doxorubicin loading efficiency on CS MNP-S ₁ nanoparticles.	68
Figure 3.23. Doxorubicin loading efficiency on CS MNP-S ₁ , S ₂ , S ₃ and S ₄	69
Figure 3.24. FTIR spectra of CS (a), CS MNP-S ₁ (b), Doxorubicin loaded CS MNP-S ₁ (c) and Doxorubicin (d).	70
Figure 3.25. Stability of Doxorubicin (400 - 500 µg/ml) loaded CS MNP-S ₁ and CS MNP-S ₄ in phosphate buffer (pH=7.4) up to 8 weeks.	71
Figure 3.26. Doxorubicin release graph of CS MNP-S ₄ nanoparticles at pH 4.2 and 5.0 with (a) 400 and (b) 500 µg/ml initial loading concentrations.	72
Figure 3.27. Doxorubicin release graph of CS MNP-S ₁ nanoparticles at pH 4.2 and 5.0 with (a) 400 and (b) µg/ml initial loading concentrations.	73
Figure 3.28. Fluorescent microscopy images of MCF-7/S cells treated with Doxorubicin loaded CS MNP-S ₁ nanoparticles obtained (a) at red filter, and (b) green filter.	75
Figure 3.29. Fluorescent microscopy images of MCF-7/S cells and MCF-7/Dox (1µM) resistant cells treated with Doxorubicin loaded CS MNP-S ₁	76
Figure 3.30. Cell proliferation profiles of MCF-7 cells after exposure to increasing concentrations of Doxorubicin loaded CS MNPs (IC ₅₀ =1,05µM).	78
Figure 3.31. The comparison graph of IC ₅₀ values of free Doxorubicin and Doxorubicin loaded CS MNPs on MCF-7.	78
Figure 3.32. Cell proliferation profiles of MCF-7/Dox cells after exposure to increasing concentrations of Doxorubicin loaded CS MNPs (IC ₅₀ =13,5µM).	79

Figure 3.33. The comparison graph of IC ₅₀ values of free Doxorubicin and Doxorubicin loaded CS MNPs on MCF-7/Dox.	79
Figure 3.34. Standard curve of Bortezomib obtained by spectrophotometric measurements of known drug concentrations at 270 nm.	80
Figure 3.35. Bortezomib concentration vs loading efficiency graph at Acetate Buffer.	81
Figure 3.36. Bortezomib concentration vs loading efficiency graph at PBS Buffer.	82
Figure 3.37. Bortezomib concentration vs loading efficiency graph at Acetate Buffer.	82
Figure 3.38. Bortezomib concentration vs loading efficiency at Phosphate Buffer.	83
Figure 3.39. Loading efficiency was optimized with various loading buffers.	84
Figure 3.40. FTIR analyses of chitosan coated magnetic nanoparticles, Bortezomib and Bortezomib loaded chitosan coated magnetic nanoparticles.	85
Figure 3.41. Stability of Bortezomib loaded CS MNP-S ₁ in PBS buffer (pH7.4)	86
Figure 3.42. Bortezomib release graph of S ₁ and S ₄ nanoparticles at pH 4.2 and 5.0 with 400 µg/ml initial loading concentrations.	87
Figure 3.43. Cellular uptake images of Bortezomib loaded CS MNP-S ₁ nanoparticles, applied on SiHa and HeLa cells	89
Figure 3.44. Cell proliferation profiles of SiHa (IC ₅₀ = 40 nM) cells after exposure to increasing concentrations of Bortezomib.	91
Figure 3.45. Cell proliferation profiles of SiHa (IC ₅₀ = 3 nM) cells after exposure to increasing concentrations of Bortezomib loaded CS MNPs.	91
Figure 3.46. The comparison graph of IC ₅₀ values of free Bortezomib and Bortezomib loaded CS MNPs on SiHa cells.	92
Figure 3.47. Cell proliferation profiles of HeLa (IC ₅₀ = 6 µM) cells after exposure to increasing concentrations of Bortezomib.	92
Figure 3.48. Cell proliferation profiles of HeLa (IC ₅₀ = 3,5 µM) cells after exposure to increasing concentrations of Bortezomib loaded CS MNPs.	93
Figure 3.49. The comparison graph of IC ₅₀ values of free Bortezomib and Bortezomib loaded CS MNPs on HeLa cells.	93

Figure 3.50. The expression levels of antiapoptotic (<i>Bcl-2</i> , <i>Survivin</i> and <i>cIAP-2</i>) and apoptotic (<i>Puma</i> and <i>Noxa</i>) genes at untreated control cells, and free Doxorubicin, empty CS MNP and Doxorubicin loaded CS MNP treated MCF-7 cells.....	95
Figure 3.51. The expression levels of antiapoptotic (<i>Bcl-2</i> , <i>Survivin</i> and <i>cIAP-2</i>) and apoptotic (<i>Puma</i> and <i>Noxa</i>) genes at untreated control cells, and free Doxorubicin, empty CS MNP and Doxorubicin loaded CS MNP treated MCF-7/Dox cells.....	96
Figure 3.52. The expression levels of antiapoptotic (<i>Bcl-2</i> , <i>Survivin</i> and <i>cIAP-2</i>) and apoptotic (<i>Puma</i> and <i>Noxa</i>) genes at untreated control cells, and free Bortezomib, empty CS MNP and Bortezomib loaded CS MNP treated SiHa cells.....	97
Figure 3.53. The expression levels of antiapoptotic (<i>Bcl-2</i> , <i>Survivin</i> and <i>cIAP-2</i>) and apoptotic (<i>Puma</i> and <i>Noxa</i>) genes at untreated control cells, and free Bortezomib, empty CS MNP and Bortezomib loaded CS MNP treated HeLa cells.....	98

LIST OF TABLES

TABLES

Table 2.1. PCR conditions of <i>β-actin</i> , <i>Bcl-2</i> , <i>Survivin</i> , <i>cIAP-2</i> , <i>Puma</i> and <i>Noxa</i> genes..	42
Table 2.2. Primers of <i>β-actin</i> , <i>Bcl-2</i> , <i>Survivin</i> , <i>cIAP-2</i> , <i>Puma</i> and <i>Noxa</i> genes..	42
Table 3.1. Loaded amounts and loading efficiencies of Doxorubicin on CS MNP-S1 at different concentrations (150-600 µg/ml).	68
Table 3.2. Bortezomib loading efficiencies on CS MNP nanoparticles.	84

CHAPTER 1

INTRODUCTION

1.1. Cancer

Regulation of cell cycle is a key mechanism for the maintenance of homeostasis of normal cell growth and viability, and this is a very tightly controlled process. However, deregulation of cell cycle is well known to contribute to tumor development (Maya-Mendoza *et al.*, 2009). Cancer is a disease arises from the uncontrolled growth and spread of transformed cells. The transformation of a healthy cell into a tumor cell is a multistage process similar to the progression of a benign lesion to a malignant tumor. Cancer is one of the most deadly diseases in the world and the number of new cases increases everyday (Boyle *et al.*, 2008). Despite the advances in treatments, the overall survival rate from cancer has not improved substantially over the past 30 years (Jemal *et al.*, 2010).

There is a need to develop novel approaches for therapies based on the targeting of cancer cells. Recent advances in nanosystems have explored passive and active targeting strategies for enhancing intratumoral drug concentrations while limiting the unwanted toxicity and side effects to healthy tissue (Maeda *et al.*, 2001, Allen *et al.*, 2002). The targeted delivery of drugs via nanoparticles can lower the required dose of drugs for the treatment of cancer cells and overcome the difficulties associated with conventional drug therapy, such as insolubility under aqueous conditions, rapid clearance, and lack of selectivity, resulting in nonspecific toxicity towards normal cells (Ashley *et al.*, 2011).

1.1.1. Breast Cancer

Breast cancer is the most prevalent cancer for the men and women in the vast majority of countries worldwide (Bray *et al.*, 2011). The risk factors for breast cancer include being overweight, use of menopausal hormone therapy (estrogen and progestin therapy), physical inactivity, consumption of alcoholic beverages everyday, high breast tissue density, radiation therapy to the chest and family history of breast cancer (American Cancer Society, 2009).

Breast tissue mainly consists of glands for milk production, called lobules, ducts carrying milk from lobules to the nipple and stroma which is composed of surrounding fatty tissue and connective tissue (Figure 1.1). Breast cancer can develop in any type of these tissues but generally the origin of tumor is either the cells lining the ducts (ductal carcinoma) or the glands (lobular carcinoma). In some cases tumor formation begins in lobules or rarely in stroma. If cancer cells gain ability of invasion, they spread and metastasize to distant tissues through channels to the lymph nodes or the blood stream to other organs in the body.

Breast cancer pathogenesis and histologic vs. molecular subtypes

Eric Wong and Jenna Rebello

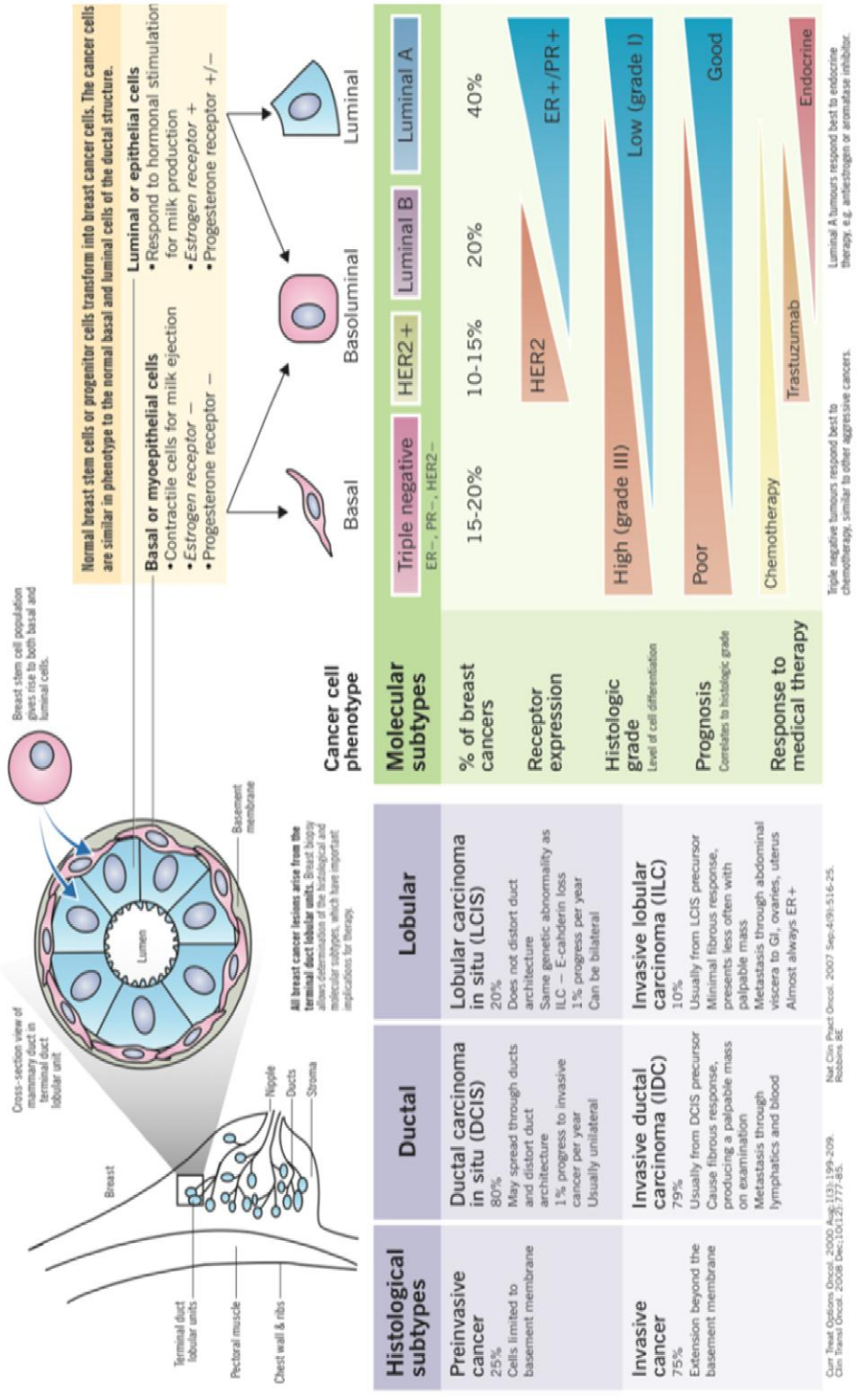


Figure 1.1. Breast cancer types and pathogenesis. (2012-2013 McMaster Pathophysiology Review (MPR) <http://www.pathophys.org/breast-cancer/>).

Clinically, breast tumors can be classified according to hormone receptor status. Estrogen receptor positive (ER⁺) cancers occur three times more often than estrogen receptor negative (ER⁻) cancers (Kocic *et al.* 2010). Patients with ER⁺ tumors are often treated with hormonal therapies to reduce estrogen responses within the tumor and/or with chemotherapy. However, several clinical studies have reported that patients with ER⁺ tumors respond less well to chemotherapy than their counterparts with ER⁻ tumors (Conforti *et al.*, 2007; Kuerer *et al.*, 1999; Berry *et al.*, 2006; Pritchard *et al.*, 2012). Laboratory studies using ER⁺ breast cancer cell lines have also demonstrated that the presence of physiologic estrogen levels counter the effects of chemotherapy, which may explain the clinical observation of mitigated Doxorubicin sensitivity in ER⁺ tumors (Teixeira *et al.*, 1995; Leung & Wang, 1999).

Treatment for breast cancer depends on the stage of the disease, but often includes surgery, chemotherapy and radiation therapy. Some targeted therapies, including anti-hormone therapies and Herceptin® (trastuzumab), have also become part of standard treatment for breast cancer when a patient's tumor expresses the targets of these drugs. Targeted therapies, employing carefully designed drugs, have begun to make personalized therapy and will continue to help researchers tailor cancer treatment based on the characteristics of each individual's cancer. Targeted therapies are important because these new approaches provide better treatment options (National Institute of Health, 2012)

1.1.2. Cervical Cancer

Cervical cancer is a disease in which the cells of the cervix transformed to cancer cells and start to grow uncontrollably, forming tumors. It is a widespread health problem especially in less developed countries. The persistent Human Papillomavirus (HPV 16, 18, 31, and 45) infection is the main cause of cervical cancer by the integration of the HPV genome into the host chromosomes. HPV 16 cause more than 50% of cervical cancers in the world. HPV 18 is the second common type (around 10%), followed by HPV 31 and 45. The dsDNA virus, HPV infects the basal epithelial cells. Then, they can replicate episomally by use of E1 and E2, two HPV encoded proteins (Frazer *et al.*, 2004; Whiteside *et al.*, 2008; Zheng *et al.*, 2006; de Villiers *et al.*, 2004; de Kuo *et al.*, 1994). During the carcinogenic progression, HPV genome is often integrated into the host cell chromosome. In this way, the virus is not only able to complete its life cycle but can persist in the host cell and initiate oncogenesis. This integration frequently disrupts the E1–E2 genome region. E2 protein is transcriptional repressor of E6 and E7 oncogenes (Figure 1.2) Loss of E2 gene expression leads to an increase in expression of both oncogenes (Fernandes *et al.*, 2012; Hebner *et al.*, 2006; Doorbar *et al.*, 2006). E6 inactivates the tumor suppressor p53, that promotes apoptosis in response to DNA damage, and E7 leads to the degradation of Rb (retinoblastoma), suppressor of Akt survival pathways, resulting in activation of the anti-apoptotic proteins mTor, Bcl2 and NF-κB. Both of these viral proteins initiate and maintain the proliferation of cervical cancer cells (Frazer *et al.*, 2004; Whiteside *et al.*, 2008; Zheng *et al.*, 2006; de Villiers *et al.*, 2004; de Kuo *et al.*, 1994).

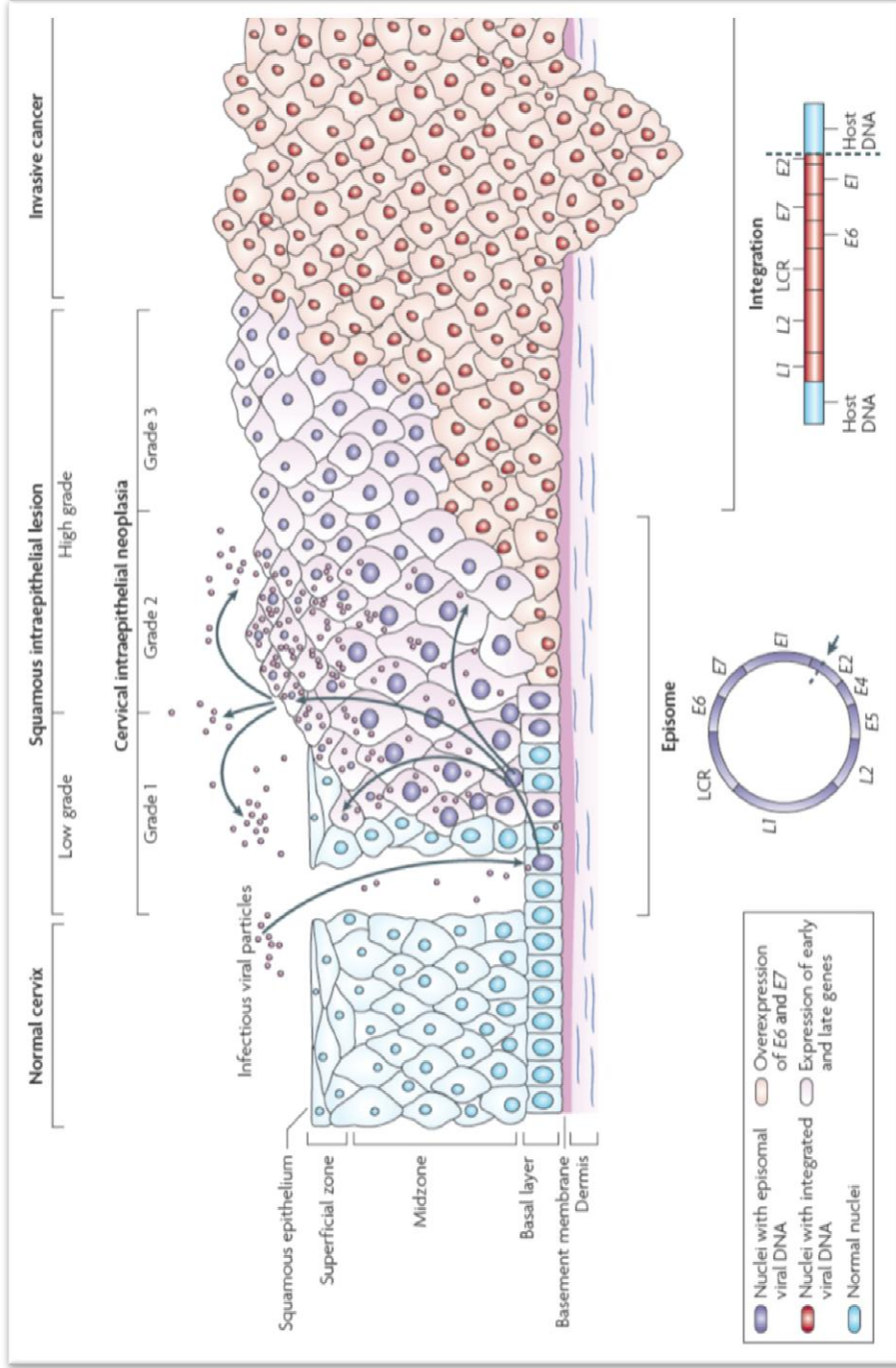


Figure 1.2. HPV-mediated progression to cervical cancer. HPV enters to the basal cells through microabrasions in the cervical epithelium. Following infection, the early HPV genes E1, E2, E4, E5, E6 and E7 are expressed and the viral DNA replicates from episomes (purple nuclei). The late genes L1 and L2 encapsidate the viral genomes to form virions. The progression to invasive cancer is associated with the integration of the HPV genome into the host chromosomes (red nuclei), loss or disruption of E2 gene, and subsequent upregulation of E6 and E7 oncogene expression (Woodman *et al.*, 2007).

E6 and E7 oncogenes bind to different proteins involved in the processes of adhesion, apoptosis, cell cycle, DNA repair, metabolism, signal transduction, transcription and other functions. Neoplastic processes induced by HPV infection have also been linked to viral and host epigenetic changes, including DNA methylation and histone modifications, which contribute to carcinogenesis. 'DNA methylomes' from pre-immortal keratinocytes were found to be almost completely un-methylated, whereas the immortal cells featured densely methylated viral genomes. It is believed that the viral genome is methylated by human host cell DNA methyltransferases (Doerfler *et al.*, 1991; Kalantari *et al.*, 2004; Woodman *et al.*, 2007; Fernandes *et al.*, 2009).

Treatment alternatives of cervical cancer are radiotherapy and chemotherapy (Cisplatin). However, the combinatorial therapy of cisplatin and radiotherapy have better results than radiotherapy alone, 5year survival rate is around 52% (Green *et al.*, 2001), and the treatment still results in morbidity (Maduro *et al.*, 2003).

Further improvements in survival rates by intensification of the standard treatment is limited due to the intrinsic and acquired tumor resistance, and side effects (Hougardy *et al.*, 2005). Better knowledge at the molecular mechanisms of apoptosis and resistance mechanisms might improve the treatment results by the modulation of these pathways.

Despite the high incidence of cervical cancer worldwide, there have not been many studies on innovative drugs. Therefore, alternatives are needed to increase the antitumor efficacy of drugs while decreasing the toxicity on healthy cells. It must be focused on innovative drugs which targets the therapeutics into the tumor site.

1.2. Cancer Chemotherapeutics

1.2.1. Doxorubicin (Adriamycin®)

Doxorubicin (Figure 1.3) is an anthracycline type antibiotic. All anthracyclines bind to double stranded DNA and intercalate it, thereby are called as intercalating agents.

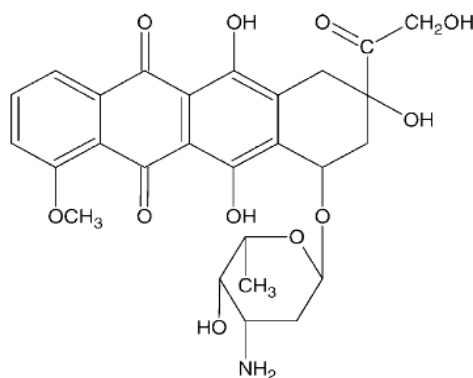


Figure 1.3. Molecular formula of Doxorubicin (Pajeva *et al.*, 2004).

Anthracyclines have a number of important effects in the cytotoxic actions of these drugs. Firstly all anthracyclines can intercalate and interfere with DNA and RNA synthesis. Secondly, they interfere with a single step of the catalytic cycle of Topoisomerase II (Topo II) by stabilizing it in cleavable complex (Robert and Larsen *et al.*, 1998). DNA strand breakages may be formed due to inhibition of break rejoining activity of Topo II. Thirdly, anthracyclines can also cause the formation of reactive oxygen species (ROS) and free radical damage on cells contributing to antitumor activity of the drug (Figure 1.4). The anthracycline chromophore contains a hydroxyquinone which is a well-described iron chelating structure. The drug-Fe complex catalyzes the transfer of electrons from glutathione to oxygen, resulting in the formation of ROS and free radicals in the cell. Superoxide and hydroxyl radicals are produced by the reductive semiquinone species. Peroxidation of unsaturated membrane lipids causes disturbance of membrane structure and dysfunction of mitochondria which is, in particular, related to extensive cardiotoxicity of Doxorubicin (Muraoka *et al.*, 2004).

The drug-Fe complex can also cause single strand breakages in DNA. Collectively, the effects are inhibition of cell proliferation, induction of G₂-M cell arrest (Kwok *et al.*, 1994) or apoptosis (Walker *et al.*, 1991). Although the effect of Doxorubicin on cells is not phase specific, cells in the S and G₂ phases are more sensitive than cells in G₁.

In addition, it has been reported that Doxorubicin can directly inhibit nitric oxide synthase activity, which may result in significant alterations in vascular tone both in the heart and in tumors. Figure 1.4 summarizes the action mechanisms of Doxorubicin on the cells (Chabner and Longo,2005).

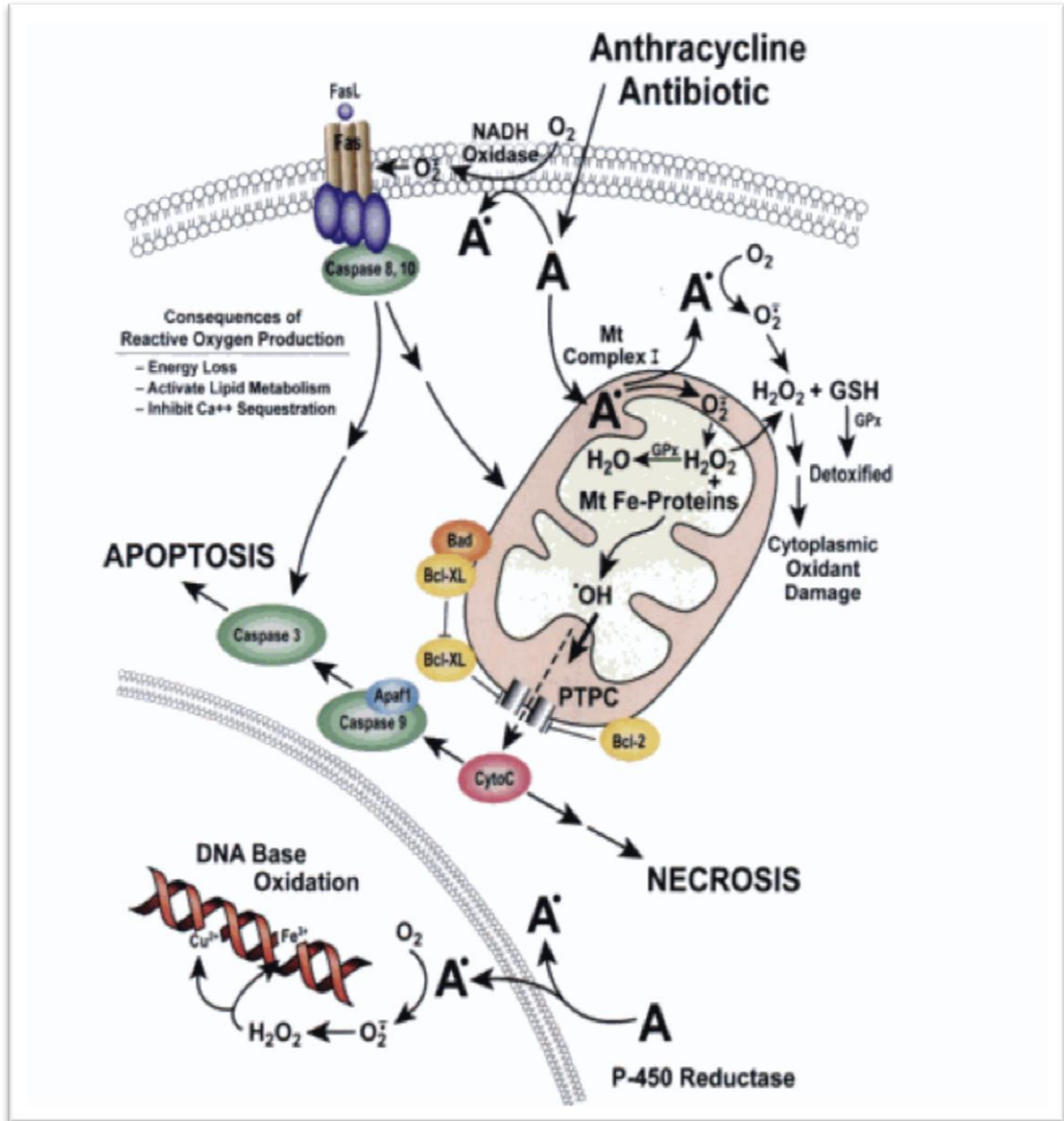


Figure 1.4.Cell death mechanisms of anthracyclines (Chabner and Longo, 2005).

The mechanisms of action cause the nucleus to be one of the targets of Doxorubicin. Recently, its entry to the nucleus has been described. Once Doxorubicin diffuses through the plasma membrane, a substantial portion of the drug is bound to the 20S fraction of the proteasome. Afterwards, the drug is actively transported to the nucleus in an ATP requiring, nuclear pore dependent process by means of nuclear localization signals found in 20S proteosomal subunits. Due to its higher affinity to DNA, Doxorubicin dissociates from the proteasome in the nucleus (Chabner and Longo, 2005).

It is effective in a wide range of cancers, including both hematological and solid tumors. The highest activity was observed against solid tumors, particularly ER⁺ breast cancer. Others are ovary, bladder, and lung carcinomas. It is also active in the treatment of Non-Hodgkin's lymphoma and Hodgkin's disease.

The principle hindrance to the clinical efficiency of chemotherapy has been toxicity to the normal tissues and the development of cellular drug resistance. Doxorubicin resistance is generally associated with MDR1/MRP overexpression, altered levels of topoisomerase II expression, expression of mutated forms of topoisomerase II, increased glutathione or glutathione peroxidase levels, DNA mismatch repair deficits, cellular resistance to apoptosis and finally changes in the membrane lipid composition (Paul and Cowan, 1999; Pajeva *et al.*, 2004). Breast cancer tumor resistance is mainly associated with overexpression of P-gp (Gottesman *et al.*, 2002). Therefore, in order to achieve better clinical outcome and increase the success of chemotherapy in breast cancer tumors, Doxorubicin was loaded into the nanoparticles to improve the drug influx by escaping P-gp pumps and overcome P-gp transporter mediated multidrug resistance (MDR).

Acute adverse effects of Doxorubicin are nausea, vomiting, neutropenia, alopecia, and arrhythmias. The incidence of acute cardiotoxicity is approximately 11% (Chatterjee *et al.*, 2010). The chronic side effect of Doxorubicin is its dose dependent cardiotoxicity. As the lifetime accumulative dose approaches 500 mg/m² and beyond, iatrogenic lifethreatening cardiomyopathy becomes more likely, which can lead to dilated cardiomyopathy and congestive heart failure in up to 20% of cases (Chatterjee *et al.*, 2010). This chronic cardiotoxicity is likely related to iron oxidation and oxygen free radical formation, rather than the drug's anti tumor mechanisms, since cardiomyocytes are minimally replicating cells (Shi *et al.*, 2011).

1.2.2. Bortezomib (Velcade®)

Bortezomib is the first approved proteasome inhibitor drug by the US Food and Drug Administration (FDA) for the clinical treatment of newly diagnosed, relapsed/refractory multiple myeloma and mantle cell lymphoma, and acts by reversibly inhibiting the proteasomal activity in addition to multiple oncogenic pathways in tumor cells. Bortezomib is a dipeptide boronic acid derivative which contains pyrazinoic acid, phenylalanine and leucine with boronic acid in its structure (Figure 1.5) (Chenet *et al.*,2011; Kane *et al.*,2003; Kane *et al.*,2007).

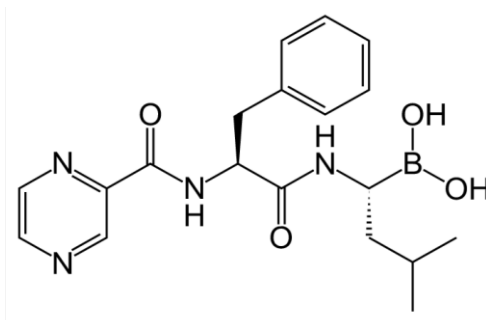


Figure 1.5.Molecular formula of Bortezomib (Chen *et al.*, 2011).

Bortezomib is registered for the treatment of relapsed and refractory multiple myeloma. A phase I study is being done to investigate the use of Bortezomib and radiotherapy in patients with recurrent or metastatic squamous-cell carcinoma of the head and neck, a clinical setting comparable to cervical cancer. The knowledge acquired from patients with head and neck cancer should be exploited, because this cancer resembles to cervical cancer in HPV positivity, squamous cell carcinoma, association with smoking, and sensitivity to combination therapy (Adams *et al.*,2004; Sunwoo *et al.*,2001; Lenz *et al.*,2003; Crawford *et al.*,2006).

The proteasome is a multicatalytic enzyme complex found abundantly in both the nucleus and the cytoplasm of cells. The proteasome has an important role in the regulation of intracellular protein degradation by functioning as a protein shredder. It calibrates the concentrations of proteins involved in cell cycle progression,apoptosis and inflammatory responses (Adams *et al.*,2004). The major HPV encoded oncoproteins, E6 and E7, target the host tumorsuppressorgene products p53 andpRB, respectively, for accelerated proteasomal degradation and inactivation of tumor suppressors, thereby contribute to cellular transformation and immortalisation (Figure 1.6 and 1.7).

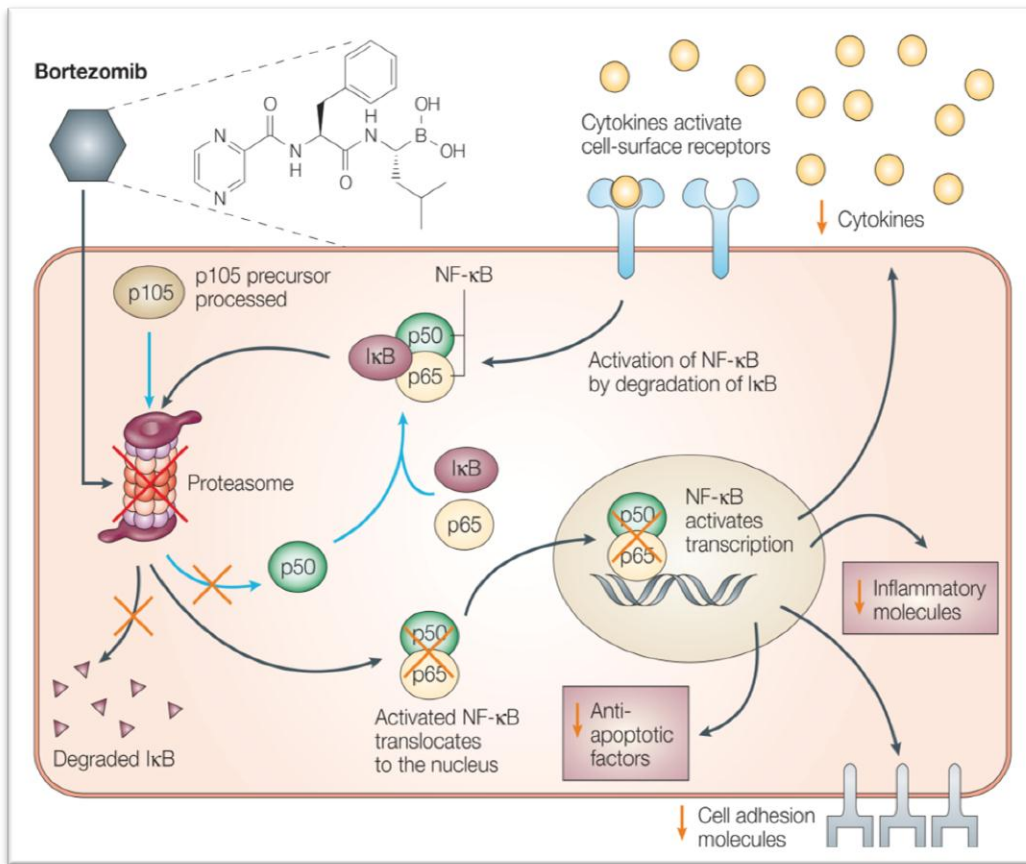


Figure 1.6. The proteasome inhibitor, Bortezomib, kills cancer cells by blocking the NFκB activity. In normal cells, NFκB is found as bound to its inhibitory protein (IκB), which maintains NFκB at inactive form in the cytosol. Proteasome is essential for the activation of NFκB, it catalyses the proteolytic generation of the NFκB subunit p50 from the inactive p105 precursor and the destruction of the inhibitory IκB. NFκB is constitutively active in certain tumors. The activated NFκB enters the nucleus, and helps the cell to survive and proliferate. By inhibiting the activation of NFκB (orange crosses), Bortezomib reduces antiapoptotic factors; inflammatory molecules; cell adhesion molecules, which allow attachment cells to adhere to bone marrow cells; and cytokines, which promote the growth of myeloma cells (Paramore and Frantz, 2003).

Many types of proliferating malignant cells are more susceptible to proteasome blockade than are healthy cells (Voorhees *et al.*, 2003). Bortezomib also has an effect in tumors that do not express p53, showing that it can induce p53-independent apoptosis (Yerlikaya *et al.*, 2013). Therapeutic strategies that rescue the tumor suppressor pathways by blocking degradation of proteasomes might be useful to treat cervical cancer (Shackelford *et al.*, 2004).

Apoptosis of cancer cells can take place through intrinsic (mitochondria dependent) or extrinsic (mitochondria independent) pathways. The intrinsic apoptotic pathway is initiated by DNA damage, stress molecules, or growthfactor withdrawal. Important regulators of the intrinsic pathway are the BCL2 protein family members, which are either death antagonists (BCL2, BCLXL) or death agonists (BAX, BAK, BAD, BID, BIK, BIM, PUMA, NOXA). The p53 protein is a mediator of the mitochondrial apoptotic pathway in response to stress signals such as radiation and chemotherapy. Activation of the intrinsic,mitochondrial pathway results in release of cytochrome C and activation of caspase 9, which then activates caspase 3 (Figure 1.7).

The extrinsic apoptotic pathway is initiated by the activation of death receptors (DRs) on cell membrane. Apoptosis is triggered by the binding of specific TNF superfamily ligands, such as FASL or TRAIL, to their cognate receptors FAS, and DR4 or DR5, respectively (Figure 1.7). DR activation results in the formation of an intracellular death-inducing signaling complex, recruited procaspase 8 molecules, which initiates intracellular apoptotic cascades. Activation of caspase 8 leads to activation of caspase 3, either directly or indirectly by cleaving BID. Cleaved or truncated BID translocates to the mitochondria to trigger the mitochondrial apoptotic pathway.

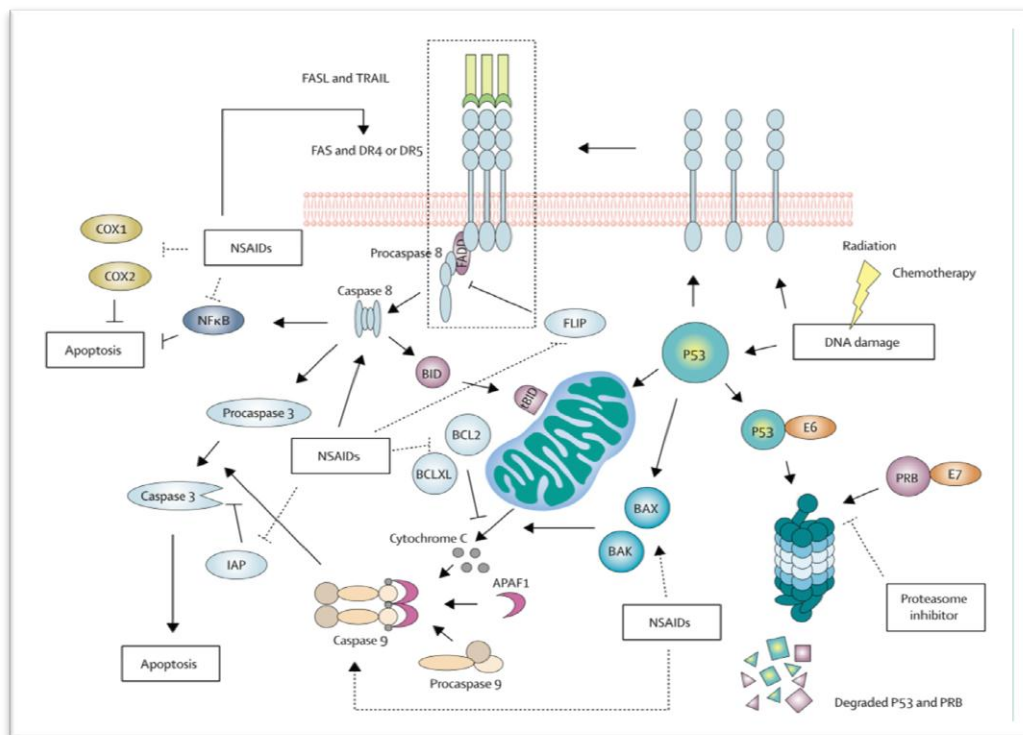


Figure 1.7. Apoptosis induction by death receptors results in the activation of extrinsic and intrinsic apoptotic pathways. The apoptosis cascade following DNA damage. The effect of proteasome inhibitors (Bortezomib) on E6 and E7-mediated degradation of p53 and pRB is shown (Hougardy *et al.*,2005).

Bortezomib is a selective inhibitor of both standard proteasomes and immunoproteasomes, which influences antiviral responses and the viral peptides. Bortezomib is an important drug for the treatment of cervical cancer. Bortezomib inhibits activation of NF κ B and sensitizes cells to chemotherapy, radiation, or immunotherapy without added toxicities (Cveket *et al.*, 2004).

Bortezomib reversibly inhibits the chymotrypsin-like activity at proteasome β 5 subunit and to a lesser extent inhibits the trypsin-like activity at the β 1 subunit. The mutations at key points of β 5 subunit and overexpression of β subunits leads to Bortezomib resistance by decreasing the affinity to Bortezomib and contributing to the high basal levels of proteasome activity, respectively. Most importantly, efflux transporter P-gp was shown to mediate a certain degree of Bortezomib resistance (Rumpold *et al.*, 2007; Lü and Wang, 2013). It is possible to bypass the P-gp pumps by loading Bortezomib into the nanoparticles, to increase the efficacy of drug and overcome P-gp transporter mediated resistance.

General side effects of Bortezomib are asthenic conditions (fatigue, malaise, and weakness), pyrexia, headache, insomnia, dizziness, back pain, dehydration, anxiety and rigors (Drugs.com, 2013).

1.3. Targeted Drug Delivery Systems

Conventional chemotherapeutic agents are unspecifically distributed all over the body where they affect both cancerous and normal cells. This treatment results in excessive toxicities. Targeted drug delivery with nanoparticles has emerged to overcome the lack of specificity of conventional chemotherapeutic agents (Hausen *et al.*, 2009). Nanoparticles are promising to circumvent these challenges, by enabling high amounts of drugs to be loaded and targeted to the tumor site. Delivery of drugs via nanoparticles increases the half life and reduces toxic side effects of drugs, by improving their pharmacokinetic profile and therapeutic efficacy (Shubayev *et al.*, 2009; Kim *et al.*, 2005; Pan *et al.*, 2007).

Nanotechnology opened a new door to the development of particles with nano sizes that can be fabricated from a multitude of materials in a variety of compositions, including quantum dots (Ferrari *et al.*, 2005) polymeric nanoparticles (Li *et al.*, 2004, Unsoy *et al.*, 2012) gold nanoparticles (Lagaru *et al.*, 2007) magnetic nanoparticles (Kjaer *et al.*, 2006) and dendrimeric nanoparticles (Pan *et al.*, 2007; Gao *et al.*, 2005; Khodadust *et al.*, 2013).

After the synthesis of nanoparticles, surface modifications with organic molecules enables stabilization of nanoparticles in a biological suspension with a pH around 7.4 and a high salt concentration, provides functional groups at the surface for further derivatization, and prevents immediate uptake of drug loaded nanoparticles by the reticuloendothelial system (RES) (Fusselet *et al.*, 1997). Ligands such as targeting agents, permeation enhancers, optical dyes, and magnets can all be conjugated on the surface or incorporated within these nanostructures (Figure 1.8) (Aslam *et al.*, 1998; Hermanson *et al.*, 1996; Sun *et al.*, 2008).

The idea of targeted drug delivery was introduced almost a century ago by Paul Ehrlich with the concept of the “magic bullet”. This “bullet” consists of two components: the first is recognition of and successful binding to the target; the second is effectively delivering the therapeutic agent for suppression of the targeted tumor (Strebhardt *et al.*,2008) (Figure 1.8).

Targeted drug delivery systems by nanoparticles may have some difficulties, such as low drug loading capacity, heterogenous size distribution and insufficient targeting; these difficulties can be accomplished by the appropriate nanoparticle design (Maeda *et al.*,2010).

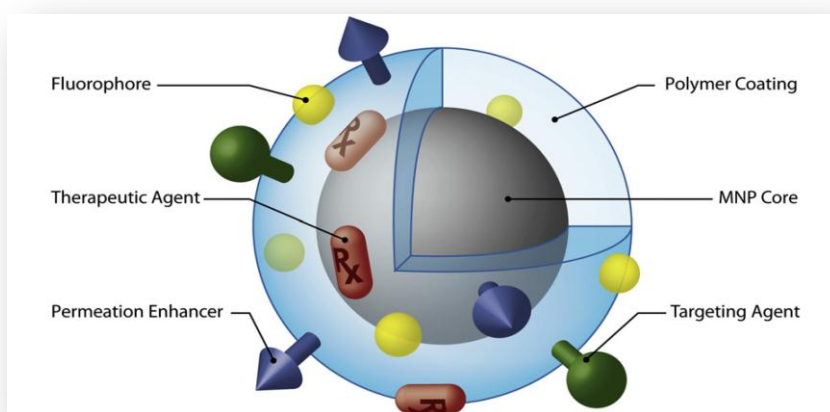


Figure 1.8. Schematic representation of functionalized, polymer coated superparamagnetic (iron oxide) nanoparticles (Sun *et al.*,2008).

Nanoparticles can be routed to the tumor tissue via passive or active targeting but active targeting highly increases the efficacy. Passive targeting occurs by the extravasation of drug loaded nanoparticles which are able to penetrate tumors due to their small size, and the hyperpermeable, leaky nature of tumor microvasculature. Furthermore, poor lymphatic drainage of tumor microenvironment results in slow clearance of nanoparticles and their selective accumulation in tumor tissue (Figure 1.9). This is referred as the enhanced permeation and retention (EPR) effect (Matsumura *et al.*, 1986; Maeda *et al.*,2000). The majority of solid tumors exhibit a vascular pore cut-off size between 380 nm and 780 nm, although vasculature organization may differ depending on the tumor type, its growth rate, and microenvironment. There is no limitation as the diameters of nanoparticles are below of the narrowest capillaries. The main limitation is the residence time of nanoparticles in the bloodstream. Size dependent removal of nanoparticles is a common occurrence in healthy capillaries. Thus, the use of conventional nanoparticles for targeted drug delivery by passive targeting is restricted to mononuclear phagocyte system organs such as spleen, liver, and bone marrow. Targeting tumors at other tissues would be achieved by active targeting because of the short circulation times and the low concentrations of nanoparticles at the tumor site, resulting with the low drug concentrations below the therapeutic level (Maeda *et al.*, 2010).

Active magnetic targeting is based on the physical characteristics of nanocarriers. Therefore, nanocarriers sensitive to physical stimuli (e.g. magnetism, temperature, pH) have been developed and conjugated with drugs for magnetic targeting. The drug, as conjugated to a magnetic nanocarrier, is introduced to the body, and concentrated at the tumor site by an externally applied magnetic field or an internally implanted permanent magnet; then, the drug was released from the nanoparticles (Figures 1.9, 1.10 and 1.11) (Moghimi *et al.*, 2005).

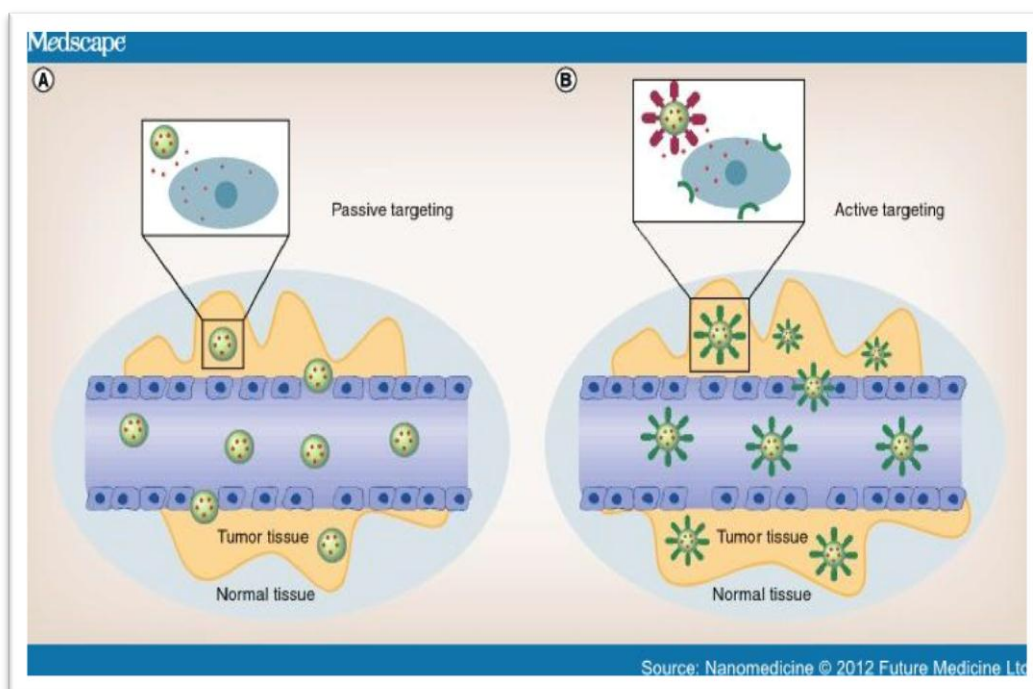


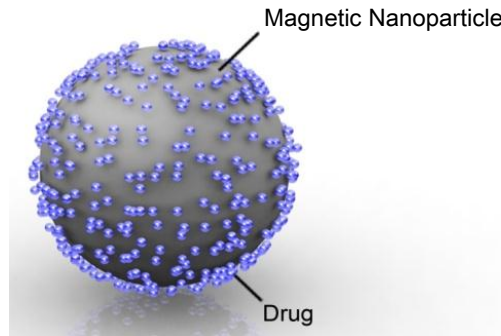
Figure 1.9. Passive and active targeting. Nanoparticles can be passively extravasated through leaky vascularization by EPR effect, allowing their accumulation at the tumor region (a). Drugs may be released in the extracellular matrix and then diffuse through the tissue. However, active targeting (b) can enhance the therapeutic efficacy of drugs by the increased accumulation and cellular uptake of nanoparticles through magnetic field or receptor-mediated endocytosis. Nanoparticles can be engineered as superparamagnetic or incorporated with ligands that bind to cell surface receptors (Zhao *et al.*, 2012).

Controlling the aggregation of nanoparticles in the tumor environment, by considering the differences of tumor microenvironment from the normal tissue, such as low pH, low O₂, or matrix metalloproteinase enzymatic activity, can serve as a novel strategy to enhance retention and cell uptake of nanoparticles in tumors and improve the performance of nanoparticles used in cancer diagnosis and treatment (Liu *et al.*, 2013).

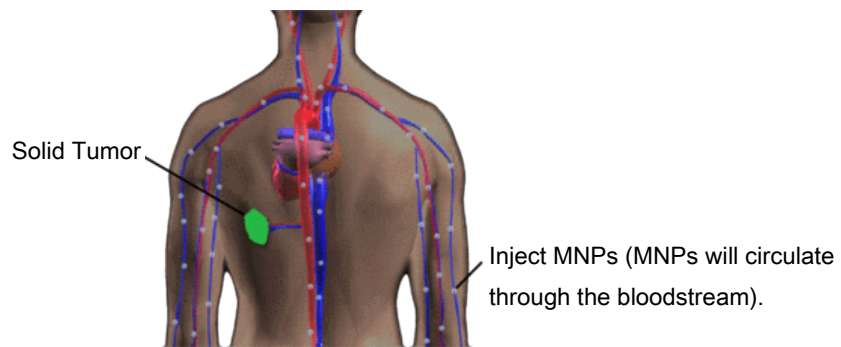
1.3.1. Magnetic Nanoparticles in Targeted Drug Delivery

Nanoparticles can enhance the intracellular drug concentrations in cancer cells by using active magnetic targeting strategies, while avoiding toxicity in normal cells (Maduro *et al.*, 2003; Hougardy *et al.*, 2005) (Figures 10 and 11).

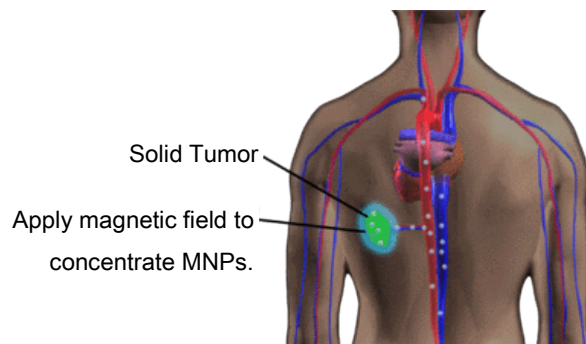
- a. Drug is loaded onto the magnetic nanoparticles, which act as a nanocarrier.



- b. The anticancer drug loaded magnetic nanoparticles are injected into the bloodstream and these nanoparticles circulate all over the body.



- c. A magnetic field is applied at the target site (tumor location) in order to concentrate drug loaded magnetic nanoparticles at the tumor location.



d. The anticancer drug is released at targeted site, allowing the drug to enter the tumor area. In addition, magnetic nanoparticles can be imaged under MRI to ensure that they reached their targeted destination.

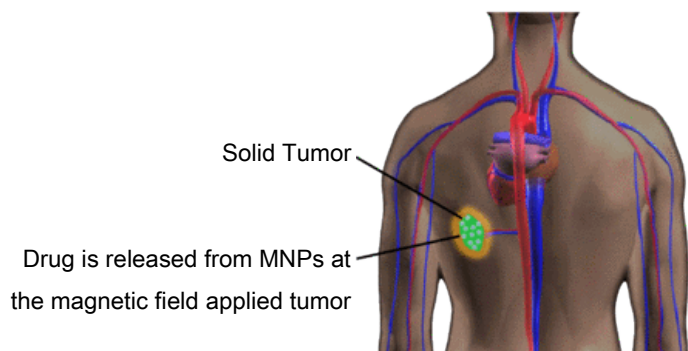


Figure 1.10. Anticancer drug loaded nanoparticles are magnetically guided by external magnetic field after the intravenous administration of magnetic nanoparticles (Biophan Technologies, 2013).

Magnetic nanoparticles are guided to the tumor tissue under the magnetic field. Permanent Nd-Fe-B magnets in combination with superparamagnetic iron oxide nanoparticles, which have excellent magnetic properties, can reach effective magnetic field depths up to 10-15 cm in the body (Neuberger *et al.*, 2005). Obviously, the geometry of the magnetic field is extremely important and must be taken into the consideration when designing a magnetic targeting system. Since the magnetic gradient decreases with the distance to the target, the main limitation of magnetic drug delivery relates to the strength of the external field that can be applied to obtain the necessary magnetic gradient to control the residence time of NPs in the desired area or which triggers the drug desorption.

Schenck (2005) reported that, “FDA initially considers the applications for approval to market MRI scanners on a case by case evaluation of the safety and efficacy information. Based on positive clinical and safety experience, the FDA classified magnets with field strength of less than 2 T as nonsignificant risk devices in 1987. Further positive experiences led the FDA to increase this threshold to 4 T in 1996 and again in 2003 to 8 T (for adults). Even though experiments with strong static magnetic fields (8 T) have been shown to reduce the flow rate of human blood by 30% in *in vitro* tests (Haik *et al.*, 2001) and it has been reported that magnetic fields above 3 T might affect the normal behavior of erythrocytes, recent studies evaluating human subjects for adverse effects in physiological or neurocognitive functions resulting from exposure to static magnetic fields (up to 8 T) from MRI systems have not shown any clinically relevant effects (Chakeres *et al.*, 2005).”

According to Kangarlu and Robitaille (2000), “human imaging at magnetic fields in excess of 10 T will most probably be achieved within the decade and such projects are now being planned”(Figure 1.11)(Kangarlu and Robitaille, 2000; Arrueboa *et al.*,2007).

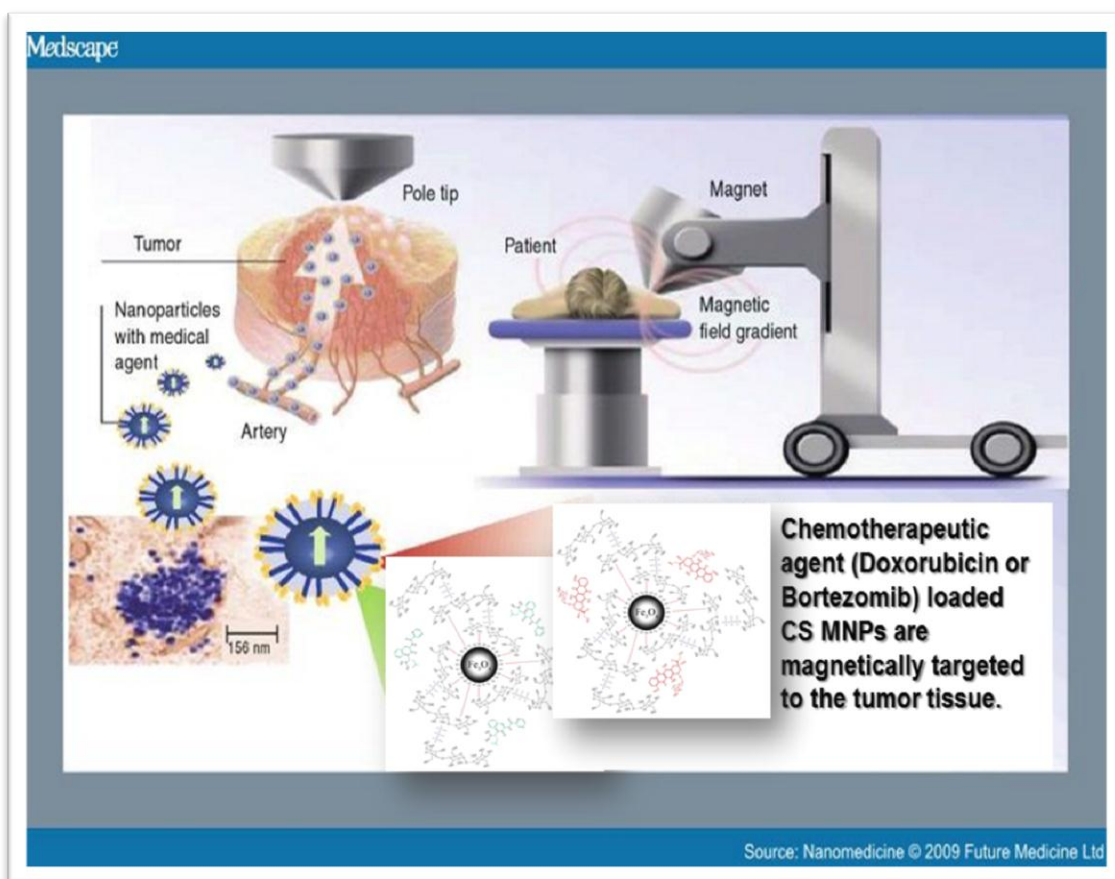


Figure 1.11. Active magnetic drug targeting; magnetic drug carriers disintegrate in the target zone and release the drug(Bakarat *et al.*,2009).

The main advantages are, magnetic nanoparticles can be targeted by a magnetic field; visualized (superparamagnetic nanoparticles are used as MRI agents); and trigger drug release when heated via magnetic field or produce hyperthermia of tissue (Goya *et al.*,2008).

Superparamagnetism(negligible remanence and coercivity) is necessary for targeted drug delivery because once the external magnetic field is removed,magnetization of nanoparticle disappears, and thus agglomeration and the possible embolization of capillary vessels are avoided(Figure 1.12).

15.09.2013 1

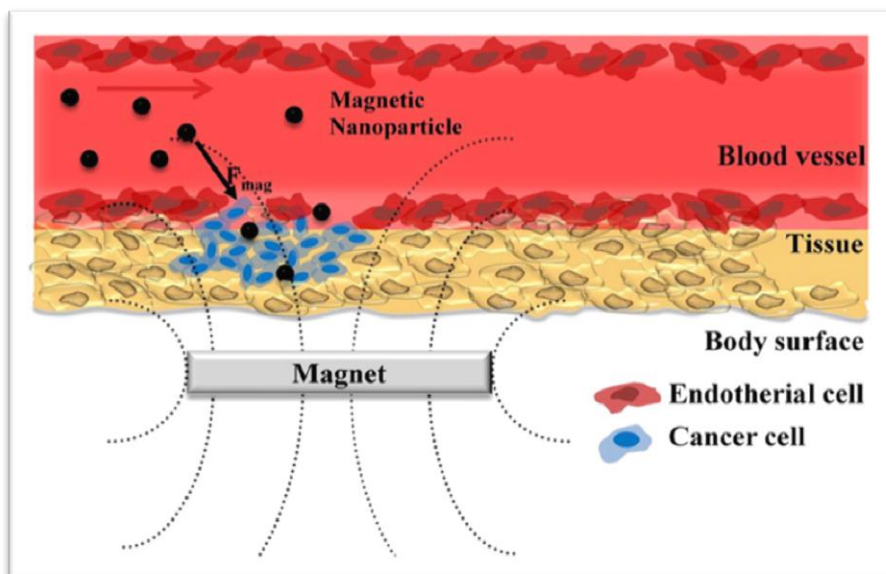


Figure 1.12. Schematic representation of tissue specific delivery of superparamagnetic nanoparticles (Park *et al.*, 2010).

The behavior of superparamagnetic nanoparticles are related to the size (size distribution, magnetic core, and hydrodynamic diameter), magnetic properties (magnetic saturation, coercivity, remanence), and surface chemistry of nanoparticles. The surface chemistry is especially important to increase the half life of nanoparticles in the bloodstream and escape from the reticuloendothelial system (RES), which is a part of the immune system. Coating of nanoparticles with hydrophilic compounds increases the circulatory halflife from minutes to hours or days. Reducing the particle size is an alternative way however, the complete avoidance of the RES does not seem possible (Gaur *et al.*, 2000).

The biodistribution of drug loaded nanoparticles in the body depends on various physicochemical factors; such as size of nanoparticles, surface charge, surface hydrophobicity, capacity for protein adsorption, drug loading and release kinetics, toxicity, stability, degeneration of carrier systems, hydration behavior, electrophoretic mobility, porosity, crystallinity, contact angle, and molecular weight. Nevertheless, the fate of magnetic nanoparticles also strongly depends on the administration route (oral, intravenous, pulmonary, transdermal, and ocular) and the dose.

Drug release from the superparamagnetic iron oxide nanoparticles can take place by simple diffusion or proceed through changes in physiological conditions such as pH and ionic strength, or mechanisms requiring enzymatic activity. Superparamagnetic iron oxide nanoparticles are considered as biodegradable owing to their iron (Fe) is reused and recycled by cells with normal biochemical pathways for Fe metabolism (Arrueboa *et al.*, 2007).

1.3.2. Chitosan as Surface Coating Material

Irrespective of particle type and surface ligands, the majority of systemically administered drug loaded nanoparticles to reach the targeted tumors depend on the leakiness of the vasculature around the tumor area (Kirpotin *et al.*, 2006; Mamot *et al.*, 2005; Bartlett *et al.*, 2007). Therefore, prolonged circulation and reduced immune clearance are primary design criteria for tumor targeted nanoparticles. Since hydrophobic surfaces of nanoparticles cause nonspecific interactions with healthy tissues (Moreno *et al.*, 2010) and premature clearance by the RES, (Carrstensen *et al.*, 1992) nanoparticles are coated with polymer, forming a hydrated shell.

The coating also facilitates the stabilization of nanoparticles in an environment with a slightly alkaline pH or a significant salt concentration. The coating retards the clearance of nanoparticles by the RES. Depending on their surface functionalization, size, and hydrophilicity, a rapid uptake of uncoated nanoparticles by the mononuclear phagocyte system is likely after systemic administration, followed by clearance to the spleen, liver, and bone marrow. Different proteins of the blood serum bind to the surface of foreign bodies, accelerating phagocytosis of the particles. Various coating materials (biodegradable and non-biodegradable; organic and inorganic) can be used to retard detection and uptake of nanoparticles by the macrophages of the RES. One of the most widely used coating material is chitosan, whose attachment to nanoparticle surfaces provides a shielding effect, delaying the action of the RES (Neuberger *et al.*, 2005; Macaroff *et al.*, 2006).

The nature of the coating material is important to reduce the aggregation and increase the stability of nanoparticles in body fluids. Superparamagnetic iron oxide nanoparticles can be functionalized or modified with coatings of hydrophilic, biocompatible, and biodegradable polymers, such as chitosan.

Chitosan is a natural, alkaline, hydrophilic, biodegradable, and biocompatible polymer with no toxicity (Figure 1.13). Chitosan has been widely used in gene delivery. Chitosan-DNA nanoparticles were capable of conferring immunological protection to mice against a peanut antigen, indicating a possible use of chitosan in delivering genetic vaccines to control food allergens. However, chitosan at high doses can cause hypocholesterolemia in humans, thereby limiting its applications (Lee *et al.*, 2005).

One of the most relevant properties of chitosan, with particular interest in drug delivery, relies on its ability to transiently open epithelial tight junctions, resulting in the permeation enhancement of macromolecules through well organized epithelia such as nasal (Fernandez *et al.*, 1999; Vila *et al.*, 2004), intestinal (Artursson *et al.*, 1994; Borchard *et al.*, 1996; Prego *et al.*, 2005), ocular (De Campos *et al.*, 2001), buccal (Portero *et al.*, 2002) and pulmonary (Al-Qadi *et al.*, 2012).

The word ‘chitosan’ refers to a large number of polymers, which differ in their degree of *N*-deacetylation (40-98%) and molecular weight (50 000 - 2 000 0000 Daltons). These two characteristics are very important to its physicochemical properties and may have a major effect on the biological properties (Sannan *et al.*,1976). Chitosan salts are soluble in water; the solubility depends on the degree of deacetylation and the pH of the solution. With a p*K*_a of approximately 6.5, chitosan is soluble at acidic solutions owing to the protonation of the amino groups in the polymeric chain (Rinaudo *et al.*, 2008; Singh *et al.*,2000). In this regard, highly deacetylated chitosan (85%) is readily soluble in solutions of pH up to 6.5, but as the deacetylation degree decreases, the solubilization becomes more difficult (Cho *et al.*,2000).

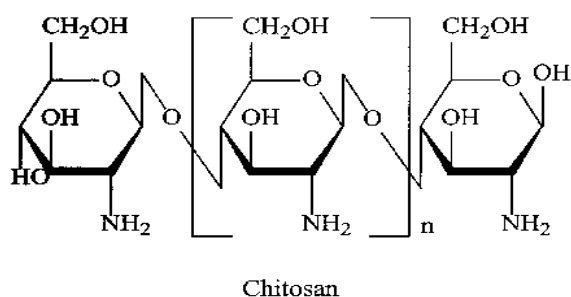


Figure 1.13. Molecular formula of chitosan (Ravi Kumar, 2000).

The usage of chitosan as a coating material is preferable to modify the surface properties of the core structure, either to improve the pattern of interaction with surrounding structures or to improve the biodegradation profile (Andrade *et al.*, 2011; Fonte *et al.*,2012; Grenha *et al.*,2012; El-Sherbiny *et al.*,2011). Chitosan has an intrinsic antitumor activity, stimulating the production of Tissue Necrotic Factor- α (TNF- α) by monocytes, promoting production of nitrogen oxide by macrophages and enhances mRNA production and stimulates neutrophils. Chitosan molecules demonstrated a good retention in the blood circulation and a slight accumulation in tissues, suggesting that chitosan is an effective carrier for drugs that are excreted rapidly (Dodane *et al.*,1998).

Chitosan nanoparticles were demonstrated as pH responsive systems with a reversible process of swelling and shrinking of particles. In tumor cells, low pH values, such as pH 5.5 are generated by the anaerobic glucose metabolism. Moreover, pH values of 3.0–5.5 are seen in acidic intracellular organelles, such as endosomes and lysosomes, within the cancer cells (Lim *et al.*, 2011). Thus, pH responsive chitosan nanoparticles would be expected to have an effective drug release in the tumor microenvironment since the drug release rate can be suddenly accelerated with lower pH after endocytosis into cancer cells (Aydm *et al.*, 2012).

1.3.3. Chitosan for Surface Coating of Magnetic Nanoparticles

Magnetic nanoparticles, which can be targeted to tumor site in a magnetic field, gained importance in cancer therapy in recent years. Magnetic nanoparticles include metallic, bimetallic, and superparamagnetic iron oxide nanoparticles, which have reactive surface that can be coated with biocompatible polymers and loaded with therapeutic agents (Sun *et al.*, 2008; Gupta&Gupta, 2005). There are several commercially available MNP-based agents, which were approved for biomedical application such as MRI agents (Gupta *et al.*, 2007).

Chitosan is adequate for targeted delivery with its structural and biological properties, which include the cationic character and the solubility in aqueous medium. The biodegradability and mucoadhesivity of chitosan are the other advantages (Amidi *et al.*, 2010; Lehr *et al.*, 1992; Baldrick *et al.*, 2010; Dash *et al.*, 2011). These properties are a result of the proper structure of the polysaccharide, which is composed of repeating alternated units of *N*-acetylglucosamine and D-glucosamine, linked by β -(1-4) glycosidic bonds (Rinaudo *et al.*, 2008; Rodrigues *et al.*, 2012).

Chitosan coating around the iron oxide core provided through ion pair formation with the TPP ions, protonated chitosan ionically interacts with TPP molecules and forms chitosan–TPP network. This mainly occurs due to simultaneous cross linking of chitosan with TPP ions and neutralization through deprotonation. The ionic interaction between the chitosan molecules and TPP ions is depicted in Figure 1.14.

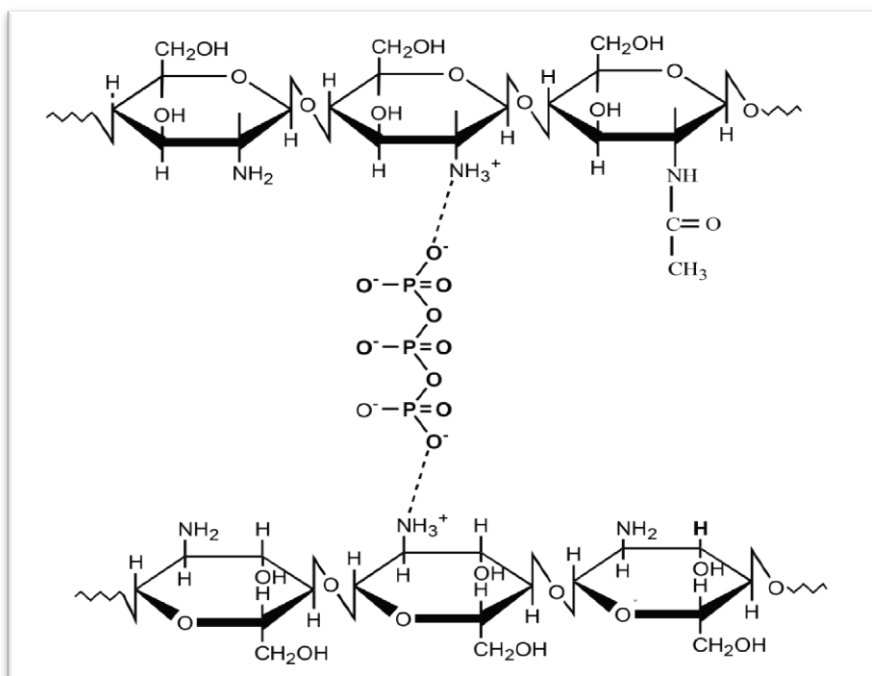


Figure 1.14. Schema showing the interaction between the chitosan and the crosslinker, TPP molecules.

1.3.4. Cellular Uptake of Nanoparticles

Nanoparticles can efficiently intrude into the living cells by endocytosis, resulting in permanent cell damage (Lunov *et al.*, 2010; Asha Rani *et al.*, 2008). Only specialized cells such as macrophages are capable of phagocytosis, a form of endocytosis in which the cell engulfs large particles. Almost all cells internalize nanoparticles by pinocytosis. Four different basic pinocytic mechanisms are known, macropinocytosis, clathrin-mediated endocytosis, caveolae-mediated endocytosis and mechanisms independent of clathrin and caveolin (Conner *et al.*, 2003; Jianget *et al.*, 2011). Physicochemical properties of nanoparticles including size (Chithrani *et al.*, 2006; Rejman *et al.*, 2004), shape (Chithrani *et al.*, 2006), surface charge (Labhasetwar *et al.*, 1998; Arbab *et al.*, 2003; Sun *et al.*, 2005) and surface chemistry (Nativo *et al.*, 2008) have been identified as modulating the cellular uptake efficiency (Treuel *et al.*, 2013).

Nanoparticles may also enter cells by passive penetration of the plasma membrane (Wang *et al.*, 2012). It was shown that the adherence and penetration abilities of nanoparticles depend on the physical properties, including size, surface composition and surface charge (Verma *et al.*, 2008; Leroueil *et al.*, 2007; Roiter *et al.*, 2008). Small and positively charged nanoparticles were observed as passing through the cell membranes, leading to membrane rupture and noticeable cytotoxic effects (Leroueil *et al.*, 2008; Yu *et al.*, 2007; Kostarelos *et al.*, 2007; Choet *et al.*, 2009). Even particles greater than 500 nm in diameter were reported to penetrate cell membranes by inducing strong local membrane deformations (Zhao *et al.*, 2011). Membrane disruption can be reduced or even entirely avoided by a suitable design of the surface structure and charge density (Verma *et al.*, 2008; Lin *et al.*, 2010). Cell adhesion and potential cell uptake of chitosan coated magnetic nanoparticles should be efficient due to its positive charge which is attracted by negatively charged cell membranes.

The drugs, whose target molecules are within the cells, have to penetrate the cellular membrane and escape from the endosome before exhibiting their biological effects. The pH responsive, N-acetyl histidine conjugated glycol chitosan nanoparticles were developed for the efficient intracytoplasmic delivery of paclitaxel (Park *et al.*, 2006). Under slightly acidic conditions (similar to endosomes), the amino groups of chitosan get protonated. This may induce the influx of water and ions into endosomes when the nanoparticles are taken up by the cells, causing disruption of endosomal membranes (Figure 1.15). As a consequence, the disassembled nanoparticles could release the encapsulated drug into the cytosol.

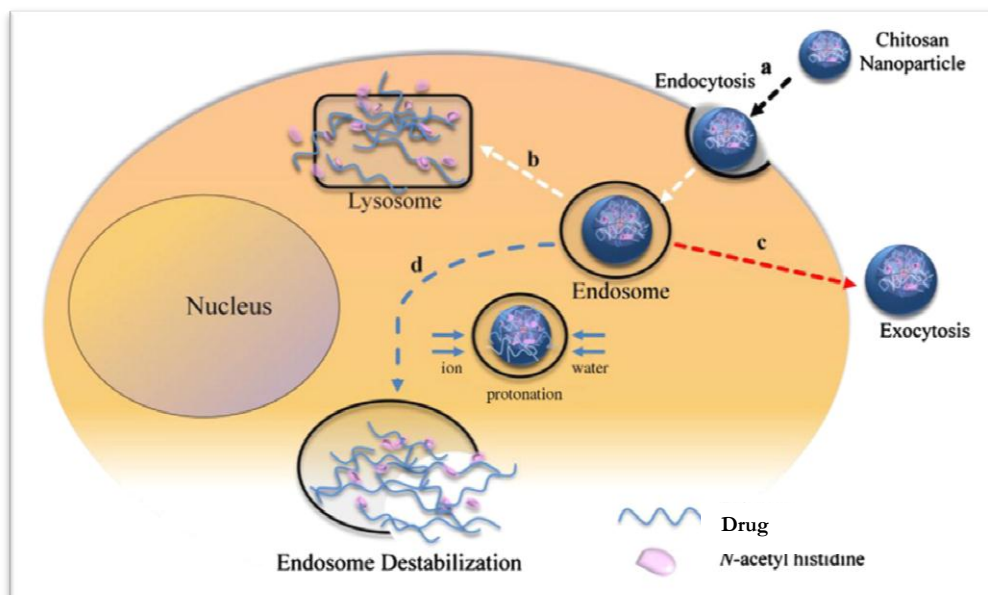


Figure 1.15. Schematic representation of the cellular uptake and drug release from chitosan nanoparticles. Internalization of nanoparticles is initiated by interactions between nanoparticles and cell membranes. Some of the nanoparticles are exocytosed. Drug-loaded nanoparticles are routed to lysosomes, where a high level of lysosomal enzymes is present. Drugs sensitive to these enzymes are degraded and lose their activity. Under slightly acidic environments, the protonated groups cause the disruption of endosomal membranes and simultaneous delivery of drugs into the cytosol (Park *et al.*, 2010).

1.3.5. Toxicity of Nanoparticles

In general, the coating, size, surface area, composition, and shape of a nanoparticle are the most important characteristics determining the cytotoxicity. The surface modifications of nanoparticles are the key tool to minimize toxicological effects.

The general rule for magnetic nanoparticle applications is that the nanocarrier should be non-toxic, non-immunogenic, and at a size that avoids embolization of capillary ducts. Once a nanoparticle enters the bloodstream, opsonization processes activate the RES response. Circulating mononuclear phagocytes carry the nanoparticles to the liver, spleen, and bone marrows where the nanoparticles are metabolized by resident cells (e.g. Kupffer cells in the liver). Depending on size and biodegradability, some of the nanoparticles present in the lysosomal vesicles of Kupffer cells may be incorporated into the bile and be excreted in the feces. Other nanoparticles will be filtered by the kidneys and excreted by the urine.

Generally, smaller nanoparticles are subjected to renal elimination rapidly, while larger nanoparticles taken up by the liver, spleen and bone marrow (Figure 1.16). Larger nanoparticles are cleared by phagocytic cells (i.e. by macrophages or dendritic cells), while smaller nanoparticles are cleared by endocytic cells (i.e. by B and T lymphocytes). The decomposition products of biodegradable magnetic nanoparticles are taken up by any cell with pinocytosis (Macaroff *et al.*, 2006; Neuberger *et al.*, 2005).

According to Neuberger *et al.*, “magnetic particles smaller than 4 μm are removed by cells of the RES, mainly in the liver (60-90%) and spleen (3-10%). Particles larger than 200 nm are usually filtered to the spleen, whose cut-off point extends up to 250 nm, while particles up to 100 nm are mainly phagocytosed through liver cells. In general, the larger the particles are, the shorter their plasma half life period. This clearance of particles by Kupffer cells can be useful for the treatment of liver diseases, such as cancer or leishmania, tuberculosis, listeria although it is important to consider that it would simultaneously entail the depletion of a significant number of the patient’s own defense cells” (Neuberger *et al.*, 2005).

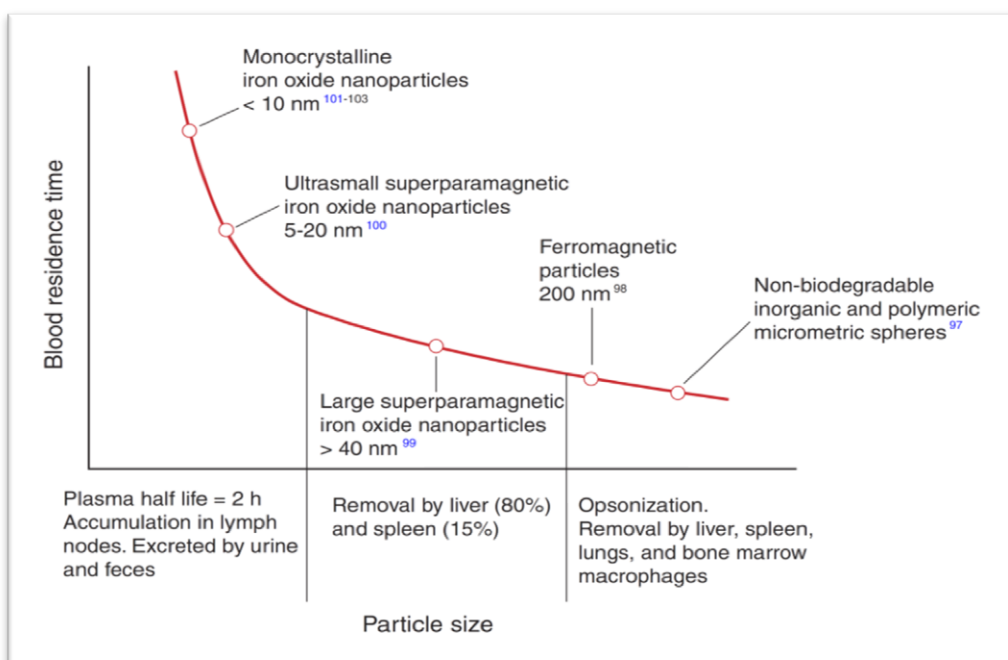


Figure 1.16. Graph of particle size versus blood residence time of nanoparticles (Arruebo *et al.*, 2007).

Before the preclinical tests of a magnetic nanocarrier for targeted drug delivery, it is necessary to analyze their *in vitro* and *in vivo* toxicity (acute, subacute, and chronic toxicity, teratogenicity, and mutagenicity); hematocompatibility; biodegradation; immunogenicity; and pharmacokinetics (body distribution, metabolism, bioavailability, organ specific toxicity) of the magnetic nanoparticle as a vector (Macaroff *et al.*, 2006).

CHAPTER2

MATERIALSAND METHODS

2.1. Materials

Iron (II) chloride tetrahydrate ($\text{FeCl}_2 \cdot 4\text{H}_2\text{O}$), iron (III) chloride hexahydrate ($\text{FeCl}_3 \cdot 6\text{H}_2\text{O}$), Chitosan (LMW, 85% deacetylated) were purchased from Sigma-Aldrich (U.S.A). Sodium tripolyphosphate (TPP, Sigma-Aldrich Chemie GmbH, Germany) was provided by Assoc. Prof. Dr. Ayşen TEZCANER's Lab. Ammonium hydroxide solution (32%, NH_4OH) acetic acid (CH_3COOH), was obtained from Merck (Germany). Nitrogen gas was provided from AsyaGaz (Turkey). Bortezomib (Velcade®) was kindly provided by Janssen-Cilag. Doxorubicin (Adriamicin®) was obtained.

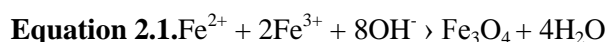
The parental MCF-7 human breast cancer cell line was donated by the ŞAP Institute, Ankara, Turkey. $1\mu\text{M}$ Doxorubicin Resistant MCF-7 cell line (MCF-7/Dox) was previously developed from MCF-7 cells (MCF-7/S) by continuous drug applications (Kars *et al.*, 2006) in our laboratory. SiHa human cervical squamous carcinoma cell line was purchased from ATCC. HeLa human cervical squamous carcinoma cell line was kindly provided by Assoc. Prof. Dr. Elif ERSON BENSAN's Lab.

Eagle's MEM medium was purchased from ATCC, USA. RPMI medium and fetal bovine serum (FBS) were obtained from Biochrom AG, Germany. Trypsin-EDTA, Gentamycin sulphate, Trypan blue and XTT cell proliferation kit were purchased from Biological Industries, Israel. Phosphate buffered saline (PBS) and dimethyl sulfoxide (DMSO) were obtained from Sigma-Aldrich, USA. Ethyl alcohol was provided from Dop Organik Kimya, Turkey.

2.2. Methods

2.2.1 Synthesis of Bare Magnetic Nanoparticles (MNPs)

In this study, precipitation method (Liu *et al.*,2006, Unsoy *et al.*,2012), was employed, while different methods are present to synthesize magnetic nanoparticles; such as: microemulsion, precipitation, laser pyrolysis, sol-gel, thermal decomposition methods, in the literature, (Gupta & Gupta, 2005). In precipitation method, particles are usually obtained by addition of a base into aqueous solution of Fe (II) and Fe (III) salts. The chemical reaction of Fe₃O₄ precipitation is given in Equation 2.1 (Bumb *et al.*,2008).



Magnetic iron oxide (Fe₃O₄, magnetite) nanoparticles were synthesized by the precipitation of Fe(II) and Fe(III) salts at a 1:2 ratio in 150 ml deionized water within a five necked glass balloon (Figure 2.1). Glass flask is placed on a heating mantle and stirred by a glass rod of mechanical stirrer (Heildolf RZR 2021, Germany), which is inserted into the middle neck of the flask. It is vigorously stirred in the presence of nitrogen (N₂) gas flow at 90°C. The nitrogen gas prevents oxidation. Ammonium hydroxide (NH₄OH) is added to the system dropwise by a peristaltic pump. This process is ended by washing step with deionized H₂O until the solution pH reached to 9.0.

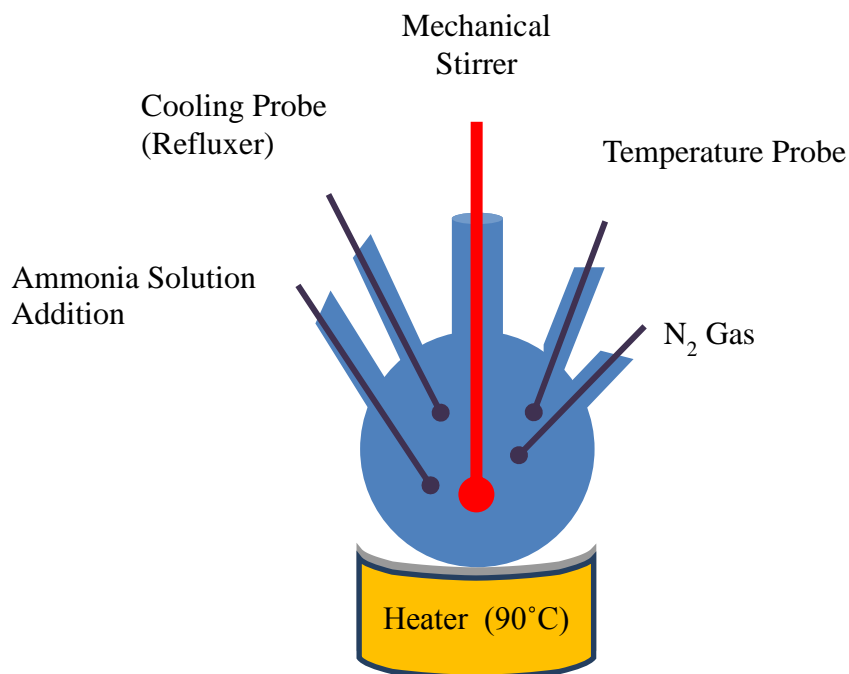


Figure 2.1. The scheme of the experimental setup for Bare MNP synthesis (Keskin, 2012).

For the optimization of synthesis method, system temperature was changed between 20°C – 90°C at 10°C intervals and the crystal structures of synthesized nanoparticles at different temperatures were analyzed by XRD.

2.2.2 In Situ Synthesis of Chitosan coated Magnetic Nanoparticles

Chitosan coated magnetic iron oxide nanoparticles were in situ synthesized by the precipitation of Fe(II) and Fe(III) salts in the presence of chitosan and TPP molecules according to Unsoy *et al.* (2012). TPP was used for the crosslinking of low molecular weight chitosan polymers. Chitosan (0.15 g) was dissolved in 30 ml of 1% acetic acid, and the pH was adjusted to 4.8 by 10 M NaOH. Iron salts (1.34 g of FeCl₂·4H₂O and 3.40 g of FeCl₃·6H₂O) were dissolved in 30 ml of 0.5% chitosan solution. Under the nitrogen (N₂) gas flow and by vigorously stirring at 2500 rpm, 10 ml of 7.5% TPP and different amounts of 32% NH₄OH (18, 20, 25, and 30 ml) were added to the solution to obtain the final NH₄OH concentrations of 31% (CS MNP-S₁), 33% (CS MNP-S₂), 38.5% (CS MNP-S₃), and 43% (CS MNP-S₄) at room temperature (Figure 2.2). The ammonia solution was added dropwise and very slowly to produce smaller sized nanoparticles by a peristaltic pump at the same rate for each synthesis. The resulting solution was stirred for an additional 1 hour. The colloidal chitosan coated magnetic Fe₃O₄ nanoparticles were extensively washed with deionized water and separated by magnetic decantation for several times.

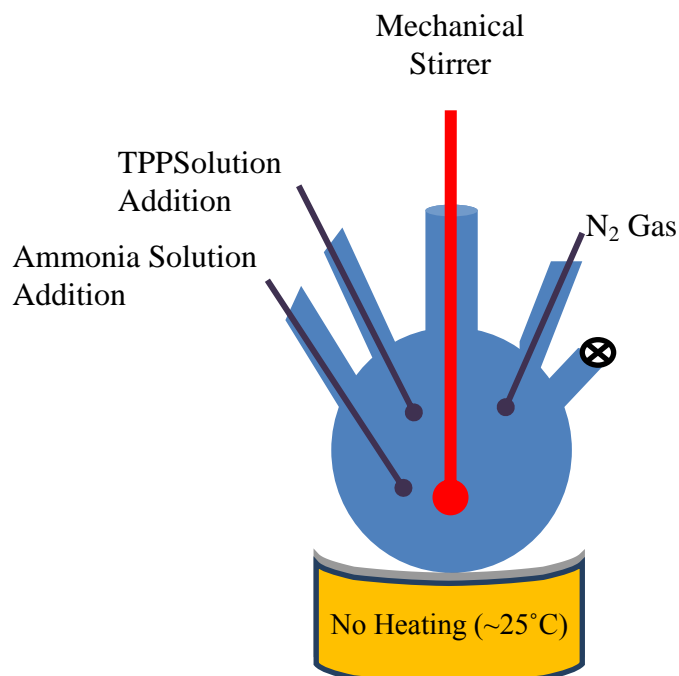


Figure 2.2. The scheme of the experimental setup for CS MNP synthesis (Keskin, 2012).

In the acidic media, the protonated amino groups of chitosan interact with anionic TPP through electrostatic attraction and chitosan TPP gel forms (Lee *et al.*, 2001). TPP has pH dependent ionization behavior owing to different pKa values. Ionization degree of TPP ions has strong influence on the mechanism of ionotropic gelation by coagulation/crosslinking of protonated chitosan (Martell *et al.*, 2004). Actually, protonated chitosan forms chitosanTPP complex through ion pair formation with the uptake of TPP ions. The amount of TPP ion uptake is highly pH dependent owing to their pH dependent degree of ionization. In alkaline pH, protonated chitosan (pKa 6.3) precipitates out from solution through neutralization by pH induced deprotonation (Zemskova *et al.*, 2005). While considering the gelation kinetics of chitosan TPP systems at different pH conditions, the complex viscosity at pH 8.6 was found to be higher than that of pH 3.0. This mainly occurs due to simultaneous cross linking of chitosan with TPP ions and neutralization through deprotonation at pH 8.6 resulting in phase separation (Figure 2.3).

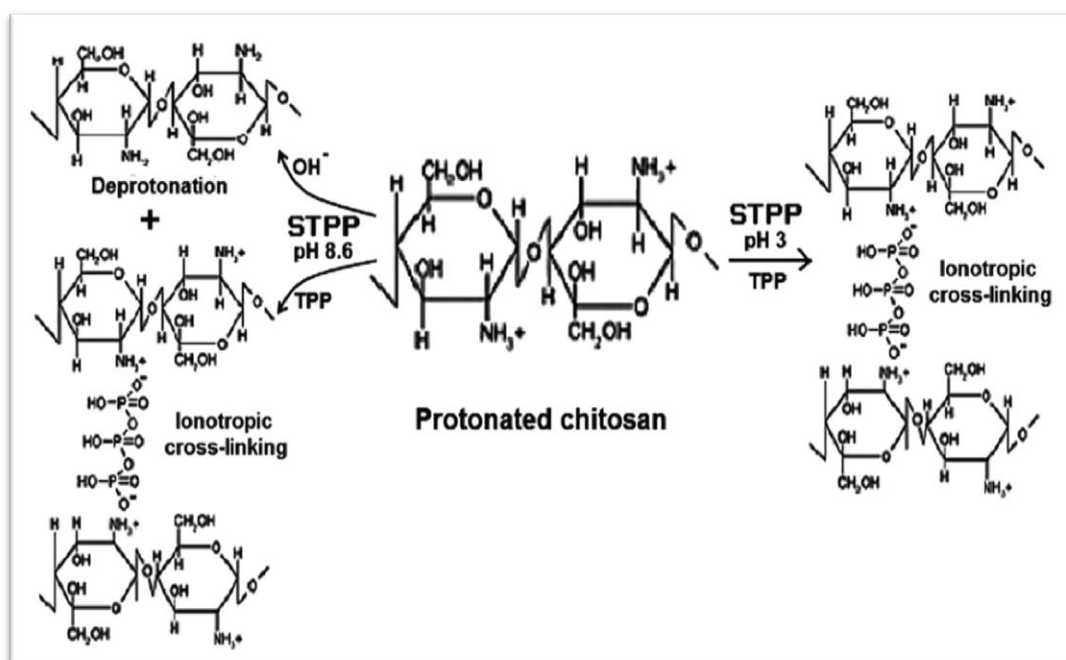


Figure 2.3. pH effect on ionotropic cross linking and deprotonation (Pati *et al.*, 2011).

In pH 3, NH₃⁺ of chitosan interact with anionic TPP and ionotropic cross linking occurs. In pH 8.6, less crosslinking occurs due to the pH induced deprotonation of chitosan. Increased stability is attributed to strong intra and inter molecular ionic cross linking of protonated amines of chitosan with TPP. Under the same TPP concentration, degree of crosslinking increased with decreasing pH, increase in degree of crosslinking results in a more compact, less porous structure (Pati *et al.*, 2011). However, for an efficient drug loading and release, basic reaction conditions were preferred so that, more porous structure is obtained.

In order to analyse the pH effect on the synthesis of CS MNPs, only the amounts of NH_4OH were changed, while the other system conditions were the same. Different amounts of NH_4OH were added to the solution to obtain NH_4OH concentrations of 31% (CS MNP-S₁), 33% (CS MNP-S₂), 38.5% (CS MNP-S₃) and 43% (CS MNP-S₄) and obtained CS MNPs were at different sizes (Unsoy *et al.*, 2012).

2.2.3 Characterization of Bare and Chitosan Magnetic Nanoparticles

X-Ray Diffraction (XRD), Fourier Transform Infrared Spectroscopy (FTIR), X-ray Photoelectron Spectroscopy (XPS/ESCA), Scanning Electron Microscopy (SEM), Transmission Electron Microscopy (TEM), Vibrating Sample Magnetometer (VSM), Thermal Gravimetric Analysis (TGA-FTIR), Dynamic Light Scattering (DLS) and Zeta Potential measurements were employed to characterize the synthesized nanoparticles. Crystal structures of synthesized MNPs were analysed by XRD method. The chemical groups and chemical interactions involved in synthesized MNPs were identified with FTIR and XPS methods. The sizes of MNPs were measured with DLS, their shapes and sizes were observed by TEM/SEM images. Magnetic properties of MNPs were determined by VSM analysis. TGA results indicated the chitosan content of CS MNPs by weight. Cellular uptake of CS MNPs were investigated with fluorescent IgG modifications by Confocal Laser Scanning Microscope (Leica DM 2500). Cytotoxicity of bare and CS MNPs were analyzed by Cell Proliferation Assay with XTT Reagent.

2.2.3.1 X-Ray Diffraction (XRD)

X-ray diffraction is used for the phase identification of crystal materials and provide information about average dimensions of nanocrystals. XRD (Rigaku Ultima-IV X-Ray Diffractometer) was performed to understand crystal structure of the synthesized bare and chitosan coated Fe_3O_4 nanoparticles.

2.2.3.2 X-Ray Photoelectron Spectroscopy (XPS, ESCA)

X-ray photoelectron spectroscopy provides elemental and chemical spectroscopic analysis with high resolution at elemental sensitivity by recording surface composition while using an ion gun to gradually remove surface layers of nanoparticles.

Fe_3O_4 (magnetite) and $\gamma\text{-Fe}_2\text{O}_3$ (maghemite) reflect similar XRD patterns because both have inverse spinel structure. So, XRD by itself is not an ideal method to discriminate the certain crystalline forms of iron-containing nanoparticles, such as, Fe_3O_4 and $\gamma\text{-Fe}_2\text{O}_3$. Therefore, XPS was used to examine shell structure of the synthesized product because core electron lines of ferrous and ferric ions can both be detectable and distinguishable in XPS.

2.2.3.3 Fourier Transform Infrared (FTIR) Spectroscopy

Fourier Transform Infrared Spectroscopy were used to understand the chemical composition of the bare, chitosan coated, Doxorubicin loaded and Bortezomib loaded chitosan coated magnetic nanoparticles. 0.2 g sample was compressed with 0.18 g KBr to form into pellets. These pellets were analyzed in FTIR instrument (Thermo Scientific, Nicolet 6700)

2.2.3.4 Transmission Electron Microscopy (TEM)

Transmission Electron Microscopy (FEI - Tecnai G2 F30 TEM and FEI - 120kV HCTEM) was employed to visualize the shape and size of bare and chitosan coated nanoparticles. An image is formed from the interaction of the electrons transmitted through an ultra-thin specimen in this microscopy technique.

2.2.3.5 Freeze Drying

Freeze-drying is a dehydration process, working by freezing the material and then reducing the surrounding pressure to allow the frozen water in the material to sublime directly from the solid phase to the gas phase.

After the drug loading studies,if the loading capacity of nanoparticles found inefficient, increasing the porosity of nanocarriers by freeze drying would be an effective solution. The freeze drying process was applied on CS MNPs in order to observe the formation of a porous, sponge like structure so that the drug loading capacity of nanocarriers is increased.

2.2.3.6 Scanning Electron Microscopy (SEM)

Scanning electron microscopes scan the surface of sample line by line with a fine probe of electrons and,give information about sample's surface topography and composition. SEM images of synthesized bare and chitosan coated nanoparticles were taken in order to visualize the surface properties and size dispersion of nanoparticles.

2.2.3.7 Dynamic Light Scattering (DLS)

Dynamic light scattering provides information about size, shape, and flexibility of particles as well as offering insight concerning the interactions between particles and their environments. It measures the hydrodynamic particle sizes in the dispersion medium. DLSwas operated to determine the hydrodynamic particle sizes and size distribution profiles of bare and chitosan coated nanoparticlesin a suspension.

2.2.3.8 Zeta (ζ) Potential

The zeta potential values of the bare and chitosan coated MNPs (CS MNP-S₁) were measured with Zetasizer Nano (Malvern Instruments Co., UK), in aqueous NaCl solutions at pH 3.0–11.0 (adjusted by NaOH or HCl).

2.2.3.9 Vibrating Sample Magnetometer (VSM)

Vibrating Sample Magnetometer (EV/9, ADE Magnetics) was used to determine the magnetic properties of bare and chitosan coated magnetic nanoparticles. VSM also supplies the hysteresis curves for the magnetic nanoparticles.

2.2.3.10 Cellular Uptake of FITC Modified CS MNPs

The CS MNPs were conjugated with fluorescein isothiocyanate (FITC) to observe cellular uptake. The conjugation process was carried out with the surface activation method of EDC (ethyl(dimethylaminopropyl)carbodiimide) and NHS (N-Hydroxysuccinimide) (Acharya *et al.*, 2009). FITC conjugated CS MNPs were formed and incubated with MCF-7 cells prior to imaging. After washing the cells with PBS, they were observed by Confocal Laser Scanning Microscope (Leica Microsystems DM 2500).

2.2.3.11 Cytotoxicity of Bare and CS MNPs

Cytotoxicity of bare and CS MNP-S₁ (750 $\mu\text{g}/\text{ml}$) on HeLa, SiHa human cervical cancer cell lines and MCF-7, MCF-7/Dox human breast cancer cell lines were determined by Cell Proliferation Assay with XTT Reagent. Experiments performed in triplicates and conditions are explained in part 2.2.6 in details. Results were statistically evaluated with GraphPad Prism 5 Software to determine significant differences between mean of the groups ($P \leq 0.05$). One-way ANOVA, two-way ANOVA, Tukey tests were carried out.

2.2.4 Drug Loading, Release and Stability of CS MNPs

Drug loading experiments were started with an anticancer agent Doxorubicin, because of the fluorescent properties and presence of the drug in our Laboratory. Later on, Bortezomib was kindly provided by Janssen and Cilag and drug loading studies on CS MNPs were carried out with Bortezomib (Figure 2.4).

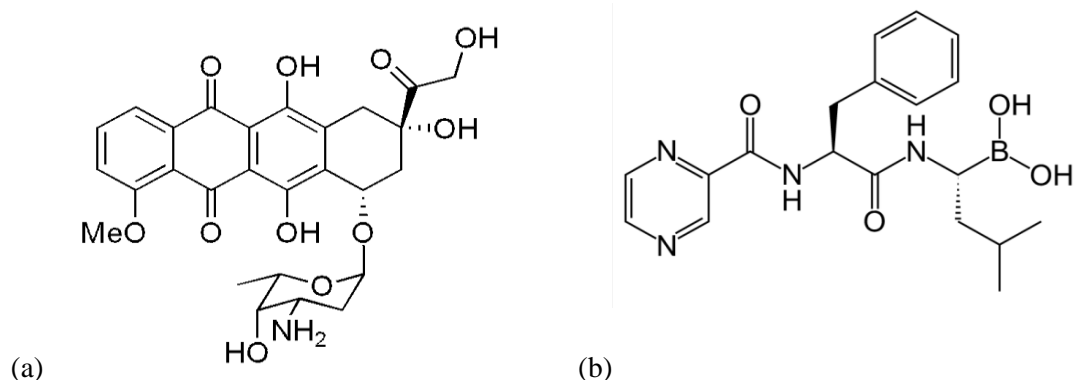


Figure 2.4. Molecular formulas of Doxorubicin (a) and Bortezomib (b).

2.2.4.1 Doxorubicin Loading

2.2.4.1.1 Loading of Doxorubicin on CS MNPs

Doxorubicin loading on CS MNPs (S₁.S₄) was performed in potassium phosphate buffer (K₂HPO₄/KH₂PO₄) with different drug concentrations in order to obtain the highest loading efficiency. The mixture of CS MNPs, Doxorubicin and buffer was rotated (Biosan Multi RS-60 Rotator) at 90 rpm with 5 seconds vibration intervals for 24 hours in the light protected tubes at room temperature.

After the incubation period, Doxorubicin loaded CS MNPs were separated by magnetic decantation and the drug loading efficiency was quantified by measuring the amount of drug remained in supernatant with a UV spectrophotometer (Multiskan GO, Thermo Scientific) at 481 nm (Equation 2.2). The standard curve for Doxorubicin was constructed by measuring the absorbance values of known and diluted concentrations of the drug.

Equation 2.2.

$$\text{Loading Efficiency (\%)} = \frac{(\text{total } \mu\text{g of drug added}) - (\mu\text{g of drug in supernatant})}{(\text{total } \mu\text{g of drug added})} \times 100$$

Doxorubicin loading was also confirmed by FTIR analyses and the schematic representation of Doxorubicin loaded CS MNPs were given in Figure 2.5.

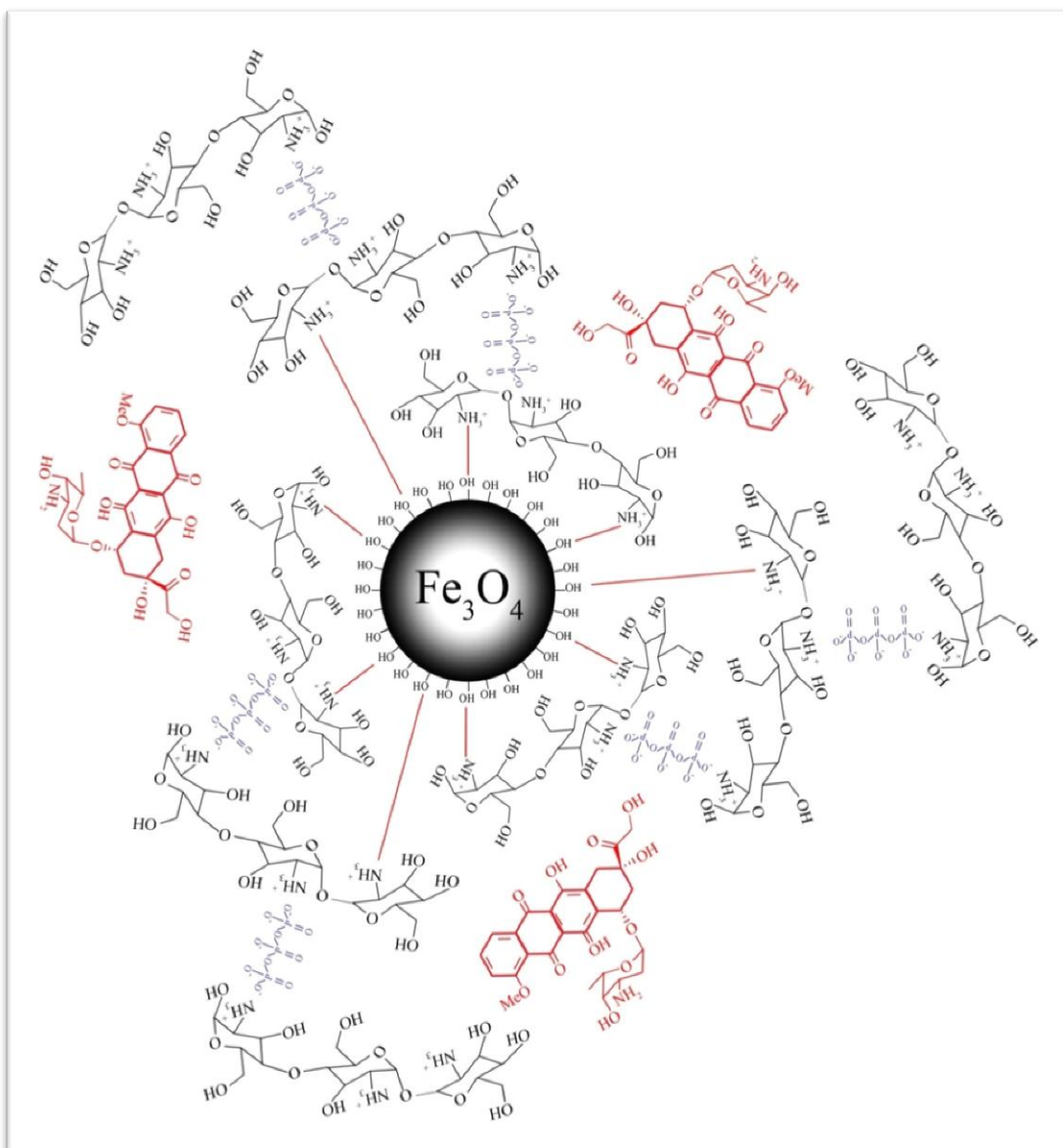


Figure 2.5. Schematic representation of Doxorubicin loaded CS MNPs.

2.2.4.1.1 Stability of Doxorubicin loaded CS MNPs

The stability of CS MNPs loaded with the highest amounts of Doxorubicin was determined in PBS buffer (pH 7.4) up to 8 weeks at 37°C. The Doxorubicin release from nanoparticles in PBS buffer was measured by a UV spectrophotometer (Multiskan GO, Thermo Scientific) at 481 nm.

2.2.4.1.2 Release of Doxorubicin from CS MNPs

The release of Doxorubicin from 400 and 500 µg/ml drug loaded CS MNPs were analyzed in acetate buffer at two different pH values (pH 4.2 and pH 5.0), up to 30 hours at 37°C. The amount of released Doxorubicin from CS MNPs was determined by measuring the absorbance of the supernatant within time intervals at 481 nm by a UVspectrophotometer (Multiskan GO, Thermo Scientific). Quantification of Doxorubicin was performed by generating a calibration curve with known amounts of drug concentrations.

2.2.4.1.3 Cellular Uptake of Doxorubicin Loaded CS MNPs

Synthesized and Doxorubicin (500 µg/ml) loaded CS MNP-S₁ nanoparticles were applied on MCF-7/S and MCF-7/1µM Dox resistant breast cancer cell lines and cellular uptake of nanoparticles were observed. The cells were allowed to adhere to a glass cover slip inplates by incubation for 12 h at 37°C in a humidified incubator maintained with 5% CO₂. Cells were treated with Doxorubicin loaded CS MNPs for 12 h. Then, the cells were washed with PBS. The cover slips were then mounted on microscope slides after the addition of DAPI for cell nuclei staining (DAPI nucleic acid stain, Invitrogen) and washing steps. Images were acquired by Fluorescence Microscope (Leica, Germany) with the appropriate filters.

2.2.4.1.4 Cytotoxicity of Doxorubicin loaded CS MNPs

Cytotoxicity of Doxorubicin loaded CS MNPs on MCF-7, MCF-7/Dox human breast cancer cell lines were determined by Cell Proliferation Assay with XTT Reagent. The experiment conditions are explained in Part 2.2.6 in details.

2.2.4.2 BortezomibLoading

2.2.4.2.1 Loading of Bortezomibon CS MNPs

Bortezomib loading on CS MNP-S₁ was performed in potassium phosphate buffer (K₂HPO₄/KH₂PO₄) with different drug concentrations in order to optimize the loading efficiency. The mixture of CS MNPs, Bortezomib and buffer was rotated (Biosan Multi RS-60 Rotator) at 90 rpm with 5 seconds vibration intervals for 24 hours in light protected tubes at room temperature. Bortezomib loaded CS MNPs were seperated by magnetic decantation and the drug loading efficiency was quantified by measuring the unloaded drug amount in supernatant with a UV spectrophotometer (Multiskan GO, Thermo Scientific) at 270 nm (Eq.1). The standard curve for Bortezomib was constructed by measuring the absorbance values of known and diluted concentrations of the drug. Bortezomib loading was also confirmed by FTIR analyses and the schematic representation of Bortezomib loaded CS MNPs were given in Figure 2.6.

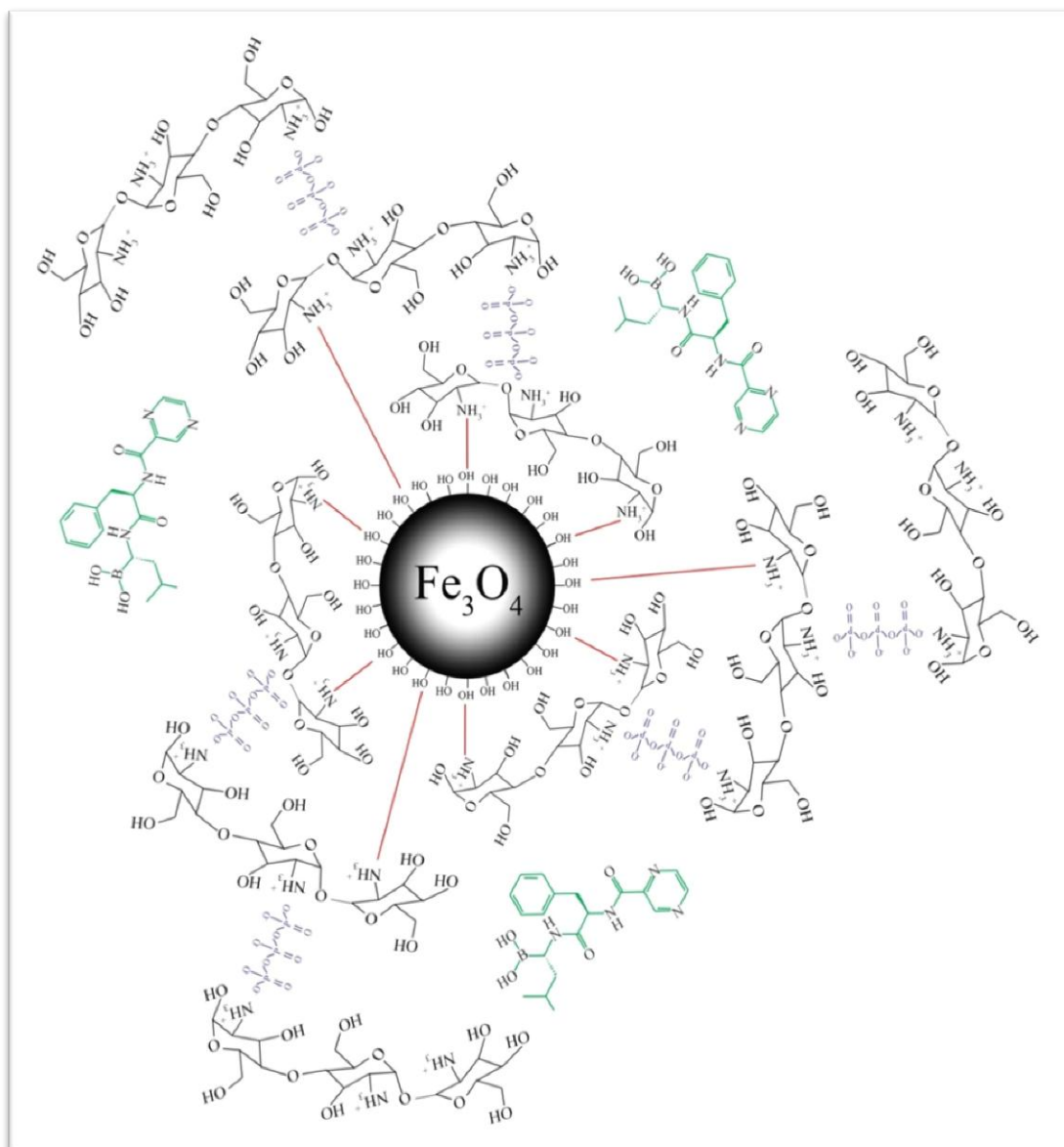


Figure 2.6. Schematic representation of Bortezomib loaded CS MNPs.

2.2.4.2.2 Stability of Bortezomibon CS MNPs

The stability of CS MNPs loaded with the highest amounts of Bortezomib was determined in PBS buffer (pH 7.4) up to 8 weeks at 37°C. The Bortezomib release from nanoparticles in PBS buffer was measured by a UV spectrophotometer (Multiskan GO, Thermo Scientific) at 270 nm.

2.2.4.2.3 Release of Bortezomib from CS MNPs

The release of Bortezomib from 400 and 500 µg/ml drug loaded CS MNPs were analyzed in acetate buffer at two different pH values (pH 4.2 and pH 5.0), up to 30 hours at 37°C. The amount of released Bortezomib from CS MNPs was determined by measuring the absorbance of the supernatant within time intervals at 270 nm by a UV spectrophotometer (Multiskan GO, Thermo Scientific). Quantification of Bortezomib was performed by generating a calibration curve with known amounts of drug concentrations.

2.2.4.2.4 Cytotoxicity of Bortezomib loaded CS MNPs

The antiproliferative effects of Bortezomib loaded CS MNPs on HeLa and SiHa human cervical cancer cell lines were evaluated by means of Cell Proliferation Assay with XTT Reagent. The experiment conditions are explained in Part 2.2.6 in details.

2.2.5 Cell Culture

2.2.5.1 Cell Lines and Culture Conditions

The immortal cancer cells lines are widely used for basic science and preclinical studies for years. MCF-7 cells, derived from a 69 year old Caucasian breast cancer patient, have been characterized extensively at the genomic and gene expression levels (Cavaillès *et al.*, 2002; Rinehart-Kim *et al.*, 2000) and, more recently, at the protein levels (Harris *et al.*, 2002; Vercoutter-Edouart *et al.*, 2001; Hathout *et al.*, 2002). MCF-7 cells are ER⁺ cells.

The MCF-7/Dox, the Doxorubicin resistant variant of the MCF-7 cells, was previously established in GUNDUZ Lab by stepwise selection of cells after prolonged treatment to increasing concentrations (1 µM, final dose) of Doxorubicin within the medium (Kars *et al.*, 2006). The IC₅₀ (inhibitory concentration to produce 50% cell death) values of MCF-7/Dox cells increases with the acquired resistance. Drug resistance is commonly caused by the inhibition of drug entrance to the cell via the efflux pumps or the loss of cell's ability to enter apoptosis.

HeLa (transformed with HPV-18) and SiHa (transformed with HPV-16) cervical carcinoma cell lines were chosen as model systems for examining the drug efficacies due to the known biological/genetic properties and stability of their endogenous HPV genomes. HeLa cell line, derived from cervical adenocarcinoma cells taken on 1951 from Henrietta Lacks (Scherer *et al.*, 1953), is the oldest and most commonly used human cell line (Rahbari *et al.*, 2009). HeLa cells have 10-50 copy HPV-18 genome integrated on its chromosome as three subgenomic fragments. SiHa cells were obtained from the squamous cell carcinomas of an Asian female and have 1-2 copy HPV-16 genome integrated as single genomic fragments on its chromosome (Meissner *et al.* 1999).

Parental MCF-7 and MCF-7/Dox human breast cancer and HeLa human cervical cancer cell lines are maintained in 1640 RPMI medium (Biochrom AG, Germany) with 10% (v/v) heat-inactivated fetal bovine serum (FBS) (Biochrom AG, Germany) and 10% (v/v) Gentamycin Sulfate Solution (Biological Industries, Israel). SiHa human cervical cancer cell line is maintained in Eagle's MEM medium (ATCC, USA) with 10% (v/v) FBS and 10% (v/v) Gentamycin Sulfate Solution (Biological Industries, Israel) in T-25 or T-75 tissue culture treated filter cap flasks (Greiner Bio-One, Germany). These cell cultures are incubated in a Heraeus incubator (Hanau, Germany) at 37°C in a 95% (v/v) humidified atmosphere with 5% (v/v) CO₂. The cell culture experiments are performed under a sterile laminar flow (BioAir, Italy). The solutions used in cell culture are cell culture grade and the equipments are presterilized and disposable.

2.2.5.2 Harvesting Cells and Subculturing

When the attached cell concentration on flask surface reached 80% confluency and cells have reached a population density which suppresses their growth, cells are subcultured under sterile conditions. The cell to cell and cell to substrate interactions are dissociated by trypsinization in routine subculturing procedure. The old medium is discarded from the culture flasks, cells are washed with PBS to remove the traces of serum which inactivates trypsin and Trypsin-EDTA (0.5 ml for 25 cm² and 1 ml for 75 cm² culture flasks) is added on cells. The flasks are incubated at 37°C until the detachment of cells is observed on the flasks. Fresh growth medium (amount depending on downstream processes) is added and detached cells are homogenized. These cells can be passed into new culture flasks or harvested for further experiments or frozen for storage.

2.2.5.3 Freezing Cells and Thawing Frozen Cells

Trypsinated and detached cells are resuspended in 4 ml of medium and centrifuged at 1000 rpm for 5 min. Supernatant was discarded and cells are resuspended in 1 ml of cold freezing medium (90% (v/v) complete growth medium supplemented with 10% (v/v) DMSO (Sigma-Aldrich, USA)) to have a final concentration of approximately 2×10^6 cells per ml. This cell suspension is transferred into the cryovials (Greiner) and maintained at 4°C for 30 min, then kept in -20°C for 3-4 hours before the overnight incubation at -80°C. Finally cryovials were transferred to liquid nitrogen containers for long term storage.

For the thawing of frozen cells, cryovials, taken from -80°C or nitrogen tank, are immediately transferred to 37°C. Since the DMSO is toxic to the cells above 4°C, it is very important to thaw the cells quickly at 37°C. Then, the cell suspension is transferred dropwise to new cell culture flask containing fresh medium. Cells are homogenized by pipetting and maintained in defined growth conditions. It is allowed the cells to attach for the first 24 hours before changing the medium to remove residual DMSO.

2.2.6 Cell Proliferation Assays

2.2.6.1 Viable Cell Counting

The determination of cell number in 1 ml cell suspension is important for seeding equal number of cells at each well in cell proliferation assays. The reactivity of Trypan Blue dye (Sigma-Aldrich) is based on the fact that the chromophore is negatively charged and does not interact with the cell unless the membrane is damaged (Strober, 2001). Therefore, viable cells exclude the dye and the dead cells are stained into blue. The cell suspension was mixed with Trypan Blue solution (0.5%) with a ratio of 9:1 and counted in a Neubauer hemacytometer (Bright-line, Hausser Scientific, USA) under phase contrast microscopy (Olympus, USA).

2.2.6.2 Cell Proliferation Assay with XTT Reagent

The antiproliferative effects of drug (Doxorubicin and Bortezomib) loaded and unloaded nanoparticles are investigated on MCF-7, MCF-7/Dox, HeLa and SiHa cell lines by Cell Proliferation Kit with XTT Reagent (Biological Industries, Israel) according to manufacturer's instructions.

This is a colorimetric assay which detects the cellular metabolic activities. The yellow XTT (2, 3-bis (2-methoxy-4-nitro-5-sulphophenyl)-2H-tetrazolium-5-carboxanilide) tetrazolium salt is reduced to orange formazan dye by dehydrogenase enzymes produced in mitochondria of metabolically active cells. This conversion does not occur in dead cells and thus, the amount of the formazan produced is proportional to viable cells in the sample. The intensity of formazan compound, measured at 496 nm by microplate reader (Anthos 2010, England), is proportional to the number of living cells in the well.

In brief, cells are seeded into the 96-well microtiter plates (Greiner) starting from the 2nd column at a concentration of 5000 cells per well. In each plate 1st and 2nd columns are used as medium and cell controls, respectively. Highest concentration of analyzed nanoparticle amount is applied to the 3rd column and diluted horizontally through the 12th column. After the incubation of plates, XTT and activator reagents are added, and 4 hours later, the intensity of formazan dye is measured. Cell proliferation curves were constructed by conversion of dye intensity into viability percentages (Figure 2.7).

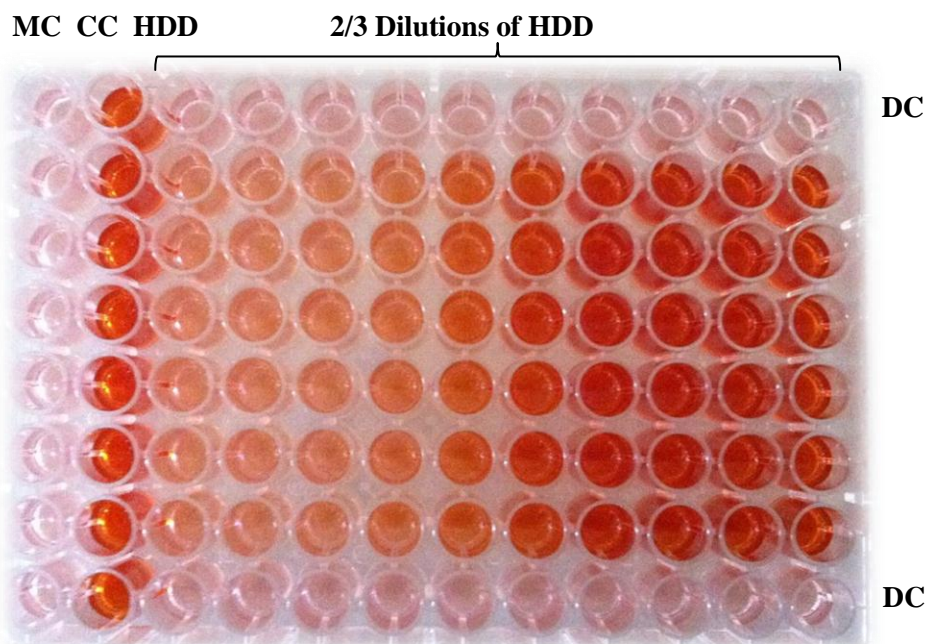


Figure 2.7. Schematic representation of XTT cell proliferation design on 96 well plate (MC: Medium Control, without cell and drug; CC: Cell Control, with cell and without drug; HDD: Highest Drug Dose, with cell and with drug; DC: Drug Control, with drug and without cell).

2.2.6.3 Statistical Analysis

All data represents three independent experiments and they were statistically evaluated by one way ANOVA test and Post hoc Tukey analyses using GraphPad Prism 5 Demo Software (USA) to determine significant differences between the groups ($P \leq 0.05$).

2.2.7 Effect of Drug Loaded CS MNPs on Apoptotic Gene Expressions

Effect of drug loaded/unloaded CS MNPs on apoptotic genes (*Puma*, *Noxa*) and antiapoptotic genes (*Survivin*, *cIAP-2* and *Bcl-2*) expressions were investigated by Real Time (RT) Quantitative PCR Analyses (Rotor-Gene Q, QIAGEN).

Total RNA was isolated (EZRNA RNA Isolation Kit, Israel) from treated MCF-7, MCF-7/Dox, HeLa and SiHa cells. The isolated RNAs were treated with the DNase (Thermo Scientific, USA) and cDNA was synthesized with EasyScript Plus™ cDNA Synthesis Kit (Applied Biological Materials Inc., Canada) according to manufacturer's instructions.

2.2.7.1 Isolation of Total RNA

All the plastic and glassware were treated with DEPC treated ddH₂O prior to RNA isolation, in order to inactivate RNases. Excess DEPC was vaporized under hood for overnight and all the equipments were autoclaved before RNA isolation and cDNA synthesis.

In this part of the study, MCF-7, MCF-7/Dox, HeLa and SiHa cells were seeded in 6 well plates (300,000 cell/well). Then, the cells were incubated overnight, CS MNPs, drugs and drug loaded CS MNPs at the IC₅₀ concentrations were applied to the cells. IC₅₀ (half maximal inhibitory concentration) represents the concentration of a drug that is required for 50% inhibition of cell proliferation. After the 72 hours of incubation periods, total RNA was isolated from treated MCF-7, MCF-7/Dox, HeLa and SiHa cells. Total RNA was extracted with a phenol/chloroform EZRNA kit (Biological Industries, Israel) according to the manufacturer's instructions.

2.2.7.2 Quantification of the Isolated RNA

The concentration and purity of isolated RNA samples were determined by measuring optical densities at 260 nm for nucleic acids and 280 nm for proteins by NanoDrop 2000C spectrophotometer (Thermo Fischer Scientific, USA). Absorbance at 260 nm is used to calculate RNA concentration where the ratio of absorbance at 260 nm to 280 nm indicates purity of RNA. Nucleic acids and proteins give absorbance at 260 and 280 nm, respectively. OD₂₆₀ / OD₂₈₀ were calculated which should be in between 1.6 and 2.1 for pure RNA.

2.2.7.3 Agarose Gel Electrophoresis of RNA

Isolated RNA was detected by horizontal agarose gel electrophoresis on 1% (w/v) agarose. For gel electrophoresis 1.5 g agarose (Applichem, Germany) was dissolved in 150 ml 1xTAE buffer (Appendix C) and boiled in a microwave oven. 7 μl ethidium bromide solution (Appendix C) was added into the gel solution. The gel solution was poured into electrophoresis tray for solidification. 3 μl of RNA sample was mixed with 2x RNA loading buffer (Fermantas, Lithuania) and loaded. 5 μl High Range RNA Ladder was also loaded (Fermantas). Electrophoresis was run with 1 l of 1xTAE buffer at 70 V, for 1.5h. The gel was observed under UV light (VILBER Lourmat UV Transilluminator) and photographed. Gels were evaluated in terms of intactness of RNA and DNA contamination.

2.2.7.4 DNase Treatment of RNA

The isolated total RNAs were treated with DNase (Thermo Scientific, USA) to degrade any DNA contamination. 1 µg RNA, 1 µl Reaction Buffer, 1 µl DNase and required amount of RNAase-free water were used for DNase treatment at 10 µl total volumes. Reaction tubes were incubated at 37°C for 30 minutes. After the first incubation period, 1 µl EDTA was added into the tubes and incubated for 10 minutes at 65°C to stop the activity of DNases. Reaction volume was completed to 11 µl with EDTA.

2.2.7.5 cDNA Synthesis

The DNase treated 1 µg RNA samples within the 11 µl total volume were used as template for cDNA synthesis (EasyScript Plus™ cDNA Synthesis Kit, Applied Biological Materials Inc., Canada).

The master mix for RT PCR includes; 4 µl Reaction Buffer (5x), 1 µl Random hexamer primers (10 µM), 1 µl dNTPs (10mM), 1 µl RTase (200 U/µl), 0.5 µl RNase Inhibitor (40 U/µl) and the volume was completed to 20 µL with RNAase-free water. 9 µl of master mix was distributed to each RNA tubes and the PCR (Thermo Scientific, USA) program was started at the conditions of 25°C for 10 minutes, 50°C for 50 minutes, and 85° C for 5 minutes. After the reaction was completed, the synthesized cDNA tubes are taken on ice and stored at -20°C freezer.

2.2.7.6 Quantitative Real-Time Polymerase Chain Reaction (qPCR)

Real-time PCR (Q-PCR) was carried out in Rotor-Gene QRT-PCR (QIAGEN). This method provides a basis for the determining of the precise concentration of the product as well as preventing the possible end point detection problems of traditional PCR. SYBR Green is a frequently used fluorescent dye which intercalates the double strands of DNA. The accumulation of PCR products in each cycle intensifies the signal generated by the intercalation of SYBR Green (Light Cycler, FastStart SYBR Green, Roche Diagnostics), enabling to monitor the change in the quantity of products.

Briefly, 20 µl reaction mixture contained 10 µl SYBR Green, 4 µl cDNA (500 ng/µl), 0.24 µl (0.3 µM) from each sense - antisense primers and the volume was completed to 20 µL with RNAase free water for *β-actin*; 3 µl cDNA, 0.2 µl from each sense -antisense primers and the volume was completed to 20 µL with RNAase free water for *Bcl-2*; 3 µl cDNA, 0.24 µl from each sense - antisense primers and the volume was completed to 20 µL with RNAase free water for both *Survivin(BIRC5)* and *Noxa*; 5 µl cDNA, 0.12 µl from each sense - antisense primers and the volume was completed to 20 µL with RNAase free water for *cIAP-2(BIRC3)*; 5 µl cDNA, 0.15 µl from each sense - antisense primers and the volume was completed to 20 µL with RNAase free water for *Puma*. Amplification conditions of

these genes are represented in Table 2.1. Each sample amplification were performed in triplicates. A non template control containing dH₂O instead of cDNA was also included to identify any background signal. Amplification plots were displayed by plotting fluorescence versus treshold cycle number.

The melting peaks of all PCR products were determined by melting-curve analysis in order to ensure that only the expected products had been generated. After real time PCR amplification, the machine was programmed to do a melt curve, in which the temperature ramped from 50°C to 99°C raising one degree at each step and the change in fluorescence was measured. All PCR products for a particular primer pair should have the same melting temperature, unless there is a contamination, mispriming or primer dimer.

Table 2.1.Q-PCR conditions of *β-actin*, *Bcl-2*, *Survivin*, *cIAP-2*, *Puma* and *Noxagenes*.

Q-PCR Conditions	Pre-incubation	Denaturation	Annealing	Melting	Cycle #
<i>β-actin</i>	95°C, 10 min	95°C, 15 sec	60°C, 60 sec	50-99°C	30
<i>Bcl-2</i>	95°C, 10 min	95°C, 15 sec	60°C, 60 sec	50-99°C	37
<i>Survivin</i>	95°C, 10 min	95°C, 15 sec	60°C, 60 sec	50-99°C	40
<i>cIAP-2(BIRC3)</i>	95°C, 10 min	95°C, 15 sec	60°C, 60 sec	50-99°C	45
<i>Puma</i>	95°C, 10 min	95°C, 15 sec	60°C, 60 sec	50-99°C	45
<i>Noxa</i>	95°C, 10 min	95°C, 15 sec	60°C, 60 sec	50-99°C	45

Table 2.2. Primer sequences of *β-actin*, *Bcl-2*, *Survivin*, *cIAP-2*, *Puma* and *Noxagenes*.

Primers	Sequences
<i>β-actin Sense</i>	5' CCAACCGCGAGAAGATGA 3'
<i>β-actin Antisense</i>	5' CCAGAGGCGTACAGGGATAG 3'
<i>Bcl-2 Sense</i>	5' TGTGGCCTTCTTTGAGTTC 3'
<i>Bcl-2 Antisense</i>	5' CGGTTTCAGGTACTCAGTCATC 3'
<i>Survivin Sense</i>	5' AGCCAGATGACGACCCCATAGAGG 3'
<i>Survivin Antisense</i>	5' AAAGGAAAGCGCAACCGGACGA 3'
<i>cIAP-2 Sense</i>	5' TCCTGGATAGTCTACTAACTGCC 3'
<i>cIAP-2 Antisense</i>	5' GCTTCTTGCAGAGAGTTTCTGAA 3'
<i>Puma Sense</i>	5' GACCTCAACGCACAGTA 3'
<i>Puma Antisense</i>	5' CTAATTGGGCTCCATCT 3'
<i>Noxa Sense</i>	5' TGATATCCAACTCTTCTGC 3'
<i>Noxa Antisense</i>	5' ACCTTCACATTCCTCTCAA 3'

CHAPTER3

RESULTS AND DISCUSSION

3.1. Characterization of Bare and CS MNPs

The synthesis of nanoparticles with small size and uniform size distribution is a subject of intensive research in recent years. In this study, chitosan magnetic Fe₃O₄ nanoparticles (CS MNPs) were synthesized with four different concentrations of ammonium and in each synthesis homogenous size distributions were obtained at different size ranges. Smallest sized nanoparticles were obtained at highest ammonium concentrations. The average diameters of CS MNPs increased from 58 to 103 nm and the chitosan content increased from 15 to 23% with the decrease of NH₄OH amount during the synthesis. They would be used as magnetic nanocarriers in biomedical applications such as targeted drug delivery, magnetic resonance imaging (MRI), and magnetic hyperthermia.

There are important applications for small sized nanoparticles in the literature. Kim *et al.*, (2005) have synthesized superparamagnetic magnetite by a sonochemical method. These particles were used as MRI agents by combining them with chitosan. These spherical particles were about 15 nm in diameter (Laurent *et al.*, 2010). Kavaz *et al.*, (2010) synthesized chitosan coated Fe₃O₄ nanoparticles in the size of around 150 nm and they loaded Concavalin-A for targeting of cancer cells and Bloemycin as an anticancer agent. The utilization of small sized superparamagnetic nanoparticles for targeted drug delivery applications have been reported in the literature (Neuberger *et al.*, 2005). The synthesized nanoparticles in this study have potential applications for such purposes.

The chitosan coated magnetic nanoparticles were in situ synthesized for lipase immobilization by Wu *et al.*, (2009); however, their synthesis methods were considerably different. Yuwei and Jianlong (2011) synthesized magnetic chitosan nanoparticles by in situ coprecipitation method without TPP for copper removal. In their study, the particle size was found to have much wider size distribution.

The size-tunable synthesis of CS MNPs was performed by in situ precipitation method. This method is very advantageous for biomedical applications (Tiyaboanchai *et al.*, 2007) because of the simple and mild synthesis conditions. The nanoparticles obtained by this method have higher biocompatibility and biodegradability properties than covalently cross linked chitosan (Agnihotri *et al.*, 2004, Park *et al.*, 2010) as it was crosslinked with ionic interactions.

3.1.1. X-Ray Diffraction (XRD)

Optimization studies for the temperature of bare MNP synthesis conditions were conducted between 20°C - 90°C and 90°C was found as optimum temperature. The synthesized iron oxide nanoparticles show amorphous or non crystalline solid characteristics up to 50°C. Over 50°C nanoparticles started to show crystalline characteristics. Fe₃O₄ and FeO(OH) peaks were observed between 60°C and 80°C. The pure Fe₃O₄ phase was achieved by disappearing FeO(OH) at 90°C temperature (Figure 3.1).

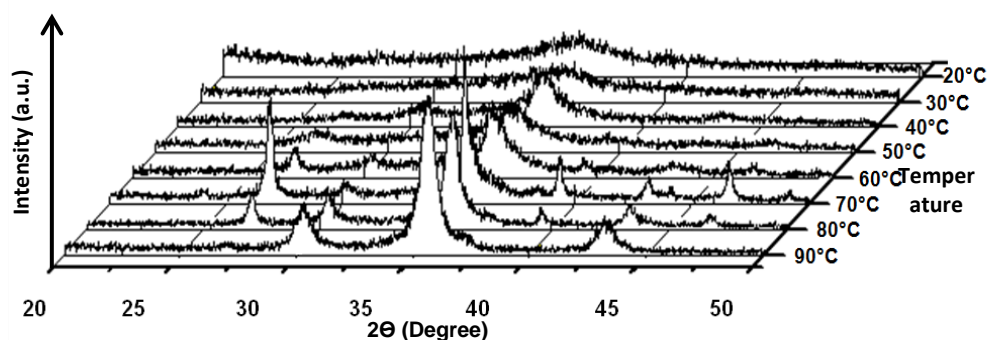


Figure 3.1. XRD patterns of iron oxide nanoparticles synthesized at different temperatures.

X-ray diffraction pattern of Fe₃O₄ nanoparticles appeared at 90°C with diffraction peaks of (220), (311), (400), respectively (Figures 3.1 and 3.2), which are the characteristic peaks of the Fe₃O₄ (magnetite) crystal having a cubic spinel structure.

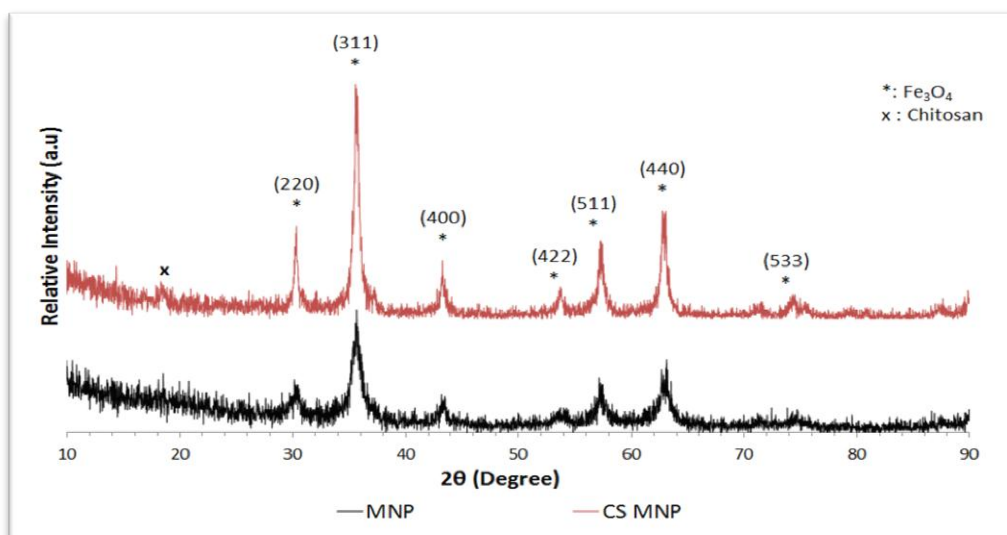


Figure 3.2. XRD patterns of bare and chitosan magnetic nanoparticles.

The resulting core magnetic nanoparticles were found as magnetite (Fe_3O_4) and had cubic spinel structures. No evidence of impurities was found in the XRD pattern. The peaks shown in the XRD pattern of the prepared sample are sharp and intense, indicating good crystallinity of Fe_3O_4 . The XRD spectrum of chitosan is given at several reports in the literature (Li *et al.*, 2005; Lu *et al.*, 2007, Dung *et al.*, 2009). These results are compatible with the reported XRD results in the literature.

Li *et al.*, (2005) reported that chitosan raw material is essentially noncrystalline. In the case of cross linked chitosan, the intensity of characteristic peaks is lower than that of pure chitosan, notified by Wan *et al.*, (2003) and Lu *et al.*, (2007). Because the chitosan is crosslinked by ionic interactions, the intensity of chitosan peak is very low in CS MNPs as it is seen in Figure 3.2, as compatible with the literature. The differences in the diffraction patterns of chitosan and crosslinked chitosan could be attributed to modification in the arrangement of molecules in crystal lattice (Bhumkar and Pokharkar, 2006). Chitosan nanoparticles were composed of a dense network structure of interpenetrating polymer chains cross linked to each other by TPP.

XRD results revealed the presence of the Fe_3O_4 crystals both in bare and chitosan coated magnetite nanoparticles. The peak positions were not changed in CS MNPs, this illustrated the chitosan coating, during the synthesis of nanoparticles, did not make any change in the structure of Fe_3O_4 .

The particle sizes can be quantitatively evaluated from the XRD data using the Debye-Scherrer equation, which gives a relationship between peak broadening in XRD and particle size. $D = k\lambda/(\beta \cdot \cos\theta)$ where, k is Scherrer constant (0.89), λ the X-ray wavelength (nm), β the peak width of half maximum, and θ is the Bragg diffraction angle. The crystallite size of the Fe_3O_4 and chitosan coated Fe_3O_4 nanospheres obtained from this equation were found to be about 18 nm and 8 nm, respectively.

3.1.2. X-Ray Photoelectron (XPS)

XPS analyze was employed because the only XRD is not an ideal method to distinguish the magnetite and maghemite. Figure 3.3 shows representative XPS spectra of the synthesized products. The photoelectron peaks at 711.7 and 725.2 eV are the characteristic doublet of Fe 2p_{3/2} and 2p_{1/2} core-level spectra of iron oxide, respectively, which is consistent with the oxidation state of Fe in Fe₃O₄. These peaks at 711.7 and 725.2 eV were observed in both bare MNPs (Figure 3.3a) and chitosan coated MNPs (Figure 3.3b) (Teng *et al.*,2003; Liu *et al.*,2010; Daou *et al.*,2006).

XPS spectra can identify the absorption sites and the interactions between MNP and CS by the bands obtained from their spectrum. There is no significant peak observed for amino groups in bare MNPs (Figure 3.3a). The XPS spectrum of CS MNP complex was shown in Figure 3.3b. The N1s band of chitosan at 397.7 eV is assigned to amino groups (-NH₂). In CS MNPs, the binding energy at 398 eV was attributed to the amino groups that were involved in hydrogen bond (NH₂-O) which reflects the presence of amino groups of chitosan. The CS MNP complex expressed a new band for N1s at around 400 eV. This new band was assigned to chelation between the amino groups and iron ions (NH₂-Fe). The chelation of CS-Fe₃O₄ demonstrates that the magnetite was coated with chitosan (Wang *et al.*,2009).

XPS spectra can identify the absorption sites and the interactions between MNP and CS by the bands obtained from their spectrum. The binding energies of N1s at 397.7 eV attributed to ‘‘free’’ amino groups (-NH₂) of CS. The atomic fraction of free amino groups (around 398 eV) was 78% (Figure 3.3b).

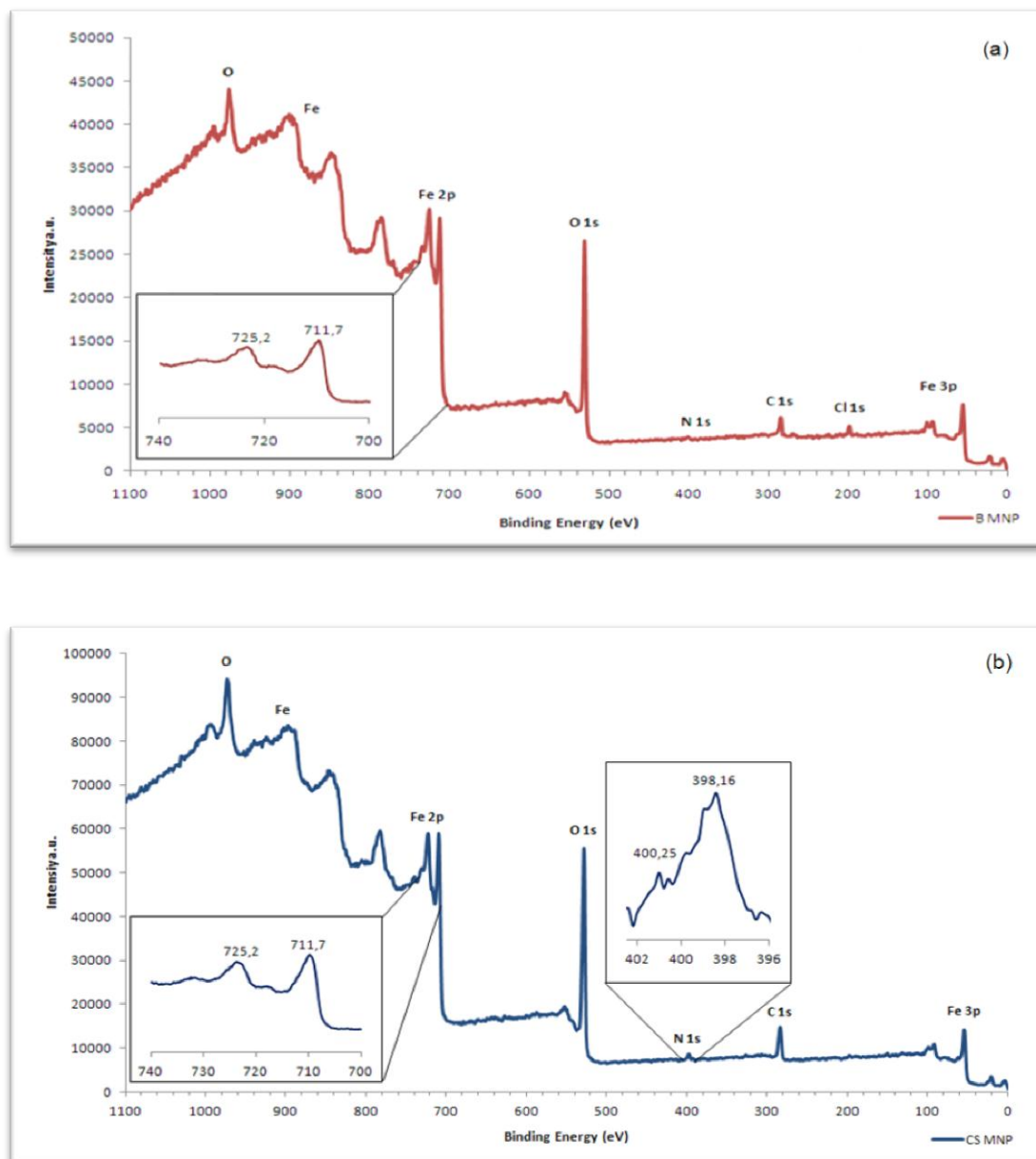


Figure 3.3. X-ray photoelectron spectra of the synthesized magnetic nanoparticles. (a) Bare MNP and (b) Chitosan coated MNP-S₁ (31%). The upper inset is expanded spectrum of N1s in CS MNPs. The lower insets are expanded spectra of Fe 2p.

3.1.3. Fourier transform infrared spectroscopy (FTIR)

Chitosan polymer is coated on iron oxide core by ionic cross linking of TPP crosslinker with chitosan via electrostatic interactions. The coating of MNPs with a layer of chitosan was validated by FTIR. To confirm the chemical composition of synthesized nanoparticles, FTIR spectra were obtained. The FTIR results are given with their auto baseline corrections. The presence of Fe_3O_4 core could be identified by the strong stretching absorption band at 579 cm^{-1} , which corresponded to the Fe–O bond (Figure 3.4 c). The peak located in the 583 cm^{-1} region is found in bare and chitosan coated nanoparticles spectra, confirming that the products contain magnetite. The peaks around $1615 \pm 15\text{ cm}^{-1}$, assigned to the NH_2 group bend scissoring, are present in both chitosan and chitosan coated nanoparticles spectra, proving that magnetite nanoparticles were successfully coated by chitosan polymer (Coates, 2000). In the IR spectrum of chitosan (Figure 3.4 a), the band at 1628 cm^{-1} is assigned to NH_2 group bend scissoring, the peak at 1422 cm^{-1} to OH bending of primary alcoholic group, and 1156 cm^{-1} to C–N stretch in chitosan. In the spectrum of CS MNP (Figure 3.4 b), the 1628 cm^{-1} peak of NH_2 group bend scissoring in chitosan, shifted to 1618 cm^{-1} and a new sharp peak at 583 cm^{-1} was appeared. All characteristic peaks of chitosan and iron oxide were present in the spectrum of CS MNP-S₁. Results indicated that MNPs were successfully coated with chitosan and these results are compatible with the articles in the literature (Li *et al.*, 2008; Zhang *et al.*, 2010a; Ma *et al.*, 2007).

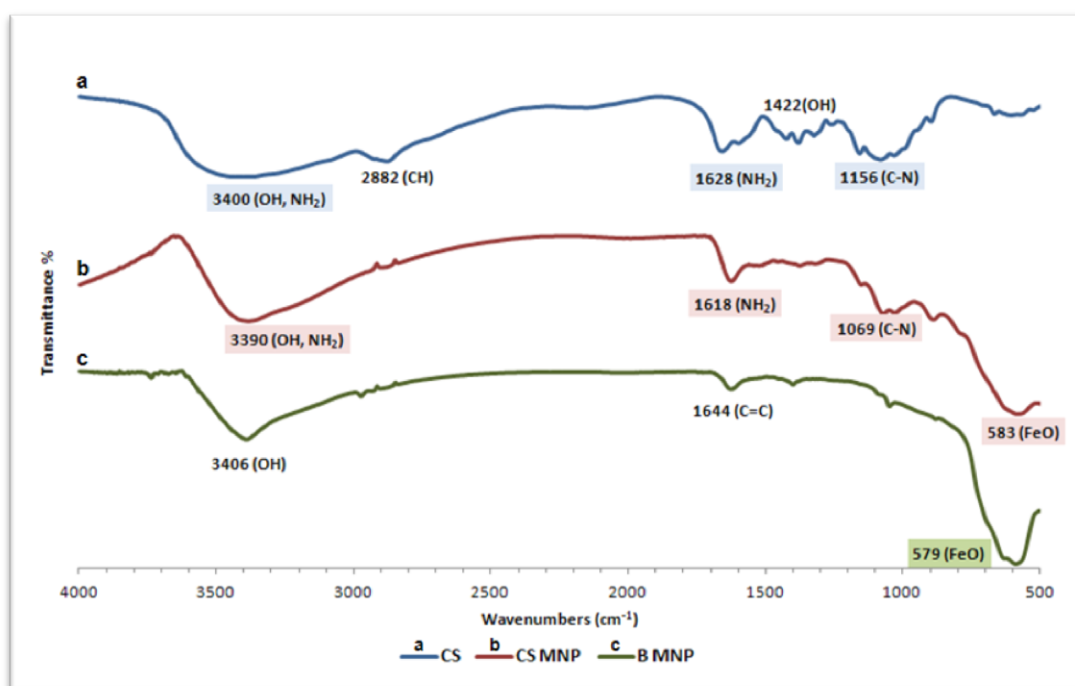


Figure 3.4. FTIR spectra of the chitosan and synthesized magnetic nanoparticles, (a) Chitosan, (b) Chitosan magnetic nanoparticles, and (c) bare magnetic nanoparticles.

3.1.4. Transmission Electron Microscopy (TEM)

Size and morphology of synthesized MNPs and CS MNPs have been observed by TEM. Obtained images showed that (Figure 3.5 and 29) the synthesized CS MNPs are almost spherical and have more uniform size distribution as compared to bare MNPs. The average diameters are around 18-20 nm (bare MNP), 6-8 nm (CS MNP-S₁), 5-7 nm (CS MNP-S₂), 3-5 nm (CS MNP-S₃) and 1-3 nm (CS MNP-S₄). The cumulative particle size distribution histograms of CS MNP-S₁- CS MNP-S₄ were also given (Figure 3.7). The sizes of the nanoparticles get smaller as the concentration of NH₄OH increases in the solution during the synthesis. The monodispersity of size distribution and production of the smallest sized CS MNPs in the literature synthesized by this method are important features of this study. The ammonium concentration seems to be critical to obtain smaller sized nanoparticles.

Though it is difficult to directly observe the layer of CS on the MNPs from TEM images, the dispersing behaviour of surface stabilized MNPs (Figure 3.6) has been improved in comparison with that of bare MNPs (Figure 3.5), which exhibits aggregated morphology. Chitosan is a good agent for stabilizing aqueous suspension of bare MNPs because of its polyelectrolyte property.

The transmission electron microscopy revealed the parallel lattice fringes clearly visible at almost all the nanoparticles. The lattice spacing seen in the lattice fringe of the nanoparticles indicate the crystallinity and structural uniformity of the sample (Ye *et al.*, 2006). The crystalline structures of the bare MNPs and CS MNPs were also characterized by powder X-ray diffraction (XRD) technique. The estimated size of bare MNPs obtained from Debye-Scherrer equation was confirmed by the TEM images.

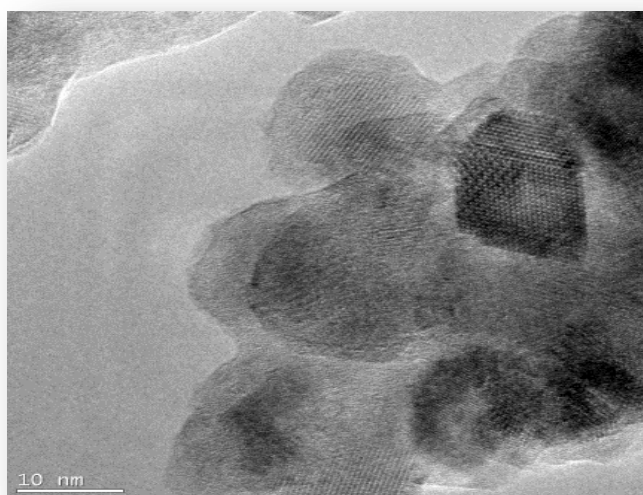
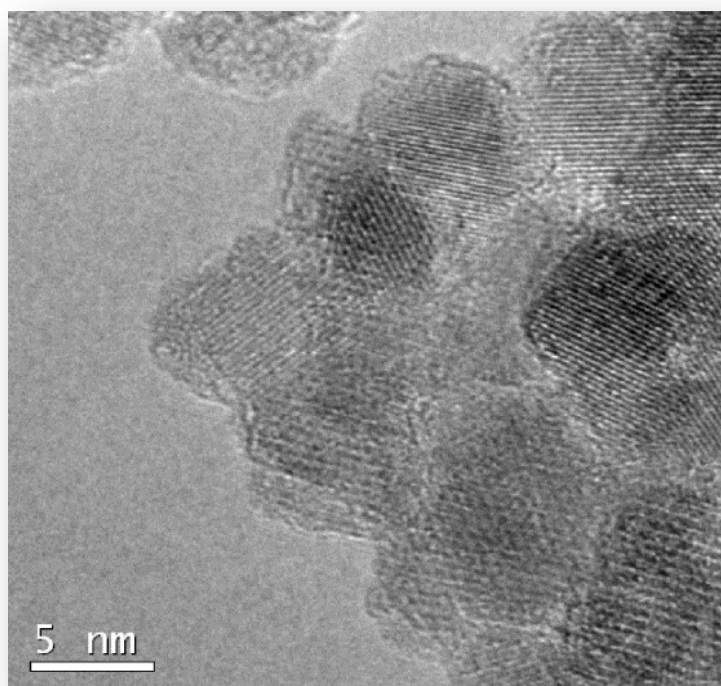
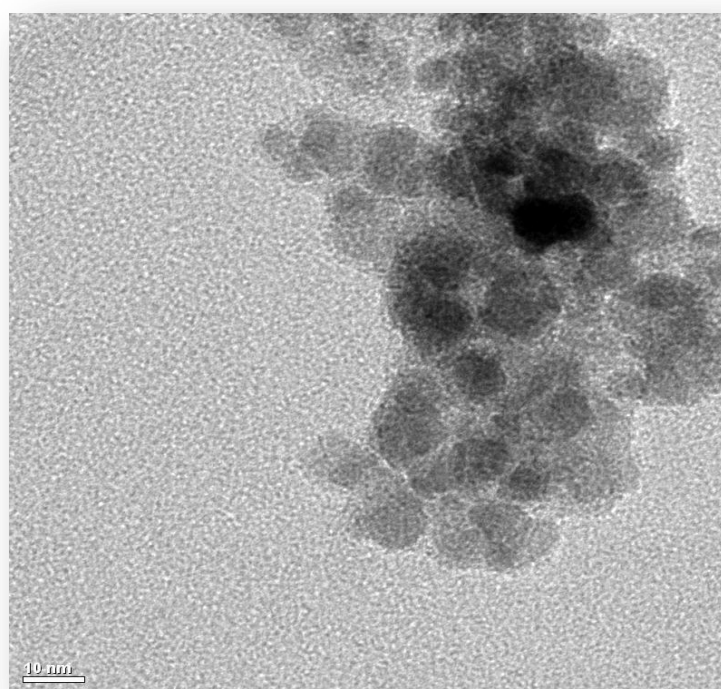


Figure 3.5. TEM images of synthesized bare magnetic nanoparticles.

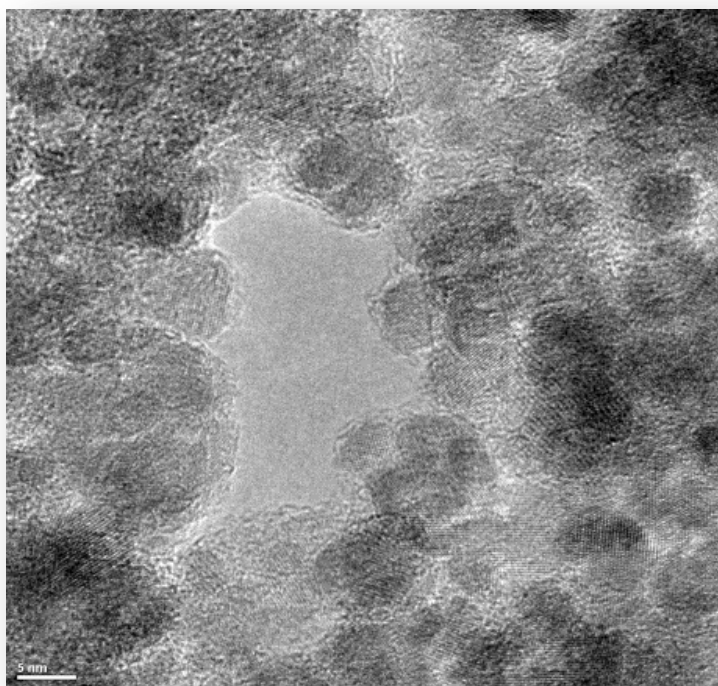


(a) CS MNP-S₁

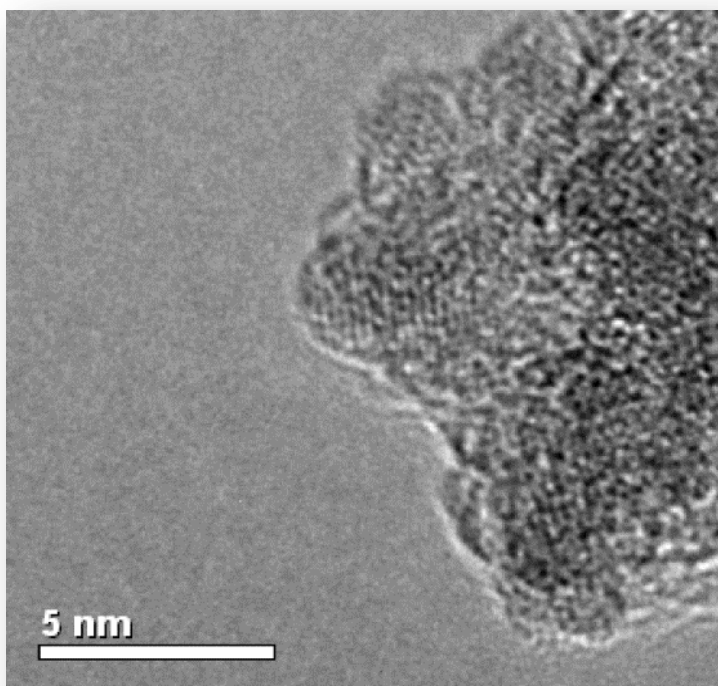


(b) CS MNP-S₂

Figure 3.6. TEM images of synthesized chitosan magnetic nanoparticles (a) CS MNP-S₁, and (b) CS MNP-S₂.



(c) CS MNP-S₃



(d) CS MNP-S₄

Figure 3.6. TEM images of synthesized chitosan magnetic nanoparticles (c) CS MNP-S₃, and (d) CS MNP-S₄.

The core sizes of CS MNPs, dependent on the preparation conditions, were found as 6–8 nm (CS MNP-S₁), 5–7 nm (CS MNP-S₂), 3–5 nm (CS MNP-S₃), and 1–3 nm (CS MNP-S₄) in TEM analyses (Figure 3.7).

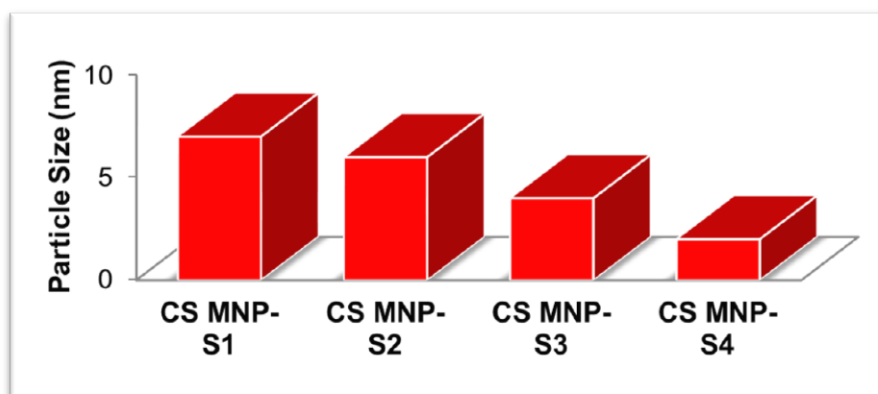


Figure 3.7. Particle size distribution of synthesized CS MNPs according to TEM images.

3.1.5. Freeze Drying of CS MNPs

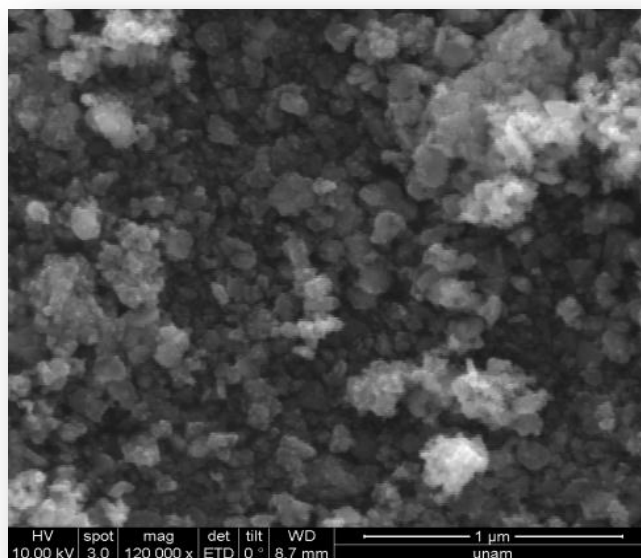
The freeze drying was resulted with an increase on the porosity of CS MNPs and this sponge like structure probably would absorb more drug in loading studies. This method would be used if the drug loading on CS MNPs were inefficient to increase the absorption capacities of nanocarriers.

Because the drug loading studies were found efficient on synthesized CS MNPs, freeze drying process was not necessary and not applied.

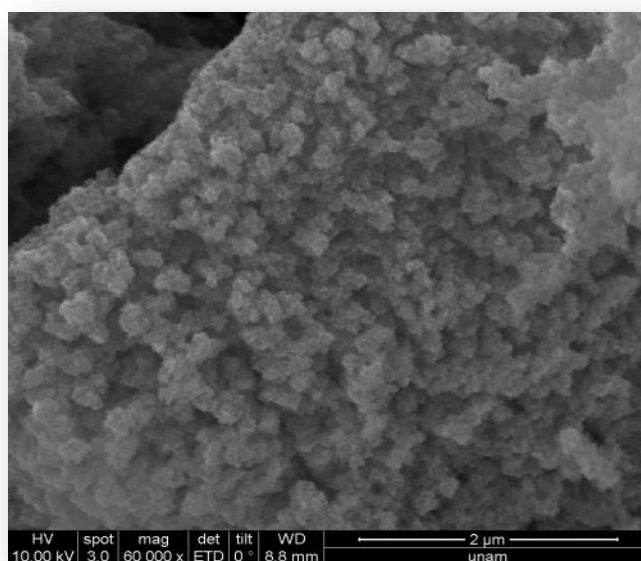
3.1.6. Scanning Electron Microscopy (SEM)

SEM images of the synthesized bare and chitosan coated Fe₃O₄ nanoparticles were given in Figure 3.8. Images of bare MNPs show that the size dispersion of Fe₃O₄ is polydisperse (Figure 3.8 a). In contrast, chitosan MNPs (CS MNP-S₁) have a monodisperse size dispersion and their size is smaller than the bare MNPs (Figure 3.8b and c).

When we freeze dried the chitosan MNPs, they gained a porous structure as compared to non freeze dried chitosan MNPs. The freeze dried chitosan MNPs were dilated and their sizes increased (Figure 3.8d).

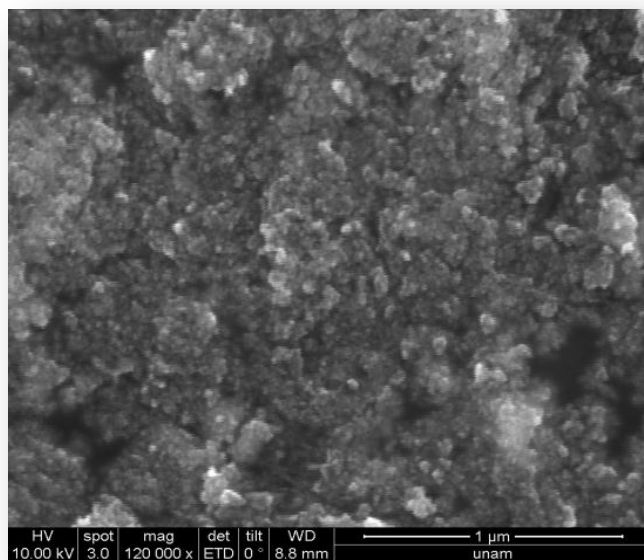


(a) Bare MNPs

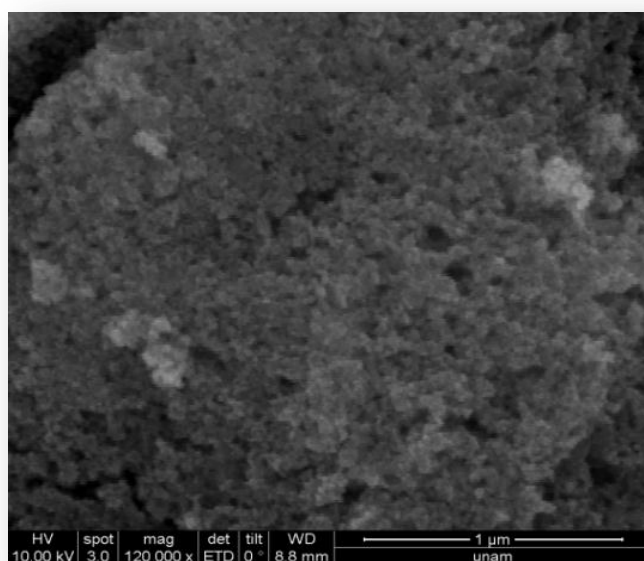


(b) CS MNPs

Figure 3.8. SEM images of synthesized bare MNPs (a) chitosan MNPs (b, c), and freeze dried chitosan MNPs (d) (continued).



(c) CS MNPs



(d) Freeze dried CS MNPs

Figure 3.8. SEM images of synthesized bare MNPs (a) chitosan MNPs (b, c), and freeze dried chitosan MNPs (d) (continued).

3.1.7. Dynamic Light Scattering (DLS)

DLS measures the hydrodynamic size of nanoparticles suspended within a dispersion medium. The average sizes of chitosan MNPs were found as 103 nm CSMNP-S₁, 86 nm CSMNP-S₂, 66 nm CSMNP-S₃, and 58 nm CS MNP-S₄ in DLS measurements (Figure 3.9 and 3.10). This steady increase of the nanoparticle sizes is in parallel with the TEM results.

DLS method differs from TEM in that it measured the hydrodynamic particle size in the dispersion medium. TEM images show the core particle size, without the contribution of the chitosan; because the chitosan layer normally collapses onto the MNPs surface when the dispersion medium is evaporated prior to imaging. It is also obvious that the thickness of the stabilizing layer, when collapsed on the surface of the MNPs, is negligible. Therefore, the difference in diameter measurements obtained by DLS and those obtained by TEM is the size of the chitosan layer. However, this is only valid for small particles (diameter ≤ 200 nm) (Bhattarai *et al.*, 2008).

Since there was no polymer coating on the surface of MNPs, which will increase the hydrodynamic diameter of the nanoparticle, the average sizes of bare MNPs found by XRD and TEM analyses were also confirmed by DLS measurements (Figure 3.11) as 18 nm.

For bare nanoparticle synthesis the yield is high in precipitation method. However, synthesized particles usually have broad size distribution (Gupta&Gupta, 2005). In this method, during synthesis pH is important and has an important role on particle size and morphology (McBain *et al.*, 2008). Thus, the coating with a polymer after the synthesis of bare nanoparticles with precipitation method is not preferred due to the diverse size distribution of core particles. In this study, in situ synthesis of chitosan coated iron oxide nanoparticles method was preferred (Unsoy *et al.*, 2012) due to the size tunable synthesis and homogenous size distribution properties as an easy made process rather than the others.

The ionic interactions occur between the negatively charged (PO^{-1}) groups of the crosslinker and the positively charged (NH_3^{+1}) groups of chitosan molecules dissolved in aqueous acetic acid. This process leads to the formation of a densely packed structure yielding smaller sized nanoparticles as explained by Hritcu *et al.* (2009). Besides, $-\text{NH}_3^{+1}$ groups of chitosan are attracted by $-\text{OH}^{-1}$ of iron oxide, through this way nuclear growth of iron oxide is inhibited by chitosan molecules which provides smaller core size. Another important factor is the degree of deacetylation of chitosan. The higher deacetylation degree of chitosan can provide an increased number of free protonable amino groups (Hu *et al.*, 2010). The CS MNPs have many reactive functional groups to load different molecules such as drugs, contrast agents, or targeting ligands for biomedical applications.

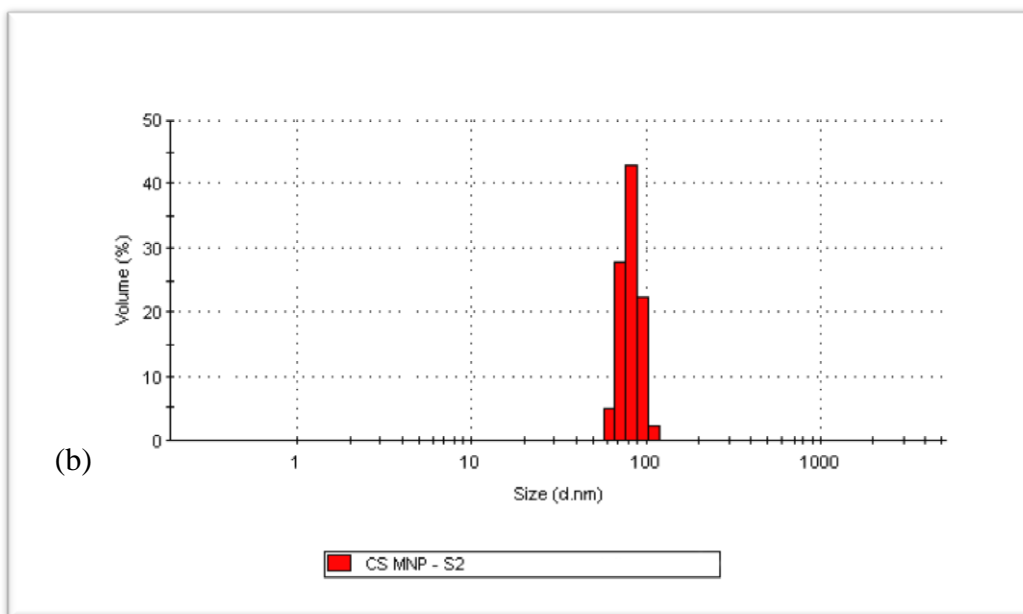
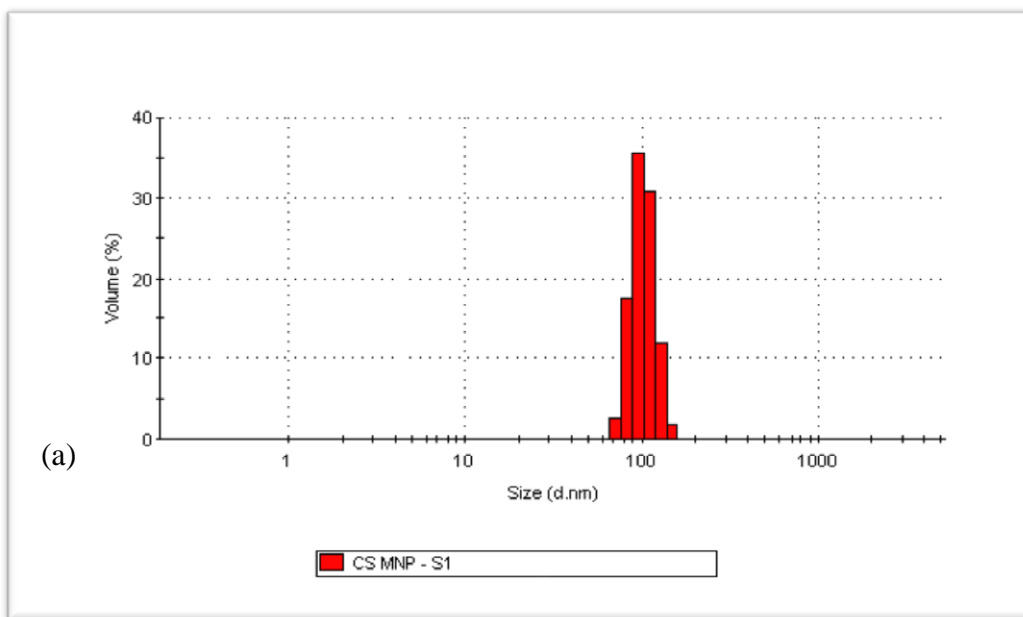


Figure 3.9. DLS diagrams of synthesized chitosan coated MNPs were found as 103 nm CSMNP-S₁ (a), 86 nm CSMNP-S₂ (b), 66 nm CSMNP-S₃ (c), and 58 nm CS MNP-S₄ (d) in DLS measurements (continued).

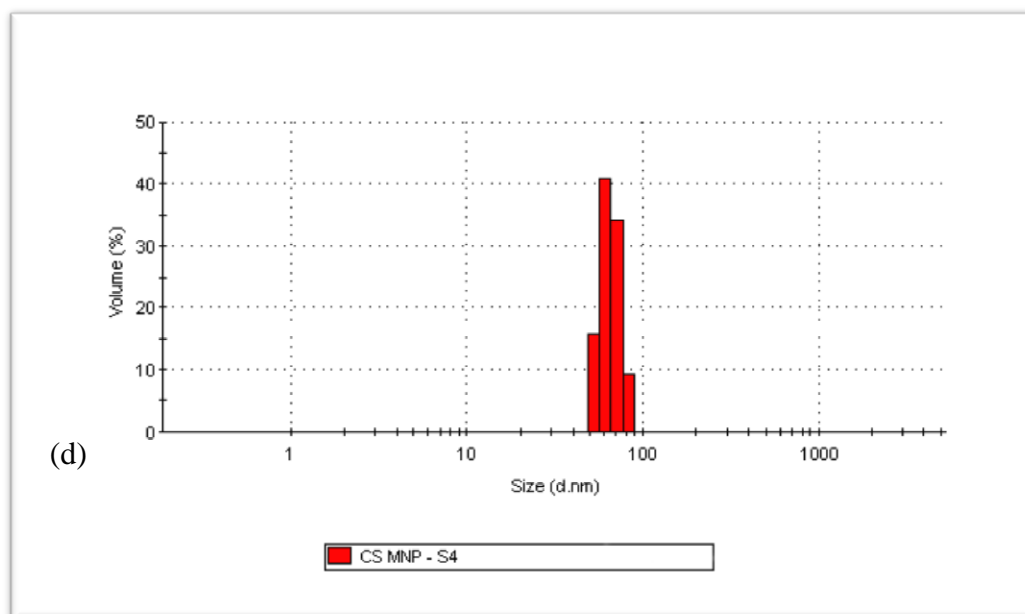
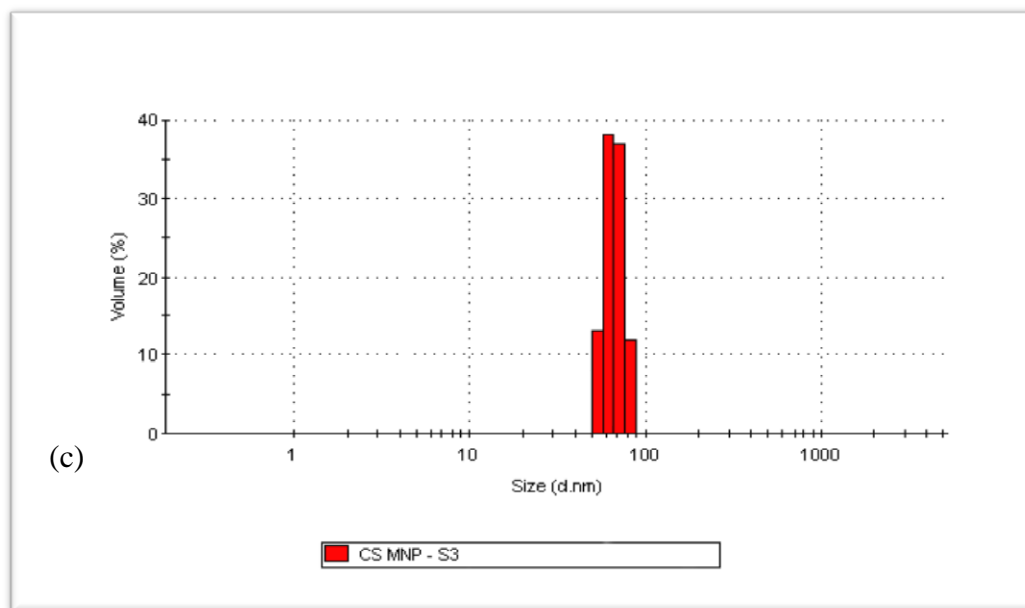


Figure 3.9. DLS diagrams of synthesized chitosan coated MNPs were found as 103 nm CSMNP-S1 (a), 86 nm CSMNP-S2 (b), 66 nm CSMNP-S3 (c), and 58 nm CS MNP-S4 (d) in DLS measurements (continued).

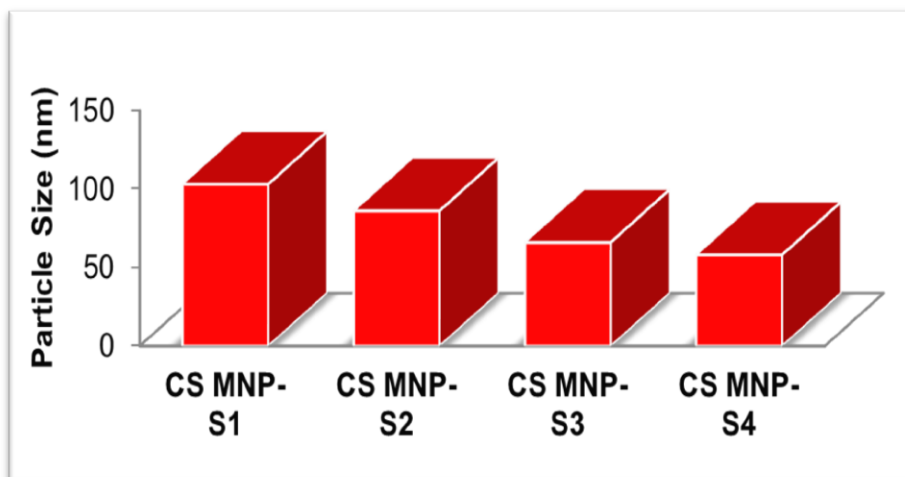


Figure 3.10. Particle size distribution of synthesized CS MNPs according to DLS results.

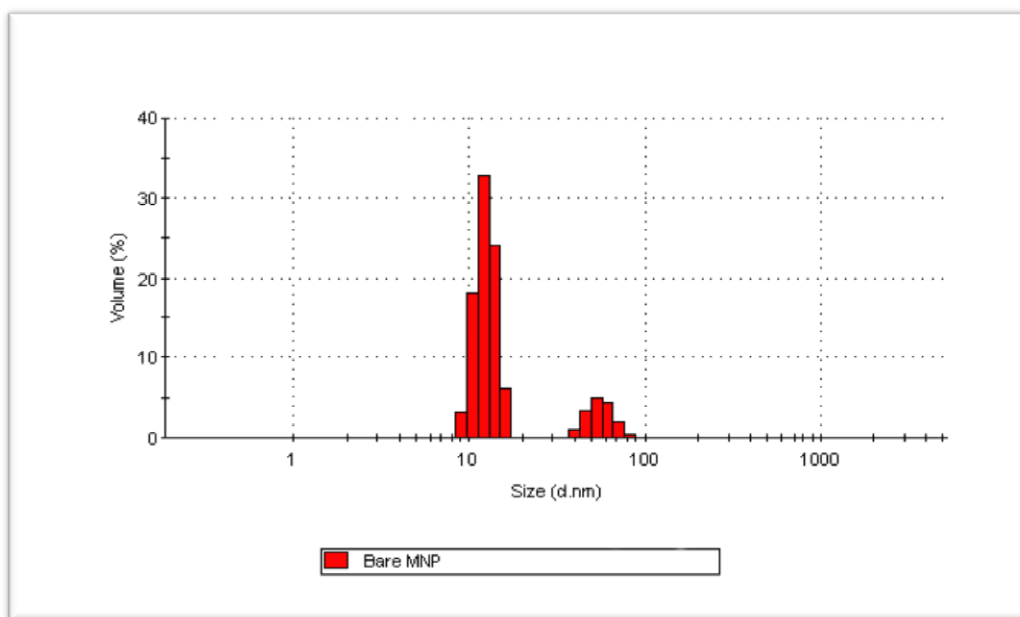


Figure 3.11. DLS diagrams of synthesized bare MNPs shows that the average diameter of particles is 18 nm.

3.1.8. Zeta (ζ) Potential

The zeta potential indicates the degree of repulsion between adjacent, similarly charged particles in dispersion. For particles that are small enough, a high zeta potential will confer stability, i.e., the solution or dispersion will resist aggregation. When the zeta potential is low, attraction exceeds repulsion and the dispersion will break and flocculate. So, colloids with high zeta potential (negative or positive) are electrically stabilized while colloids with low zeta potentials tend to coagulate or flocculate.

The zeta potential values of the bare and chitosan coated MNPs (0.1mg/ml) were measured in 10^{-3} M NaCl aqueous solutions at pH 3.0–11.0 (adjusted by NaOH or HCl). Bare MNPs were negatively charged at basic pH due to the OH⁻ ions on its surface. CS MNPs were positively charged at acidic pH with a surface potential greater than +25 mV at pH < 6 due to the presence of protonated amino groups of chitosan on particle surface (Figure 3.12). The zeta potential decreased from positive to negative with the increase of pH since higher pH facilitates the deprotonation of functional groups.

The isoelectric point (pI), is the pH at which a particular molecule or surface carries no net electrical charge. The pI of bare MNPs was about 5.2. After chitosan coating, the pI was shifted to 6.7 as consistent with the literature (Peng *et al.*, 2004; Yang *et al.*, 2007; Wang *et al.*, 2008). This also confirms the binding of chitosan and reveals that the chitosan coated Fe₃O₄ nanoparticles were positively charged at pH < 6.7.

The pKa value of amino groups in chitosan (pKa from 6.2 to 7.0) leads to protonation of these groups in acidic to neutral solution with a charge density dependent on pH and the acetylation degree. Protonated chitosan is water soluble and bioadhesive to negatively charged surfaces. Chitosan enhances the transport of polar drugs across the cell surfaces.

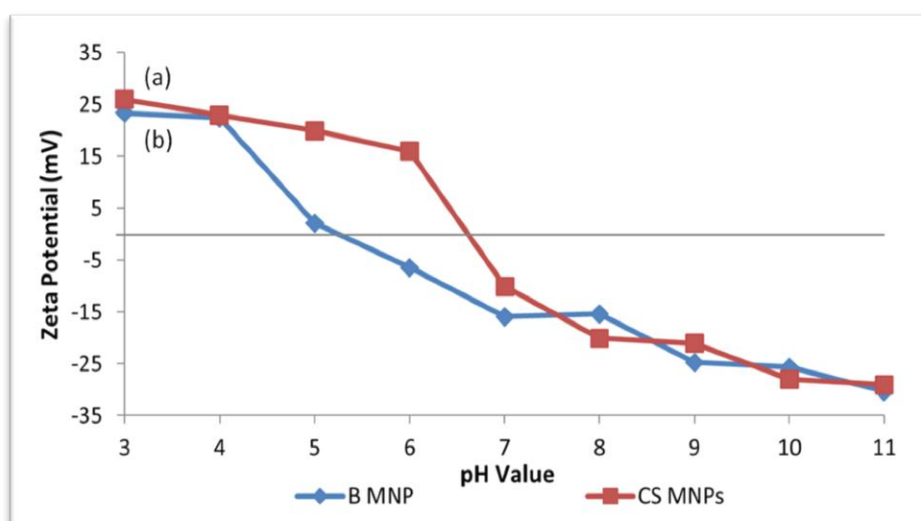


Figure 3.12. Zeta potential measurements of CS MNPs (a) and bare MNPs (b).

3.1.9. Vibrating Sample Magnetometer (VSM)

The magnetization properties of synthesized Bare and CS MNPs were analysed at 37°C, which is the body temperature. The saturated magnetization (M_s) of bare MNPs is 62 emu/g (Figure 3.14 a). The M_s values of CS MNP-S₁ (39 emu/g), CS MNP-S₂ (33 emu/g), CS MNP-S₃ (29 emu/g), CS MNP-S₄ (25 emu/g) were also obtained with VSM analyses. A decrease was observed in the M_s values owing to the decreased core sizes of magnetites incorporated in the chitosan-coating (Figure 3.13).

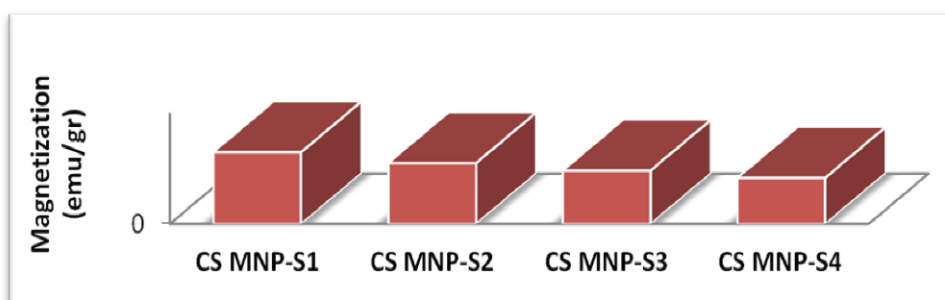


Figure 3.13. Magnetization graph of chitosan coated MNPs (S₁-S₄).

There is no remanance and coercivity was observed (Figure 3.14 b) in the hysteresis loops, demonstrating that the synthesized CS MNPs are superparamagnetic.

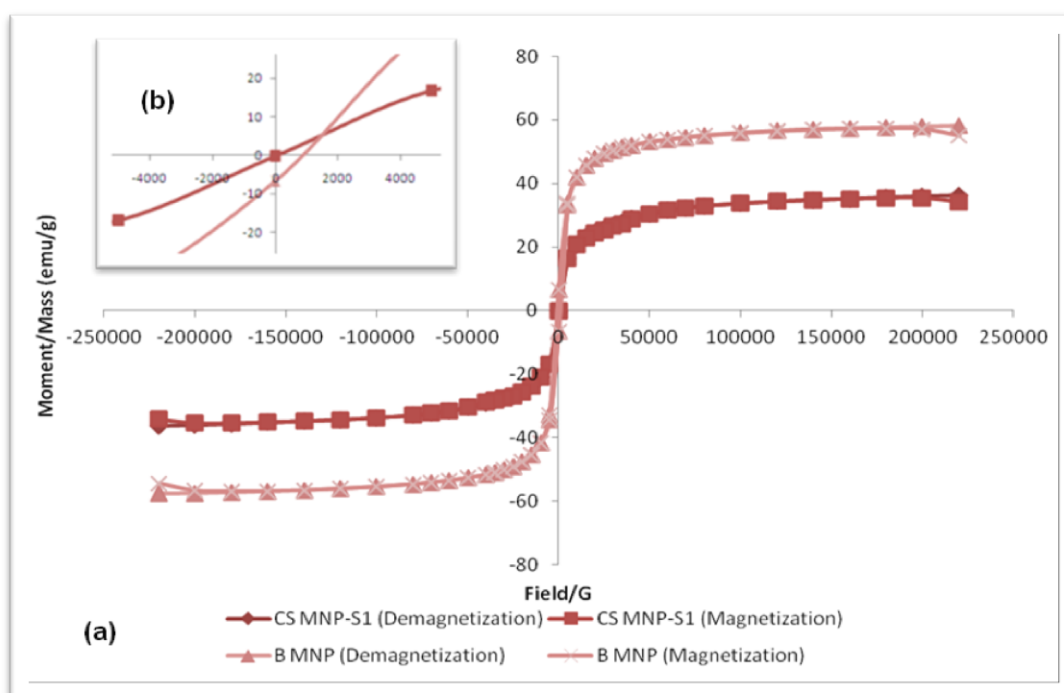


Figure 3.14. The hysteresis curve of bare and chitosan coated MNPs.

Superparamagnetic materials become easily magnetized upon exposure to a magnetic field and unmagnetized once the field is turned off. Besides, their hysteresis curves show similar pattern at different temperatures (Varadan *et al.*, 2008). Magnetic nanoparticles having a core size smaller than 30 nm show superparamagnetic behavior having remanence and coercivity values near to zero (Figure 3.14 b). In this study, magnetization characteristics of the nanoparticles were demonstrated by VSM analyses. No significant remanence and coercivity were observed in the hysteresis loops of bare and chitosan-coated MNPs (Figure 3.14 b). This phenomenon proved that MNPs synthesized in this study are superparamagnetic. In the absence of a magnetic field, superparamagnetic nanoparticles will not show magnetic properties. This is a desired characteristic in biomedical applications. These superparamagnetic magnetite (Fe_3O_4) nanoparticles, stabilized by the biocompatible CS, have many potential applications in biomedicine. Nanoparticles can be efficiently used for imaging, diagnosis, and therapy purposes because they can be easily targeted in magnetic field and have high surface to volume ratio (Yezhelyev *et al.*, 2006; Pison *et al.*, 2006).

3.1.10. Thermogravimetric Analysis (TGA and TGA-FTIR)

The TGA-FTIR analysis of bare and chitosan coated MNPs provide qualitative and quantitative information about the volatile components of the nanoparticles. The TGA curve (Figure 3.15) shows that the weight loss of bare MNPs over the temperature range from 30°C to 850°C is about 3%. This might be due to the loss of residual water in the sample.

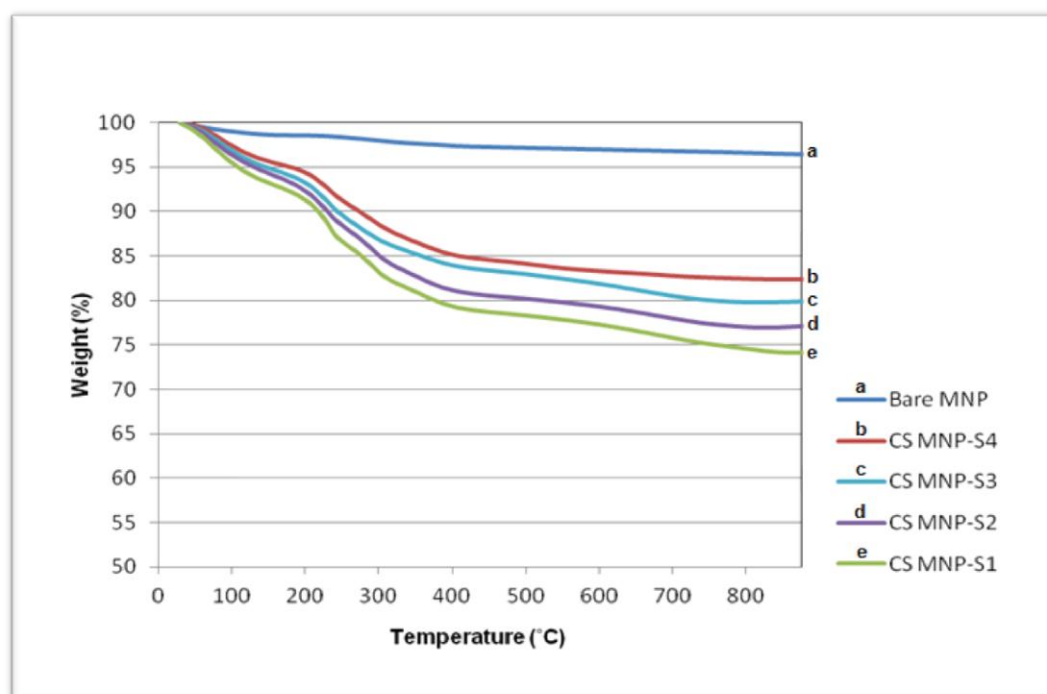


Figure 3.15. Thermal gravimetric analysis curve of bare and chitosan MNPs.

The CS MNPs gave their distinctive TGA curves, which can provide indications of the content of chitosan polymers. The principle chains of CS began to degrade at about 250°C and the final temperature of decomposition was around 700°C.

The results of TGA-FTIR demonstrated that most of the organic layer, chitosan, was removed as CO₂ at high temperatures. The peaks at 2400-2000 cm⁻¹ reflects O=C=O stretching assigned to carbonyl groups of CO₂ (Paama *et al.*, 2003). From the percentage weight loss in the TGA curve, the amount of chitosan bound on MNPs was estimated. The average mass content of chitosan in nanoparticles by TGA was found to be about 23% (CS MNP-S₁), 20% (CS MNP-S₂), 17% (CS MNP-S₃), and 15% (CS MNP-S₄) (Figure 3.15). With the decrease of NH₄OH % in the synthesis, the average diameters of magnetic CS MNPs increased from 58 to 103 nm and the chitosan content increased from 15% to 23%.

3.1.11. Cellular Uptake of Flourescent Modified CS MNPs

The cellular uptake of FITC conjugated CS MNPs were visualized in MCF-7 breast cancer cell lines by confocal microscopy (Figure 3.16). Images show that, the synthesized nanoparticles interact with the surface of cells and internalized. Cellular internalizations of nanoparticles will be displayed in the following drug loading parts in more details (Figure 3.29 and 3.43). The cell viability was not affected by CS MNPs with drug load seven at high concentrations.

Bare MNPs were not taken up as much as CS MNPs by MCF-7 cells due to the negative surface charge (Pan *et al.*, 2007). The Fe₃O₄ nanoparticles elicit a positive surface charge with the chitosan coating. Results of Harush-Frenkel *et al.*, (2007) also show that cellular uptake of positively charged nanoparticles is 3 times higher than that of negatively charged nanoparticles. Uptake of the positively charged nanoparticles reaches a plateau within 45–60 min, indicating saturated binding sites on cells. Permeability of cell membrane depends on the electric charge and polarity of the nanoparticle. Because the cell surface is negatively charged, chitosan coat contribute to the cellular uptake of nanoparticles.

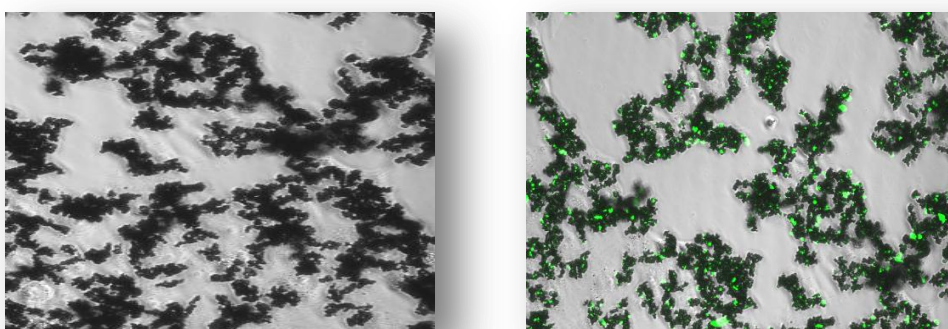


Figure 3.16. Cellular uptake of florescent CS MNP-S₁ by MCF-7 cells.

3.1.12. Cytotoxicity of Bare and CS MNPs

In order to assess the cytotoxicity of synthesized bare and chitosan coated MNPs (CS MNP-S₁), cell proliferation assays were performed with XTT reagent. In most cases there is no over toxicity in concentrations of chitosan nanoparticles up to 1000 µg/mL, although higher concentrations have been occasionally referred not to decrease cell viability as well (Rodrigues *et al.*, 2012) in the literature. When (750 µg/ml) was applied as the highest dose on HeLa, SiHa, MCF-7 and MCF-7/Dox cells, bare and chitosan coated magnetic nanoparticles did not demonstrate a significant toxicity (Figure 3.17, 3.18, 3.19, 3.20).

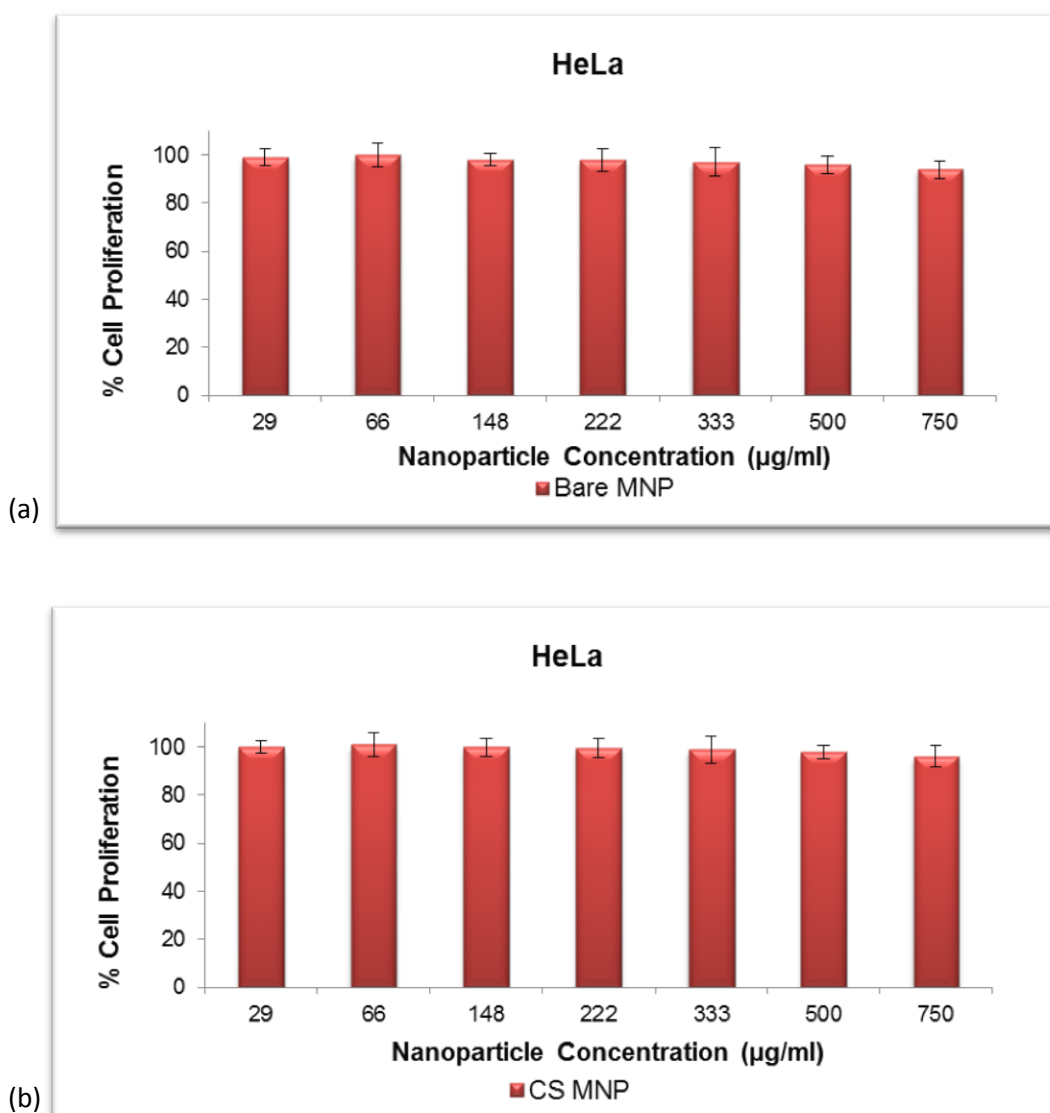
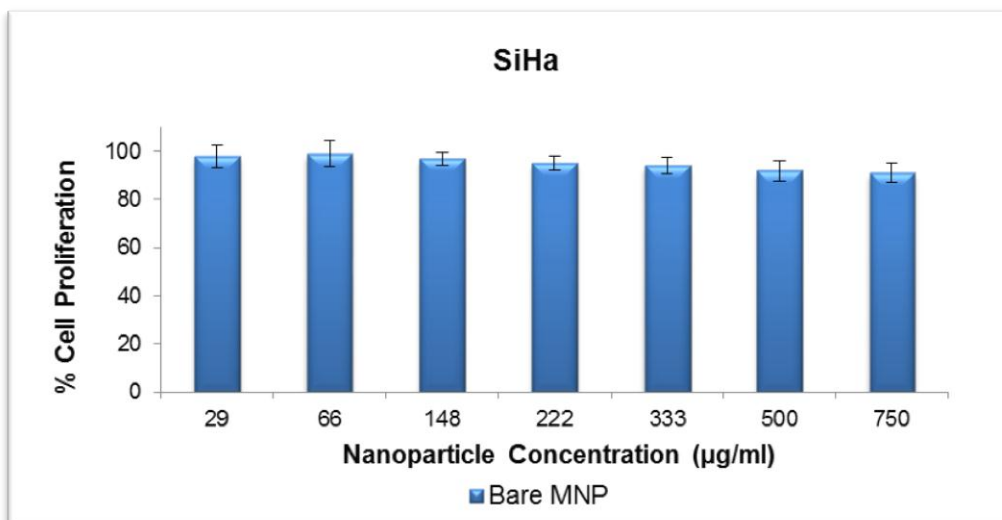
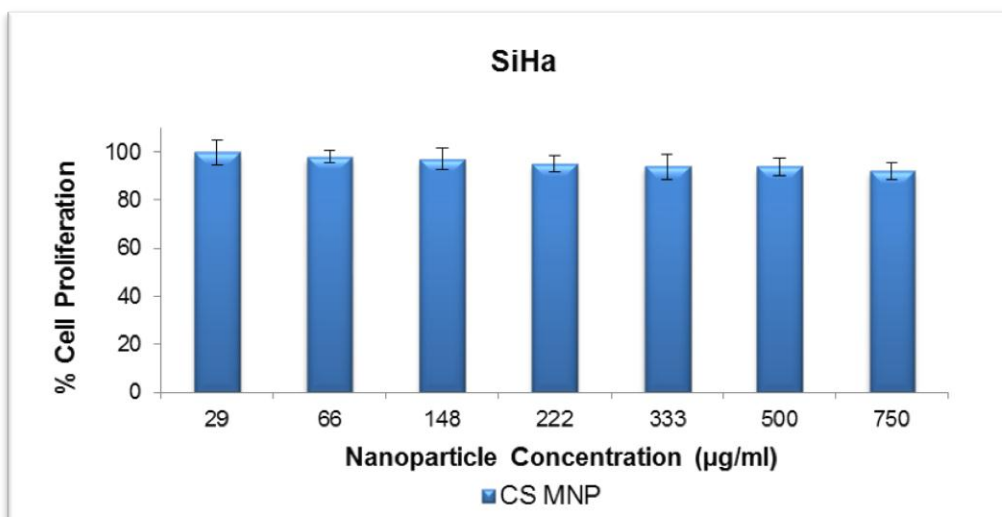


Figure 3.17. Cell proliferation vs MNP concentration graphs of bare (a) and chitosan coated MNP-S₁ (b) on HeLa cells.



(a)



(b)

Figure 3.18. Cell proliferation vs MNP concentration graphs of bare (a) and chitosan coated MNP-S₁ (b) on SiHa cells.

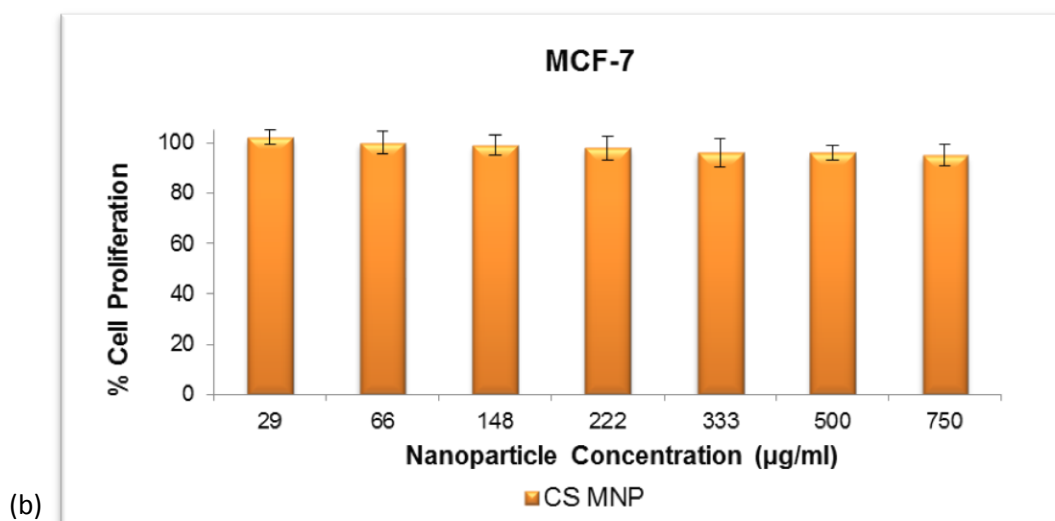
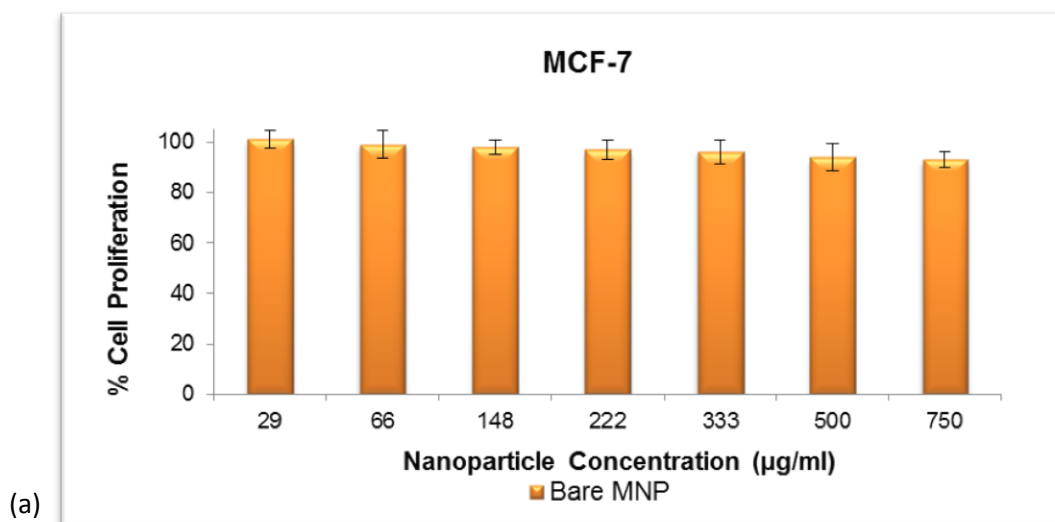


Figure 3.19. Cell proliferation vs MNP concentration graphs of bare (a) and chitosan coated MNP-S₁ (b) on MCF-7 cells.

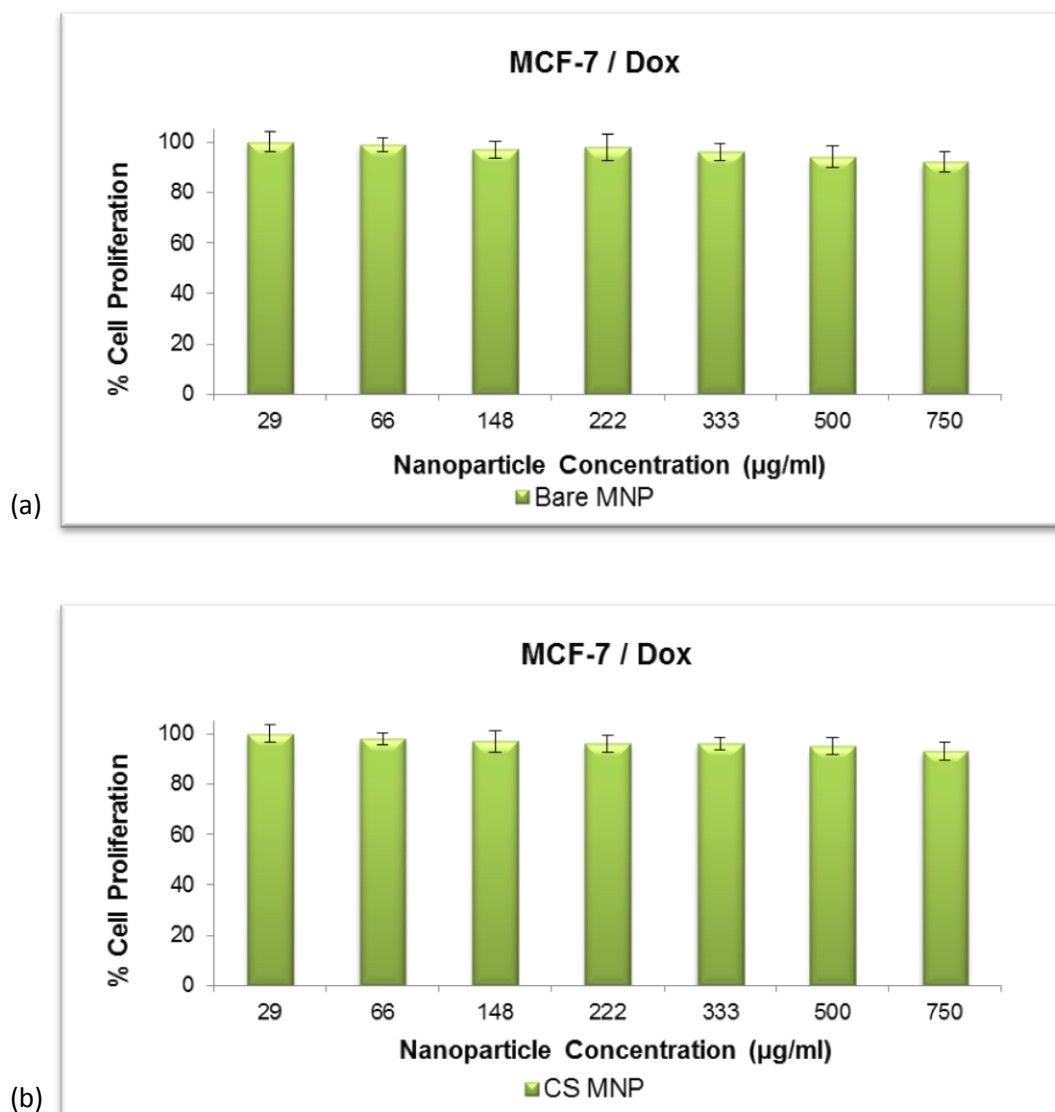


Figure 3.20. Cell proliferation vs MNP concentration graphs of bare (a) and chitosan coated MNP-S₁ (b) on MCF-7/Dox cells.

3.2. Drug Loading, Release, Stability, Cellular Uptake and Cytotoxicity of CS MNPs

The loading of drugs on nanoparticles not only protects the drug but also increases the antiproliferative effect by providing sustained release of drug in the cytoplasm. The stability of drug loaded nanoparticles is an important issue. Due to the efficacy of drug loaded nanoparticles depends on the cellular uptake, intracellular distribution and the released dose of drug from the internalized nanoparticles within the cells; the *in vitro* drug release, cellular uptake and *in vitro* cytotoxicity analyses of nanoparticles were analysed.

3.3.1. Doxorubicin

3.2.1.1. Standard curve of Doxorubicin

Quantification of Doxorubicin amount was performed by generating a standard curve with known amounts of drug concentrations. Standard curve of Doxorubicin was generated with 1/10 dilutions of 180 µg/mL, 240 µg/mL, 300 µg/mL, 400 µg/mL, and 500 µg/mL Doxorubicin concentrations (Figure 3.21).

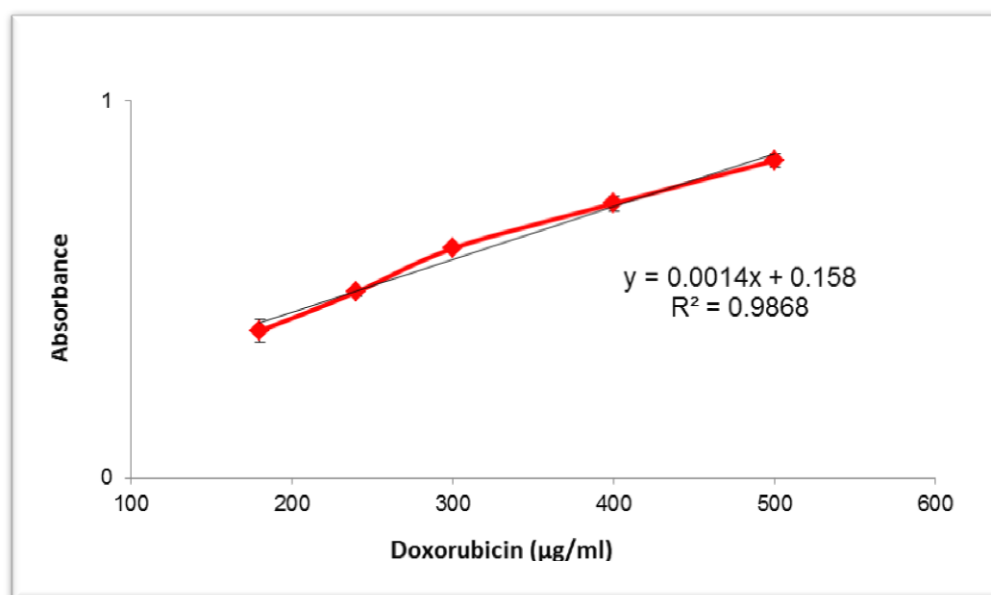


Figure 3.21. Standard curve of Doxorubicin.

3.2.1.2. Doxorubicin Loading on CS MNPs

The water soluble anticancer drug Doxorubicin is one of the most popular anticancer drugs commonly used in acute leukaemia, lymphomas, soft-tissue and osteogenic sarcomas, paediatric malignancies and adult solid tumors, in particular breast and lung carcinomas (Wood *et al.*, 2002). Doxorubicin is a strong cytotoxic compound to normal tissues and produces extensive biochemical adverse effects on the physiology of the patient. The drug is subsequently metabolised in the liver, and about 40% of the drug and its metabolites are excreted (Souhami *et al.*, 2005). Hence, only a small amount of drug actually reaches and acts on the tumor target site. Doxorubicin induced cardiac toxicity has also been well documented by several groups (Sorensen *et al.*, 2003; Kremer *et al.*, 2004; Lipshultz *et al.*, 2006; Longhi *et al.*, 2007). To decrease the toxicity of Doxorubicin, targeted delivery of the drug through polymeric magnetic nanoparticles is an efficient alternative for cancer therapy (Tan *et al.*, 2009).

Doxorubicin loading studies were initially performed on CS MNP-S₁ with different drug concentrations in potassium phosphate buffer (pH 6.0). In order to determine the highest loading efficiency, Doxorubicin concentration gradually increased up to 600 µg/ml where the saturation was obtained (Figure 3.22).

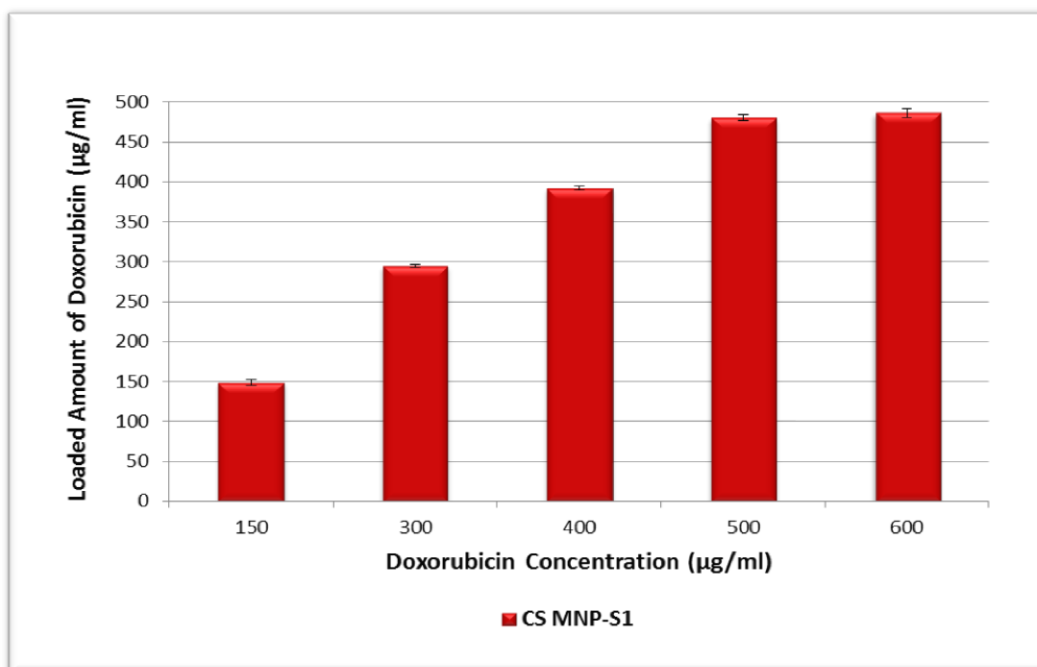


Figure 3.22. Loaded amounts of Doxorubicin on CS MNP-S₁ nanoparticles.

The loading efficiencies of 150 µg/ml, 300 µg/ml, 400 µg/ml, 500 µg/ml and 600 µg/ml Doxorubicin on CS MNP-S₁ were 99%, 98%, 98%, 96% and 81%, respectively. The most efficient and highest loaded amount of Doxorubicin was achieved as 481 µg/ml with 96% loading efficiency (Table 3.1).

Table 3.1. Loading efficiencies and loaded amounts of Doxorubicin on CS MNP-S₁ at different concentrations (150–600 µg/ml).

Loading efficiencies and loaded amounts of Doxorubicin on CS MNP-S ₁					
Doxorubicin Concentration (µg/ml)	150	300	400	500	600
Doxorubicin Loading Efficiency (%)	99.42	98.19	98.08	96.14	81.03
Loaded Amount of Doxorubicin (µg/ml)	149	295	392*	481*	486

* When the loaded amount of Doxorubicin was compared to the initial loading amount of drug, the highest loading amount was obtained with 400 and 500 µg/ml of Doxorubicin concentrations. Following studies will continue with these concentrations.

Doxorubicin loading efficiencies of CS MNP-S₁, S₂, S₃, S₄ were analyzed with the highest loaded concentrations (400 μg/ml and 500 μg/ml) of drug. The loading efficiencies on nanoparticles at 400 μg/ml were about 98% for S₁, 97% for S₂, 95% for S₃ and 93% for S₄, and at 500 μg/ml; 97% for S₁, 95% for S₂, 93% for S₃ and 92% for S₄ (Figure 3.23).

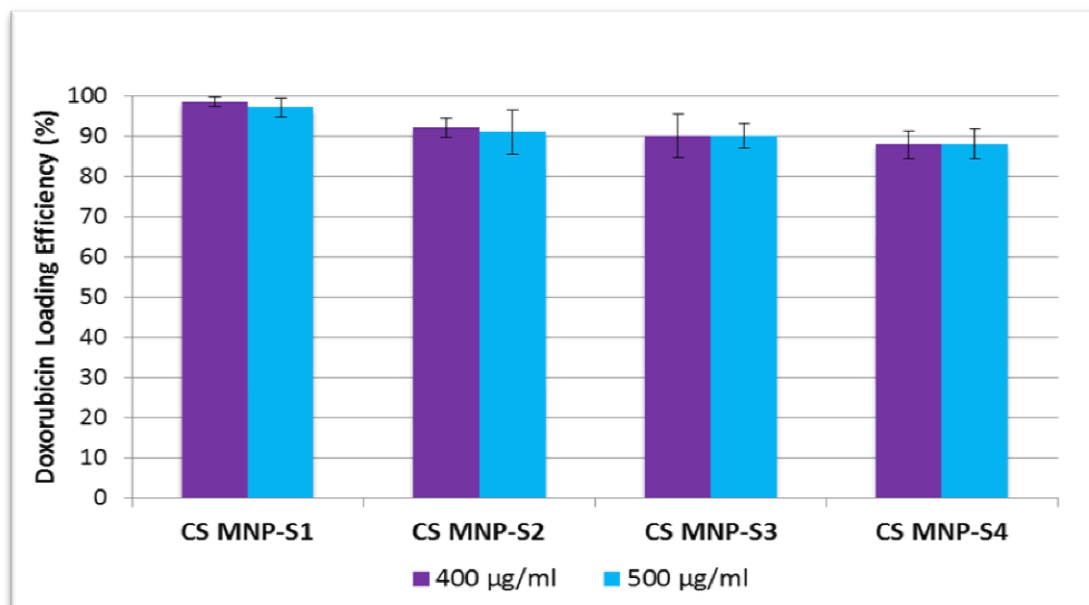


Figure 3.23. Doxorubicin loading efficiencies of CS MNP-S₁, S₂, S₃ and S₄.

The highest Doxorubicin loading efficiency was obtained in CS MNP-S₁, which has the largest particle size (103 nm) and contains the highest amount of chitosan (23%). This may be due to the fact that Doxorubicin is loaded into the chitosan network. Chitosan is known to exhibit pH dependent swelling and controlled drug release properties (Bergeret *et al.*, 2004). In this study, the swelling of unloaded CS MNPs was more than the loaded ones. The drug diffuses into the nanoparticles and forms more cross linking sites in the chitosan structure which leads to lower swelling of the nanoparticles as explained by (Shu *et al.*, 2002).

3.2.1.3. FTIR Analyses of Doxorubicin Loaded CS MNPs

The FTIR analyses were performed in order to support the information of Doxorubicin loading on CS MNPs. The FTIR spectrum for Doxorubicin shows multiple peaks at 2932 (C-H), 1730 (C O), 1618 and 1577 (N-H), 1414 (C-C) and 1071 (C-O) cm⁻¹. These peaks are also present in the FTIR spectrum of Doxorubicin loaded CS MNPs as shifted to 2920 (C-H), 1717 (C O), 1614 and 1574 (N-H), 1406 (C-C) and 1030 (C-O) cm⁻¹, respectively (Figure 3.24). According to these results; Doxorubicin was successfully loaded onto the CS MNPs.

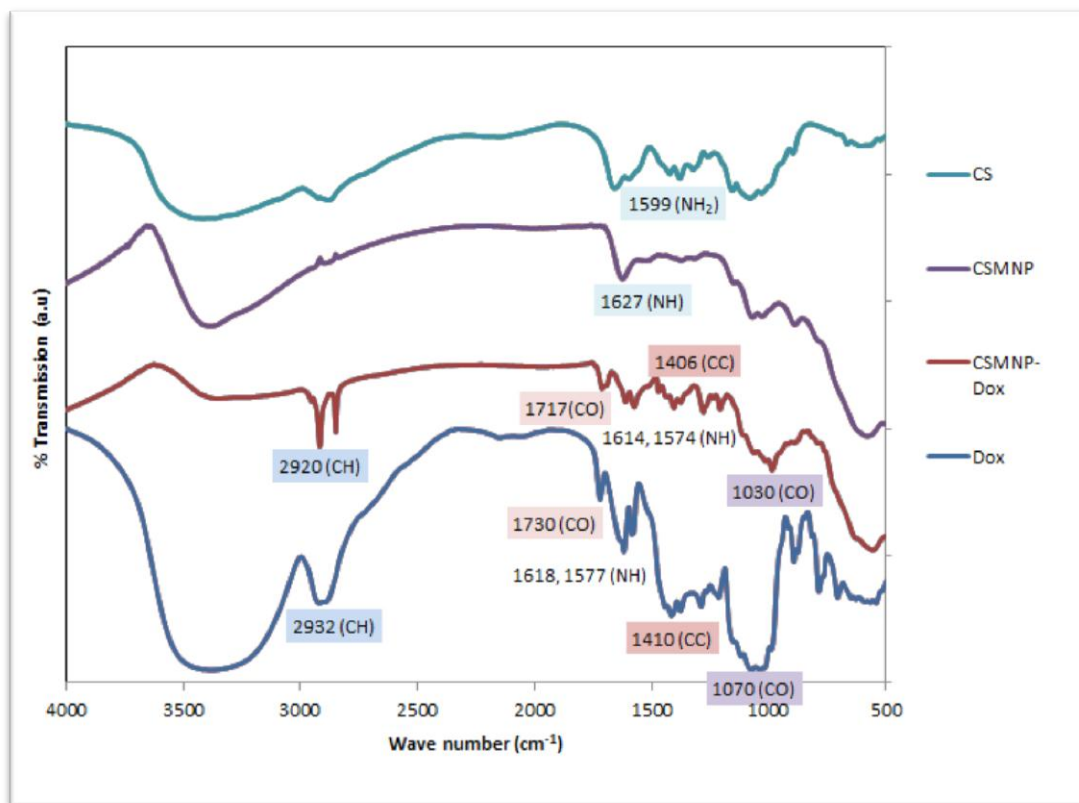


Figure 3.24. FTIR spectra of CS (a), CS MNP-S₁ (b), Doxorubicin loaded CS MNP-S₁ (c) and Doxorubicin (d).

3.2.1.4. Stability of Doxorubicin loaded CS MNPs

The stability of Doxorubicin loaded nanoparticles was evaluated up to 8 weeks in phosphate buffer (pH 7.4) at 37°C, which mimics the physiological conditions (Figure 3.25). Results show that the 500-400 µg/ml Doxorubicin loaded CS MNPs were around 80-85% stable for 10 days. The stability of Doxorubicin loaded CS MNPs did not change much with time, and they are quite stable at 37°C, pH 7.4.

In this study, it was observed that the swelling of Doxorubicin loaded CS MNPs were less than the unloaded ones. The drug diffuses into the nanoparticles and forms more crosslinking sites in the chitosan structure which leads to lower swelling and higher stability of the nanoparticles as also notified by Shu *et al.* (2002).

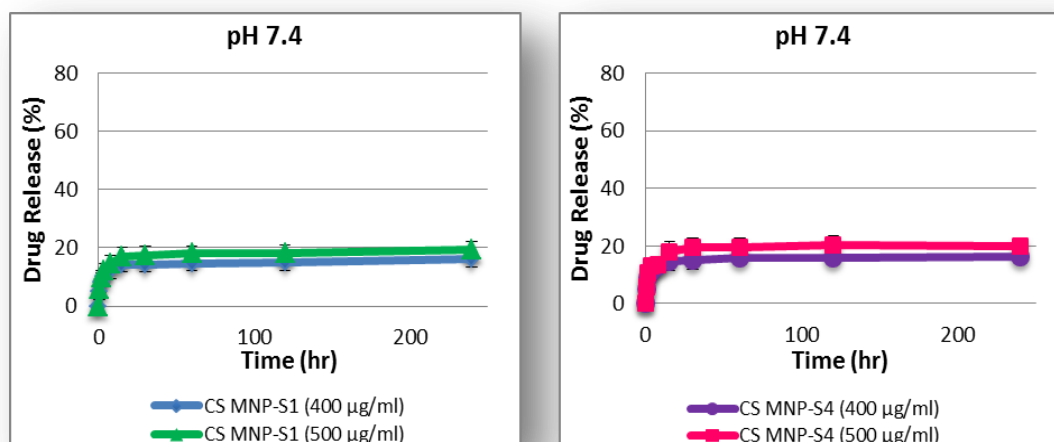


Figure 3.25. Stability of Doxorubicin (400 - 500 µg/ml) loaded CS MNP-S₁ and CS MNP-S₄ in phosphate buffer (pH=7.4).

3.2.1.5. Doxorubicin Release From CS MNPs

Drug release mechanisms of nanoparticles has been well described in the literature as i) desorption, ii) diffusion, and iii) matrix degradation (Aydın *et al.*, 2012, Gonçalves *et al.*, 2010). Doxorubicin release profiles of CS MNPs were obtained by changing different parameters such as buffer type, pH and size of the nanoparticles. CS MNP-S₁ and S₄ were selected for drug release studies due to the size differences. Release was investigated at 37°C, pH 4.2 and 5.0, which mimic endosome conditions. Doxorubicin is stable even in solutions at pH 3.0. Chitosan is known to exhibit pH-dependent swelling and controlled drug release properties (Berger *et al.*, 2004).

In vitro drug release study of CS MNPs demonstrated an initial burst release of Doxorubicin followed by a sustained release. This initial rapid release, characterized as “burst effect”, occurs by desorption of Doxorubicin, localized on the surface of nanoparticles. The burst release was detected in the first 4 hours as the range of 48-66% for pH 4.2 and 26-40% for pH 5.0. After this initial burst effect, a slower and controlled release occurred throughout the incubation period (Figure 3.26 and 3.27).

In 400 µg/ml and 500 µg/ml initial Doxorubicin loading concentrations, CS MNP-S₁ nanoparticles released about 52% and 61% of the loaded drug respectively during the first 15 hours at pH 4.2. On the other hand, 64% (400 µg/ml) and 75% (500 µg/ml) of Doxorubicin was released from CS MNP-S₄, under the same conditions (Figure 3.26 and 3.27).

In pH 5.0, drug release rate of CS MNP-S₁ was 30% and 35% at 400 µg/ml and 500 µg/ml loading concentrations of Doxorubicin for 15 hours, respectively. The drug release rate in case of CS MNP-S₄ was 40% and 47% at 400 µg/ml and 500 µg/ml concentrations of Doxorubicin (Figure 3.26 and 3.27).

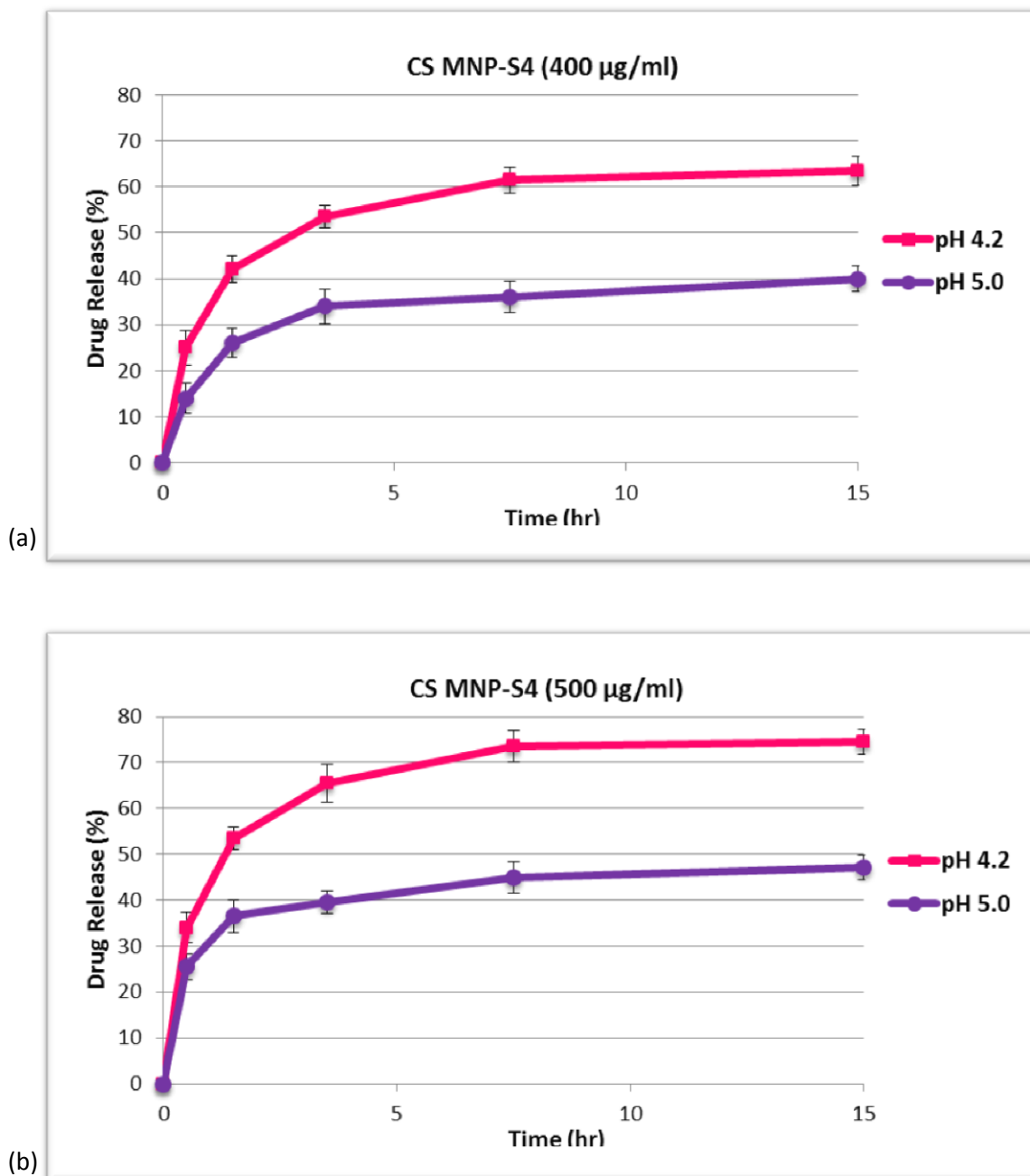


Figure 3.26. Doxorubicin release graph of CS MNP-S₄ nanoparticles at pH 4.2 and 5.0 with (a) 400 and (b) 500 µg/ml initial loading concentrations.

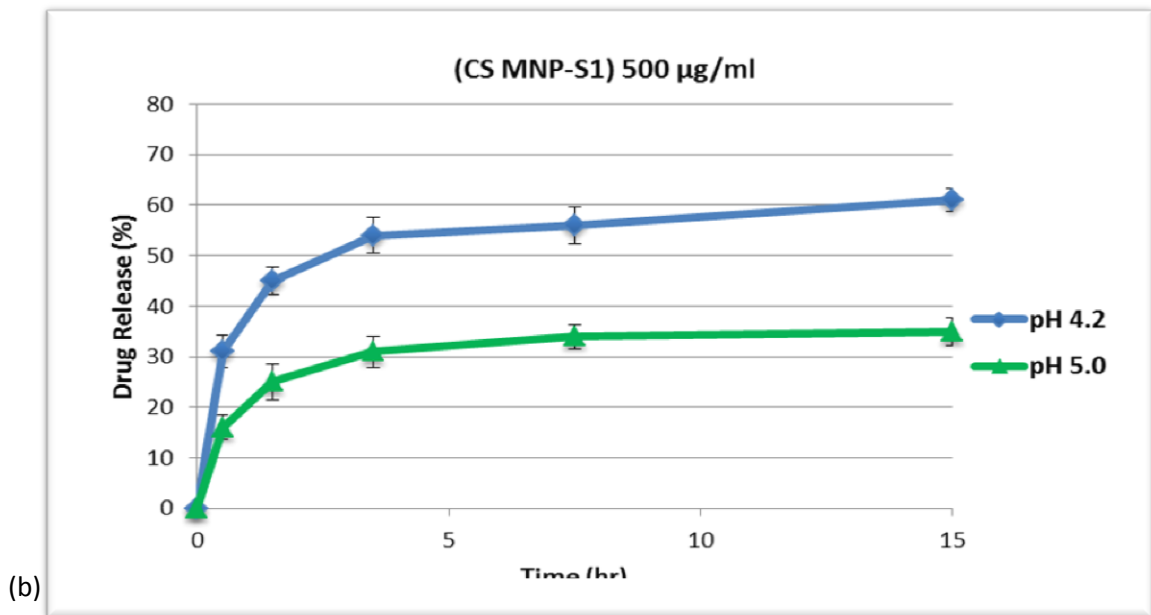
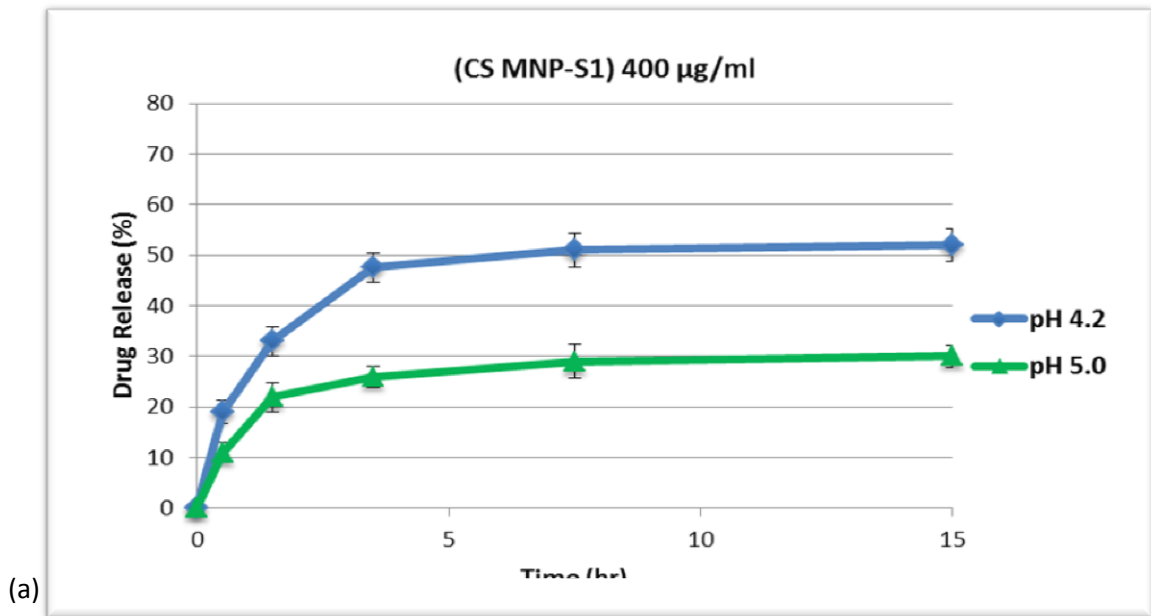


Figure 3.27. Doxorubicin release graph of CS MNP-S₁ nanoparticles at pH 4.2 and 5.0 with (a) 400 and (b) µg/ml initial loading concentrations.

As stated in the study of Sahu *et al.* (2010), pH value of the medium has a remarkable effect on the release rates of Doxorubicin. Drug release rates of CS MNPs are not same at different pH conditions. The drug release rates of CS MNPs increase with the reduced pH value of the medium. This release behavior is based on the degradation of chitosan matrix and higher solubility of Doxorubicin, at acidic pH values. The release of Doxorubicin was higher at pH 4.2 than pH 5.0 for both CS MNP-S₁ and S₄ (Figure 3.26 and 3.27). Since CS MNP-S₁ has more chitosan content and higher Doxorubicin retention capacity, drug release rates of CS MNP-S₄ was higher (~10%) than CS MNP-S₁.

The pH of the tumor microenvironment is low (around 4.0-5.5) due to the high anaerobic glucose metabolism of cancer cells (Estrella *et al.*, 2013; Engin *et al.*, 1995; Ojugo *et al.*, 1999; Van *et al.*, 1999). It is considered that the nanoparticles are taken up by endocytosis into the cells (Decuzzi *et al.*, 2007; Park *et al.*, 2006). This endocytic pathway begins near the physiological pH of 7.4, and then it drops to pH 5.5-6.0 in endosomes and comes around pH 4.5 in lysosomes (Sahu *et al.*, 2010; Mellman *et al.*, 1986). Synthesized drug loaded CS MNPs are stable at physiological conditions (pH 7.4) and expected to have an effective drug release in the tumor microenvironment since the drug release rates accelerate with the decrease in pH (around 4.0-5.0). Therefore, the pH responsive CS MNPs can selectively release their drug load inside the tumor cells at the targeted tissue. According to the drug release profiles of CS MNPs, the loaded Doxorubicin is mostly released within the first 7 hours. Doxorubicin release was higher at pH 4.2 (71%) than at pH 5.0 (45%).

For the successful delivery of Doxorubicin, a balance is required between the stability of CS MNPs at physiological conditions and drug release from CS MNPs at the lower pH conditions on the targeted tumor site (Jansen *et al.*, 1994). The efficient drug release is achieved by the pH sensitive swelling behavior of chitosan (Aydin *et al.*, 2012). The charge density is also important in electrostatic interactions and mainly depends on the solution pH. Swelling of the chitosan and release of the drug is mainly influenced by ionic interactions between chitosan chains; which depend on the crosslinking density set during the formation of the chitosan network (Bergeret *et al.*, 2004). Consequently, pH responsive chitosan drug carriers provide selective drug release at acidic intracellular vesicles such as endosomes and lysosomes in targeted tumor cells (Gillieset *et al.*, 2005).

3.2.1.6. Cellular Uptake of Doxorubicin-loaded Nanoparticles

Cellular uptake of the Doxorubicin loaded CS MNP-S₁ nanoparticles were investigated by fluorescence microscopy on MCF-7 breast cancer cells and 1 μ M Doxorubicin resistant breast cancer cells (MCF-7/Dox); obtained images are given in Figure 3.28 and 3.29

Doxorubicin is a fluorescent drug, having a bright red color and can be visualized under microscopy. In Figure 3.28, the reflected red color inside and around the nucleus indicates that Doxorubicin loaded nanoparticles were internalized by the cells, expressing the efficient cellular uptake of the particles.

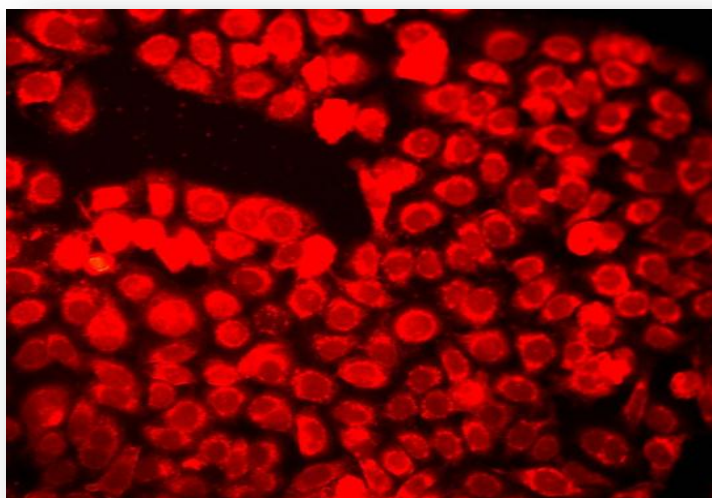


Figure 3.28. Fluorescent microscopy images of MCF-7/S cells treated with Doxorubicin loaded CS MNP-S₁ nanoparticles obtained at red filter.

Doxorubicin loaded CS MNP-S₁ nanoparticles accumulate both in the cytoplasm and the nuclei of MCF-7/Dox cells similar to the MCF-7 cells. Cellular uptake of drug loaded nanoparticles by the cells can be clearly observed by the intensity of fluorescent red color of Doxorubicin in both MCF-7 cell lines (Figure 3.29).

Doxorubicin loaded CS MNPs are successfully internalized by sensitive and Doxorubicin resistant MCF7 cells. When Doxorubicin is loaded into the nanoparticles, it can accumulate in the cells since the nanoparticles can not easily pumped out from the cells. P-glycoprotein (P-gp or MDR1), an ATP-dependent drug efflux pump, is responsible for decreased drug accumulation in multidrug-resistant cells and mediates the development of resistance to anticancer drugs. Doxorubicin accumulation was considerably lower in MCF-7/Dox cells due to the high expression of Pgp pumps on the cell membrane (Dönmezet *al.*, 2011 a). MCF-7 cells, which lack P-gp, collect Doxorubicin specifically in their nuclei, while MCF-7/Dox cells, which overexpress P-gp, accumulated drug in their cytoplasm and most of the Doxorubicin concentrated at the cell periphery (Dönmezet *al.*, 2011 b).

According to Figure 3.29, images demonstrated stronger fluorescence indicating more intracellular uptake and accumulation of Doxorubicin loaded CS MNPs in the MCF-7 cells. However, the fluorescence difference in the cytoplasm and nuclei of MCF-7 and MCF-7/Dox cells is remarkably reduced by the delivery of Doxorubicin via nanoparticles. Even though the observed intensity of fluorescence was higher in MCF-7 cells in comparison to MCF-7/Dox cells (Figure 3.29), Doxorubicin was successfully delivered into the cytoplasm and nuclei of resistant cells. Therefore, elimination of Doxorubicin resistance was achieved by the synthesized Doxorubicin loaded CS MNPs. This increase in intracellular drug accumulation was achieved in the thesis of Dönmez(2010) by *MDR1* silencing with siRNA.

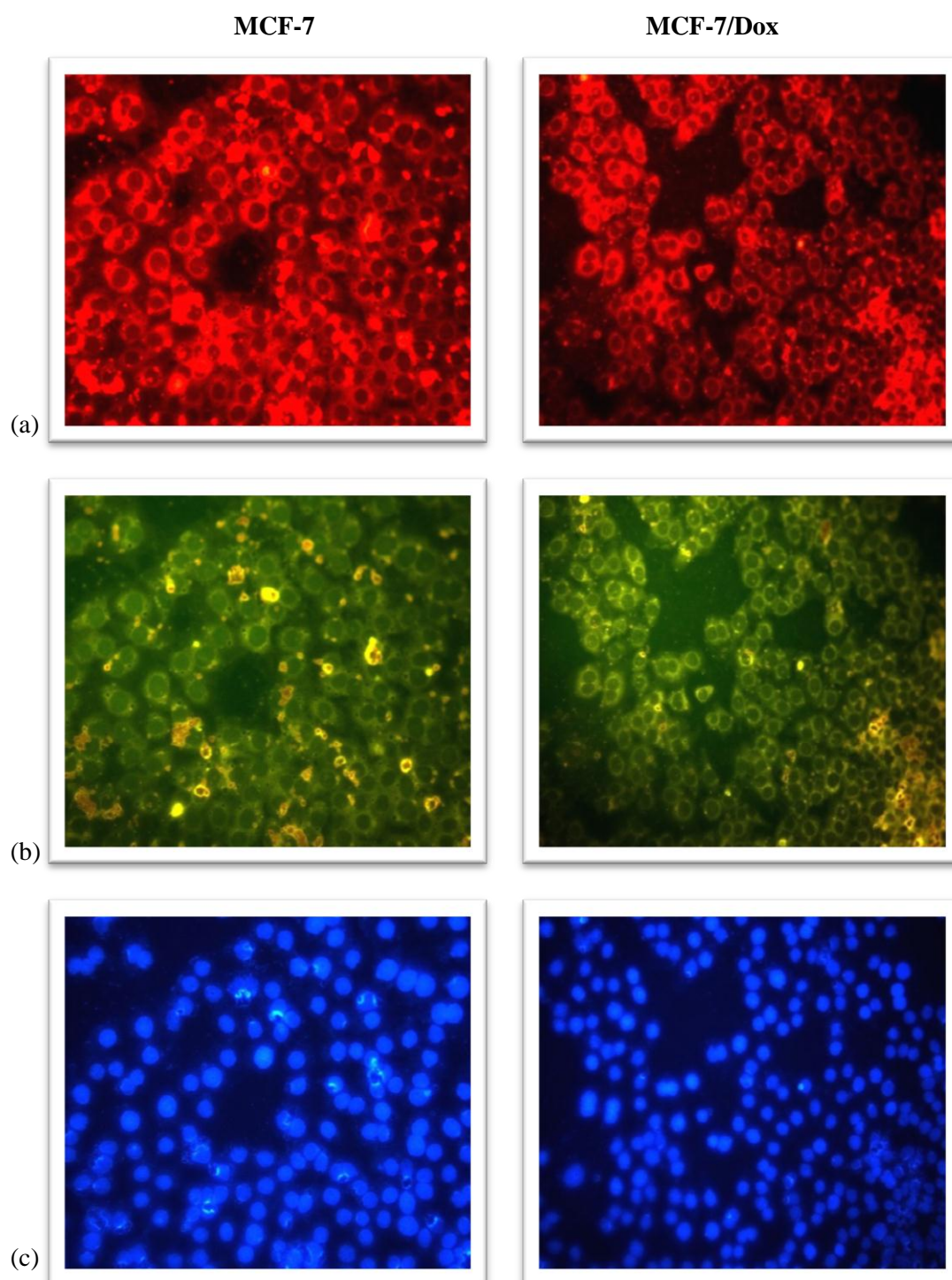


Figure 3.29. Fluorescent microscopy images of MCF-7/S cells and MCF-7/Dox (1 μ M) resistant cells treated with Doxorubicin loaded CS MNP-S₁(a) Doxorubicin loaded nanoparticles are observed inside the cells with red filter, (b) Cells and Doxorubicin loaded nanoparticle agglomerates that are not internalized can be specified under the green filter,(c) Nuclei of the cells are labelled with Dapi staining and visualized with blue filter.

3.2.1.7. Cytotoxicity Analyses of Doxorubicin Loaded CS MNPs

Cytotoxicity of Doxorubicin loaded CS MNP on breast cancer cell lines were determined by cell proliferation assay with XTT reagent. MCF-7 and MCF-7/Dox cells were treated with Doxorubicin loaded CS MNP-S₁ for 48 hours in 96-well plates. After 48 hours of incubation, cell viability profiles and IC₅₀(half maximal inhibitory concentration) values were determined for each particular cell type.

IC₅₀ values for Doxorubicin were calculated from the logarithmic trend line of the cell proliferation percentage versus concentration plots. According to the previous studies carried on our laboratory, 1.8 µM Doxorubicin induced 50% reduction in the cell proliferation of MCF-7 cells. However, in MCF-7/Dox cells, the necessary concentration for 50% inhibition of cell proliferation is 202.5 µM (Dönmez, 2010). This indicates that the resistant MCF-7/Dox cells are approximately 110 times more resistant to Doxorubicin than MCF-7 cells. In order to overcome the resistance by changing the way of Doxorubicin influx, improve the therapeutic efficiency of drug and provide targeting; Doxorubicin was loaded on CS MNPs.

Figure 3.30 and 3.32 demonstrate the antiproliferative effects of Doxorubicin loaded CS MNPs with increasing concentrations on MCF-7 and MCF-7/Dox cells. The graphs show a gradual decrease in cell proliferation with increasing concentrations of Doxorubicin loaded CS MNPs. As demonstrated in Figure 3.30 and 3.32, IC₅₀ values of Doxorubicin loaded nanoparticles was about 1.0 µM and 13.5 µM on MCF-7 and MCF-7/Dox cells, respectively. However, previously it was found as 1.8 µM and 202.5 µM for free Doxorubicin. The IC₅₀ values are decreasing, since the efficacy of Doxorubicin increases when loaded on CS MNPs.

In the studies of Lee *et al.*,(2011), chitosan/Doxorubicin conjugate nanoparticles were synthesized and *in vitro* cytotoxicity of nanoparticles were analyzed on CT-26 colon adenocarcinoma cell lines. IC₅₀ value of the chitosan/Doxorubicin conjugate was found as 1.5 times less than that of free Doxorubicin by MTT assay.

Doxorubicin loaded CS MNPs were highly uptaken by even resistant MCF-7/Dox cells as observed in fluorescent microscopy images of the cellular internalization. According to the XTT results, IC₅₀ values of free Doxorubicin (202.5 µM) decreased to 13.5 µM when Doxorubicin was given as loaded on CS MNPs to the resistant MCF-7/Dox cells (Figure 3.32). Consequently, loading of Doxorubicin onto the nanoparticles not only increased the efficiency of drug but also overcame the resistance to Doxorubicin in MCF-7/Dox cells.

Since both the free Doxorubicin and Doxorubicin loaded CS MNPs were remarkably internalized by MCF-7 cells as also shown in fluorescent microscopy images, the difference between the IC₅₀ values of free Doxorubicin (1.8 µM) and Doxorubicin loaded CS MNPs (1.0 µM) is not drastically high in MCF-7 cells when compared to resistant cells (Figure 3.30).

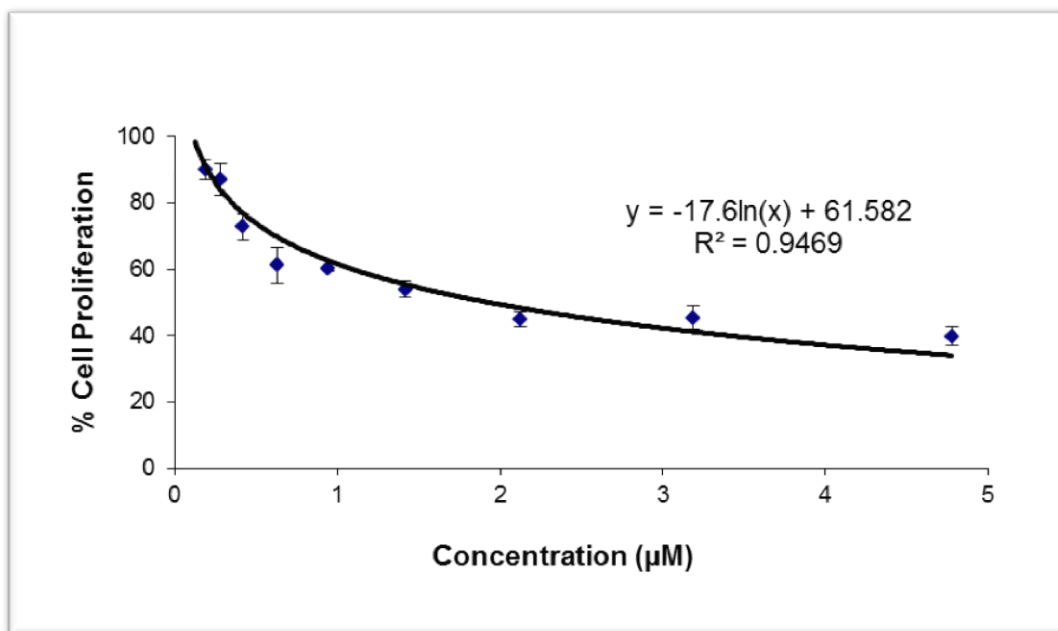


Figure 3.30. Cell proliferation profiles of MCF-7 cells after exposure to increasing concentrations of Doxorubicin loaded CS MNPs ($IC_{50}=1.05\mu M$).

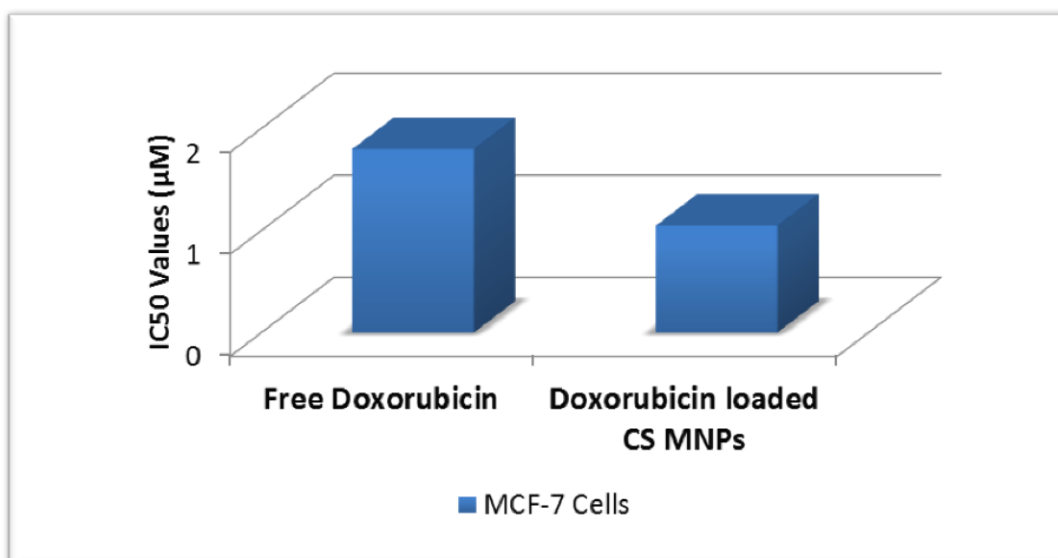


Figure 3.31. The comparison graph of IC_{50} values of free Doxorubicin and Doxorubicin loaded CS MNPs on MCF-7. When Doxorubicin is loaded on CS MNPs, IC_{50} values are decreasing. Since the efficiency of Doxorubicin increases, required amount of the drug 2 times decreases.

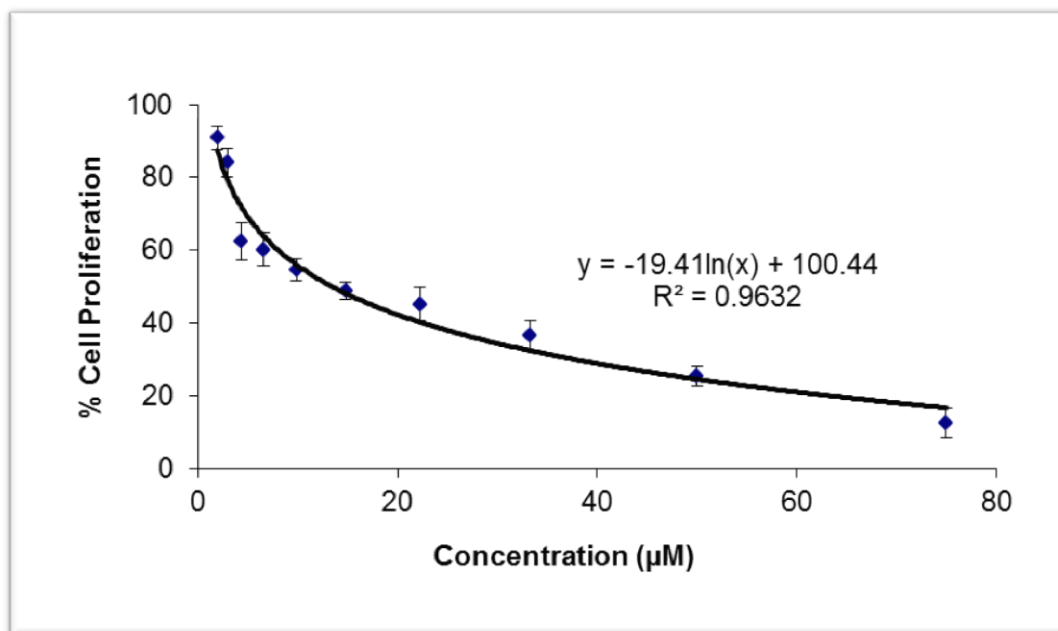


Figure 3.32. Cell proliferation profiles of MCF-7/Dox cells after exposure to increasing concentrations of Doxorubicin loaded CS MNPs ($IC_{50}=13.5\mu M$).

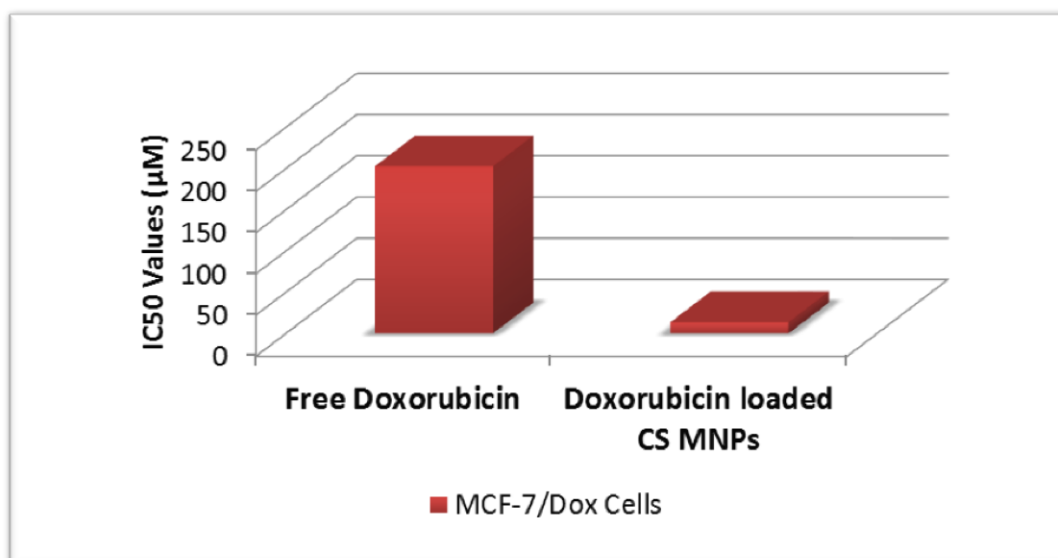


Figure 3.33. The comparison graph of IC_{50} values of free Doxorubicin and Doxorubicin loaded CS MNPs on MCF-7/Dox. When Doxorubicin is loaded on CS MNPs, IC_{50} values are decreasing. Since the efficiency of Doxorubicin increases, required amount of the drug 15 times decreases.

3.3.2. Bortezomib Loading on CS MNPs

3.3.2.1. Standard curve of Bortezomib

Standard curve of Bortezomib (Figure 3.34) was generated with the spectrophotometric readings of 1/10 diluted stock concentration at 260 μM , 130 μM , 65 μM , 32.5 μM , 16.2 μM , and 8 μM drug solutions.

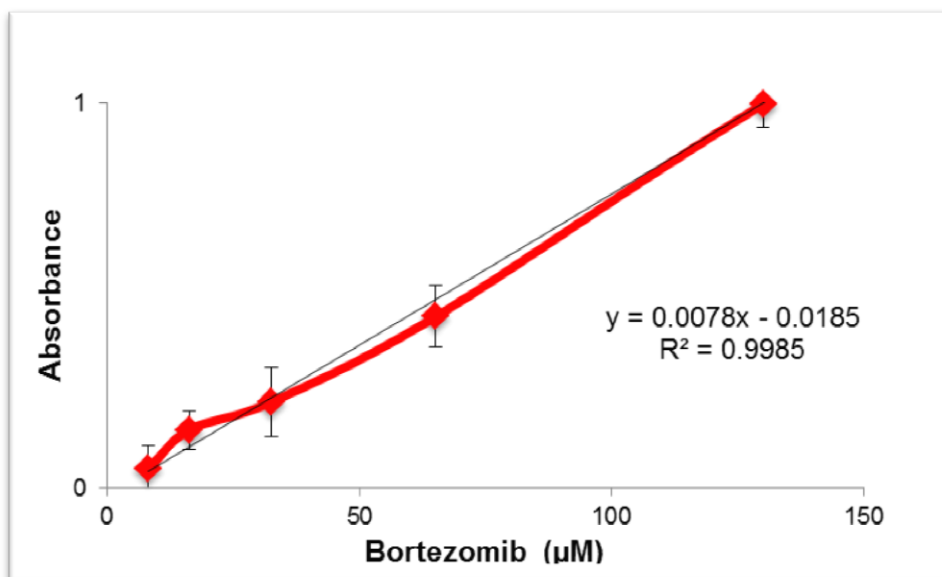


Figure 3.34. Standard curve of Bortezomib obtained by spectrophotometric measurements of known drug concentrations at 270 nm.

3.3.2.2. Bortezomib Loading on Synthesized CS MNPs

500 μl CS MNP-S₁ solution (5 mg/ml) and various amounts of Bortezomib were incubated on rotator for 24hrs. After the incubation period, supernatant was read on spectrophotometer at 270 nm against the supernatant of CS MNP and buffer. Quantification of Bortezomib amount was made with the help of Standard Curve.

For the optimization of Bortezomib loading efficiency, different solutions such as acetate, phosphate buffered saline and potassium phosphate buffer were used at different pH values. The highest loading efficiency was obtained as about 5 μM of Bortezomib at pH 4.7 acetate buffer (Figure 3.35).

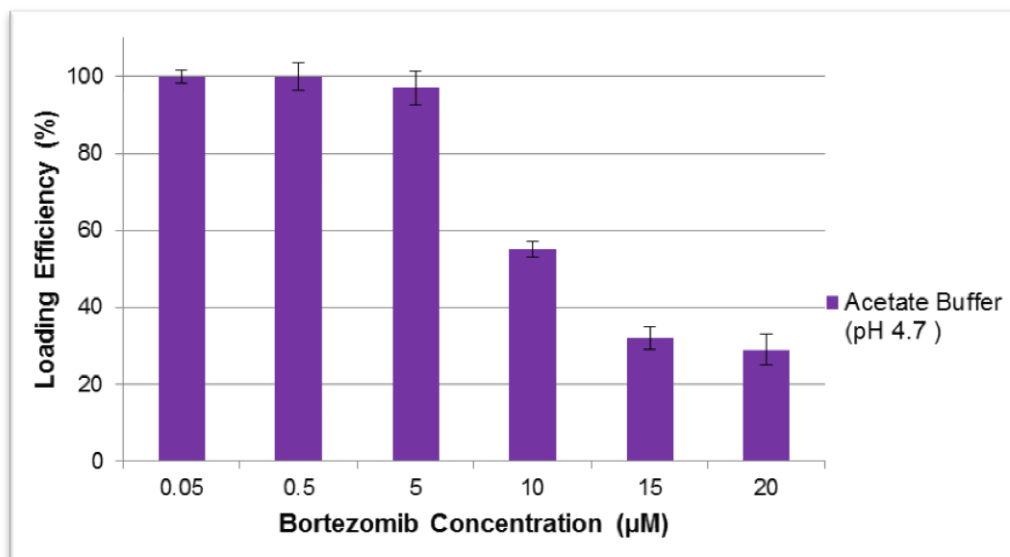


Figure 3.35. Bortezomib concentration versus loading efficiency in acetate buffer (pH 4.7).

The protonated amino groups of chitosan generate a swelling osmotic pressure at low pH and when these amino groups are deprotonated at high pH's, the swelling osmotic pressure disappears.

Either crosslinked or uncrosslinked chitosan polymer get swollen in acidic media and underwent disintegration (Pieróget *al.*, 2009). The chitosan molecules around the magnetic nanoparticle swell in acetate buffer pH 4.7. Therefore, Bortezomib can not be entrapped at high quantities by the chitosan layers so the loading efficiency is low at this pH.

Loading efficiency of Bortezomib was higher (10 µM) in PBS Buffer (pH 7.2) than the acetate buffer. About half of the absorbed drug is released at acidic pH because of the swelling behavior of chitosan (Figure 3.36).

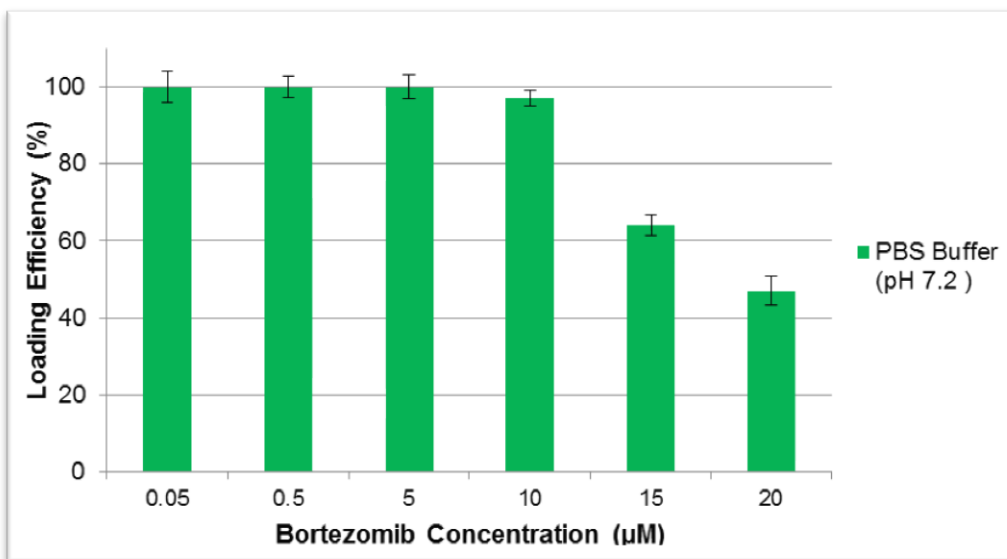


Figure 3.36. Bortezomib concentration versus loading efficiency in PBS buffer (pH 7.2).

Although, the swelling of chitosan molecules is an important factor for the preservation of the loaded drug in the nanoparticle, the protonation of amino groups is a desired feature for the ionic interaction between the drug and chitosan layer. The PBS buffer (pH 6.0) was used to provide weak acid medium for the protonation of chitosan during the loading process. 10 µM Bortezomib was loaded on CS MNPs with 98% efficiency and 15 µM Bortezomib was loaded with 67% efficiency (Figure 3.37).

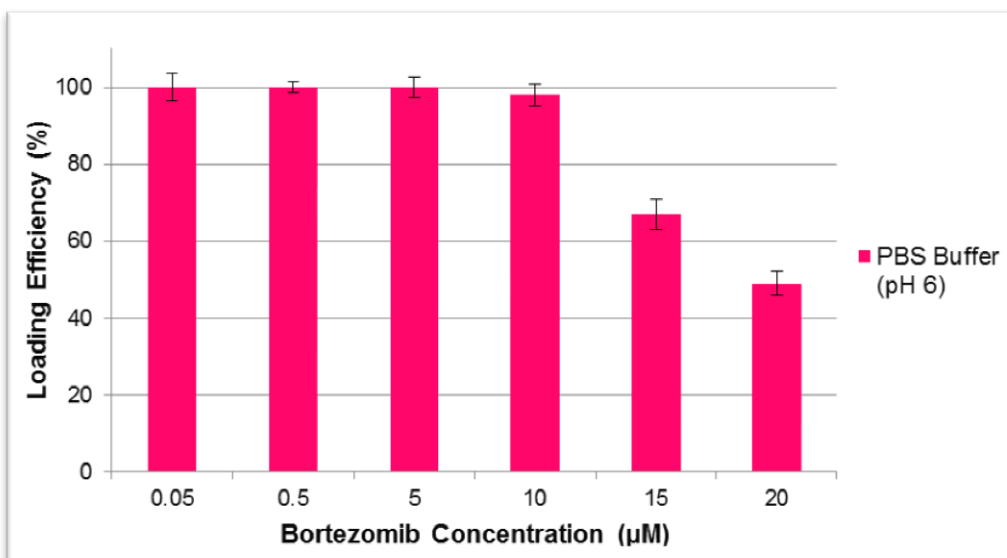


Figure 3.37. Bortezomib concentration versus loading efficiency in PBS buffer (pH 6.0).

The ionic strength of the PBS buffer is high and this would lead to an increase in swelling of chitosan layer. In order to increase the efficiency by decreasing the ionic strength of media, potassium phosphate (K_2HPO_4/KH_2PO_4) buffer (pH 6.0) was chosen as loading buffer(Figure 3.38).

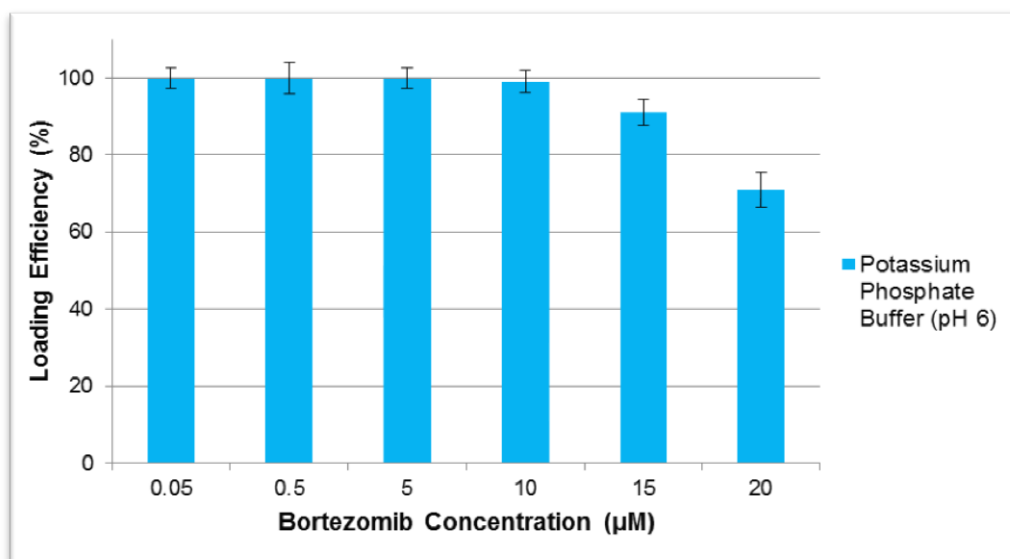


Figure 3.38. Bortezomib concentration versus loading efficiency in phosphate buffer (pH 6.0).

Bortezomib loading efficiency increased with potassium phosphate buffer (pH 6.0) to 99% of 10 μM Bortezomib and 91% of 15 μM Bortezomib.

Bortezomib was efficiently loaded on CS MNPs and loading efficiency was optimized by changing loading pH with different buffers. The highest loading efficiency was obtained at potassium phosphate buffer (K_2HPO_4/KH_2PO_4) pH 6.0 (Figure 3.39).

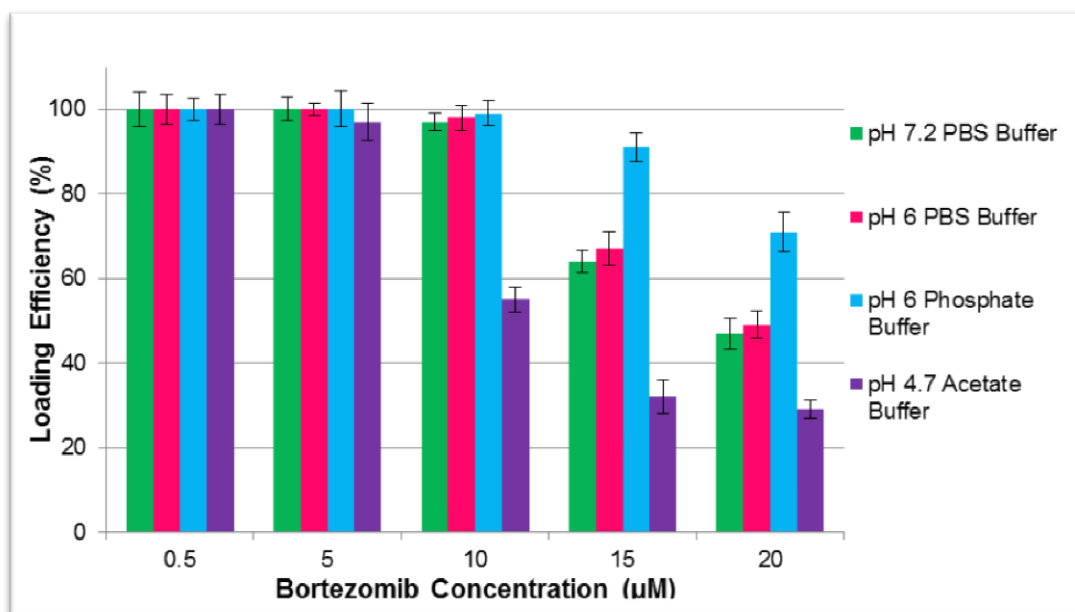


Figure 3.39. Highest loading efficiency was optimized with various loading buffers.

In order to see the temperature effect on loading efficiency, Bortezomib was loaded at 50°C. However, increase in temperature did not result with a significant increase on the loading efficiency. Bortezomib loading efficiencies of CS MNPs were determined at pH 6.0, potassium phosphate buffer (Table 3.2).

Table 3.2. Bortezomib loading efficiencies on CS MNPs.

Loading efficiencies and loaded amounts of Bortezomib on CS MNPs					
Bortezomib Concentration (µM)	5	7.5	10	15	20
Bortezomib Loading Efficiency (%)	100	100	99	91	53
Loaded Amount of Bortezomib (µg/ml)	19	29	38	52	54

3.2.2.3. FTIR Analyses of Bortezomib Loaded CS MNPs

The FTIR analyses were performed in order to confirm the loading Bortezomib on CS MNPs. The peaks at $1380-1310\text{ cm}^{-1}$ indicating the B-O stretching and $3300-3200\text{ cm}^{-1}$ reflecting the B-O-H stretching of boronic acid belonging to the Bortezomib were observed in FTIR spectrum of both Bortezomib and Bortezomib loaded CS MNPs as shifted to $1355-1356\text{ cm}^{-1}$ and $3216-3226\text{ cm}^{-1}$ (Figure 3.40). According to these results; Bortezomib loading on CS MNPs was successfully achieved.

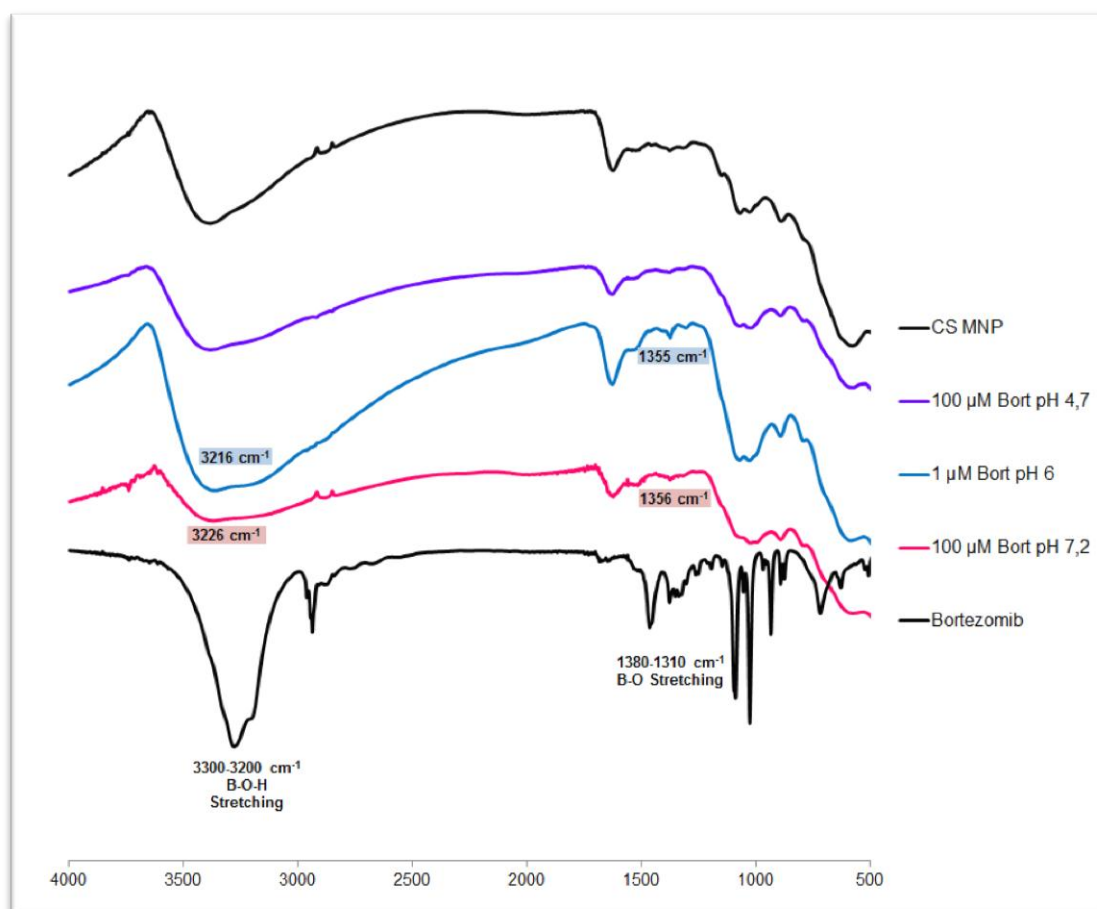


Figure 3.40. FTIR analyses of chitosan coated magnetic nanoparticles, Bortezomib and Bortezomib loaded chitosan coated magnetic nanoparticles.

3.2.2.4. Stability of Bortezomib Loaded Nanoparticles

The stability of Bortezomib loaded nanoparticles was evaluated up to 8 weeks in phosphate buffer (pH 7.4) at 37°C, which mimics the physiological conditions (Figure 3.41). Results show that the stability of Bortezomib loaded CS MNP-S₁ nanoparticles was around 85% stable for both 37°C and 4°C at pH 7.4. The stability of nanoparticles did not significantly change with temperature.

These results demonstrate that Bortezomib loaded CS MNPs were quite stable at both 37°C and 4°C (pH 7.4), and can be stored safely. The stability of drug loaded CS MNPs is critically important for both preservation of the drug in the active form through the shelflife and protection of stability in the bloodstream to limit the adverse effects of drug to the healthy tissue during the targeting period. Otherwise, instable nanoparticles would release the drug before the delivery of particles to the target site (Ducry & Stump, 2009).

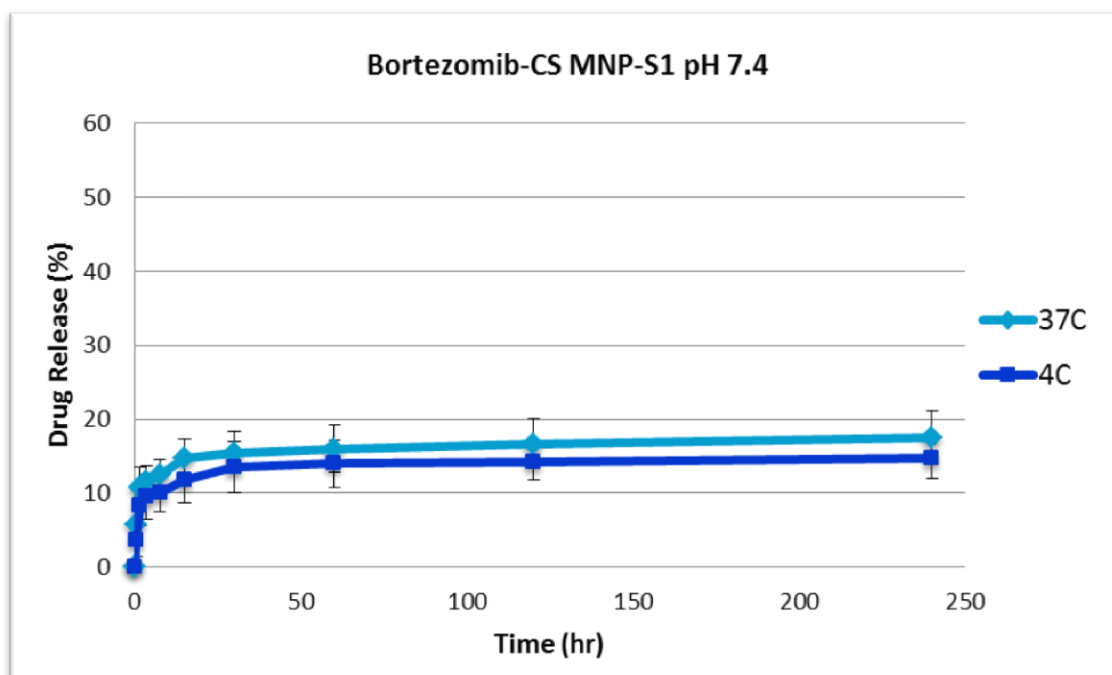


Figure 3.41. Stability of Bortezomib loaded CS MNP-S₁ in PBS buffer (pH 7.4).

3.2.2.5. Bortezomib Release From the Nanoparticles

Bortezomib release profiles and stability analyses of chitosan magnetic nanoparticles were studied by considering different parameters such as pH, buffer type, temperature of nanoparticles. Bortezomib release was investigated at different pH values (pH 4.2 and 6.0) which mimic endosomal conditions.

CS MNPs release about 51% and 28% of the loaded Bortezomib at pH 4.2 and pH 6.0, respectively during the first 15 hours (Figure 3.42). The chitosan is known to exhibit pH-dependent swelling and controlled drug release properties (Bergeret *et al.*, 2004).

A burst release of Bortezomib from CS MNPs was observed at the initial stage of 30 min at pH 4.2 as 18% and at pH 6.0 as 12%. Then a slower release was observed after 7 hours (Figure 3.43).

Drug release rates of CS MNPs were significantly different at release mediums with various pH values. The pH has a remarkable effect on the release of Bortezomib from the chitosan coated nanoparticles. The release of Bortezomib was quite higher at pH 4.2 than pH 6.0 for CS MNPs (Figure 3.43).

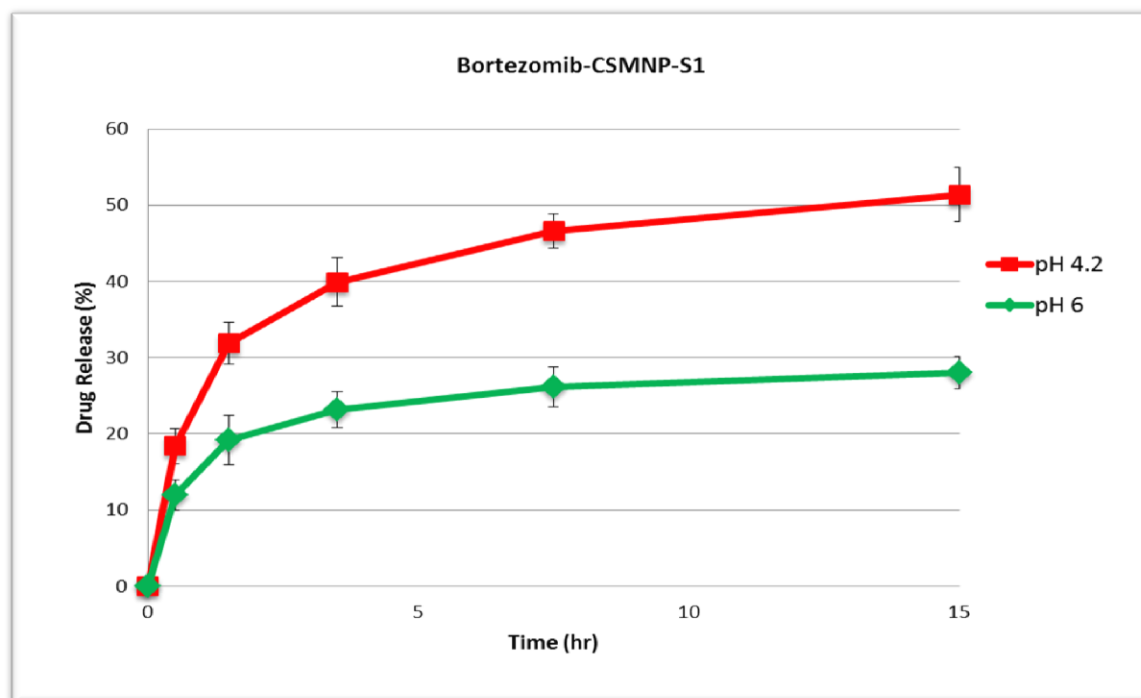


Figure 3.42. Bortezomib release graph of S₁ and S₄ nanoparticles at pH 4.2 and 6.0.

3.2.2.6. Cellular Uptake of Bortezomib Loaded CS MNPs

Cellular uptake of the Bortezomib loaded CS MNP-S₁ nanoparticles were investigated by fluorescence microscopy on HeLa and SiHa cervical cancer cells; obtained images are given in Figure 3.43. The nuclei of the cells are visualized with Dapi staining (Figure 3.43.b). Bortezomib loaded CS MNPs were overnight incubated on rotator with FITC, a fluorescent chemical, having a bright green color in order to be visualized under microscopy. The reflected green color inside the cell indicates that Bortezomib loaded nanoparticles were internalized by HeLa and SiHa cells, expressing the efficient cellular uptake of the particles (Figure 3.43. a).

Chitosan, which has a positive zeta potential, can have interaction with the negative domain of cell membranes by nonspecific electrostatic interactions. MNPs, with their tiny size and positive surface charge, showed a high electrostatic affinity for the cell membrane. Cellular uptake was initiated by nonspecific interactions between nanoparticles and cell membranes. It was reported that A549 cell uptake of chitosan nanoparticles occurred predominantly by adsorptive endocytosis, mediated in part by clathrin, but not by passive diffusion or by fluid-phase endocytosis (Huang *et al.*, 2002). Cellular uptake of N-acetyl histidine-conjugated glycol chitosan self assembled nanoparticles also was reported to internalize by adsorptive endocytosis (Park *et al.*, 2006). There were no reports of chitosan specific receptors on cell membranes (Ge *et al.*, 2009).

Internalization of drug loaded nanoparticles can be clearly observed by the intensity of fluorescent color of FITC dye in the cells. In Figure 3.43, Bortezomib loaded nanoparticles accumulate both in the cytoplasm and nuclei of the cells.

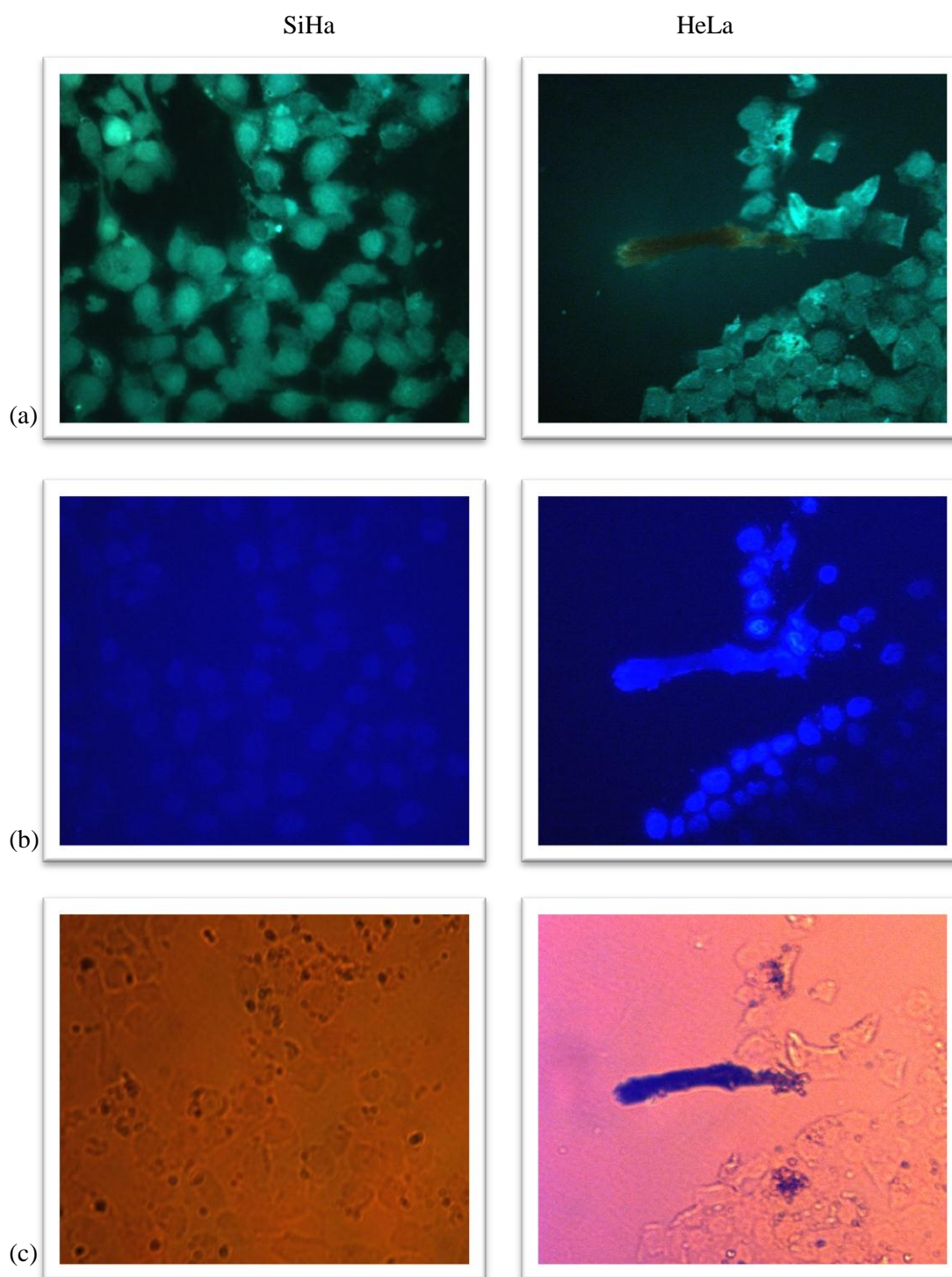


Figure 3.43. Cellular uptake images of Bortezomib loaded CS MNP-S₁ nanoparticles, applied on SiHa and HeLa cells (a) Bortezomib loaded nanoparticles are visualised in the cells at green filter, (b) Nuclei of the cells are labelled with Dapi staining, (c) Images of SiHa and HeLa cells, observed at bright field.

3.2.2.7. Cell Proliferation Assay With XTT Reagent

XTT cell proliferation assay was performed to determine the effect of Bortezomib and Bortezomib loaded CS MNPson SiHa and HeLa cervical cancer cells. After 72 hours of incubation, cell viability profiles and IC_{50} values were determined for each particular treatment and cell type. Figure 3.44 and Figure 3.45 demonstrates the antiproliferative effects of Bortezomib and Bortezomib loaded CS MNPson SiHa cells respectively.

The IC_{50} value of Bortezomib treated SiHa cells was found as 40 nM, which is consistent with the study of Dandan *et al.*, (2011). They have obtained 47.22% inhibition on proliferation of SiHa cells with MTT assay, when 40 nM Bortezomib was applied for 72 h. Kamer *et al.*, (2009) indicated that 10 nM Bortezomib resulted in 20% decrease in the proliferation rate of SiHa cells with MTT assay. In their study, after 12 h serum starvation they have applied Bortezomib for 24 h.

The IC_{50} value of Bortezomib loaded CS MNP treated SiHa cells was 3 nM. This remarkable decrease in the IC_{50} values is demonstrated in Figure 3.46. Bortezomib loading on CS MNPs increases the drug efficiency and decreases the required amount of drug to inhibit the 50% proliferation of cancer cells.

Figure 3.47 and Figure 3.48 demonstrates the antiproliferative effects of Bortezomib and Bortezomib loaded CS MNPs on HeLa cells, respectively.

The graphs show a gradual decrease in cell proliferation with increasing concentrations of Bortezomib and Bortezomib loaded CS MNPs. However, loading of Bortezomib on CS MNPs increases the efficiency of drug and decreases the required amount of drug to inhibit the proliferation of 50% of cells (Figure 3.47 and 3.48). The cell killing ability of Bortezomib released from CS MNPs was higher than free Bortezomib for both SiHa and HeLa cells.

The graphs show a gradual decrease in cell proliferation with increasing concentrations of Bortezomib and Bortezomib loaded CS MNPs. However, loading of Bortezomib on CS MNPs increases the efficiency of drug and decreases the required amount of drug to inhibit the proliferation of 50% of cells (Figure 3.46 and 3.49).

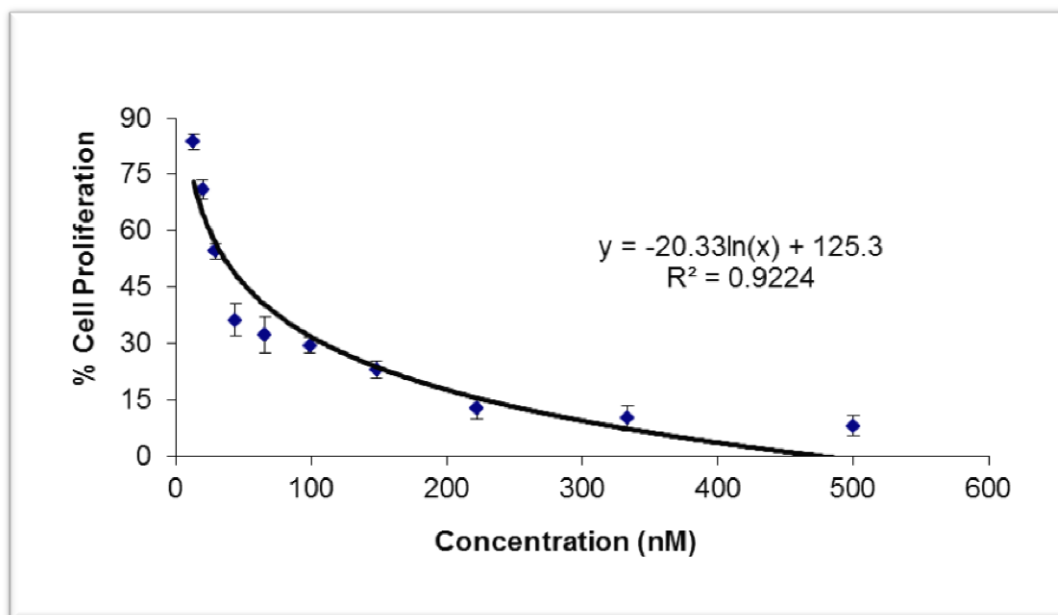


Figure 3.44. Cell proliferation profiles of SiHa ($IC_{50}=40$ nM) cells after exposure to increasing concentrations of Bortezomib.

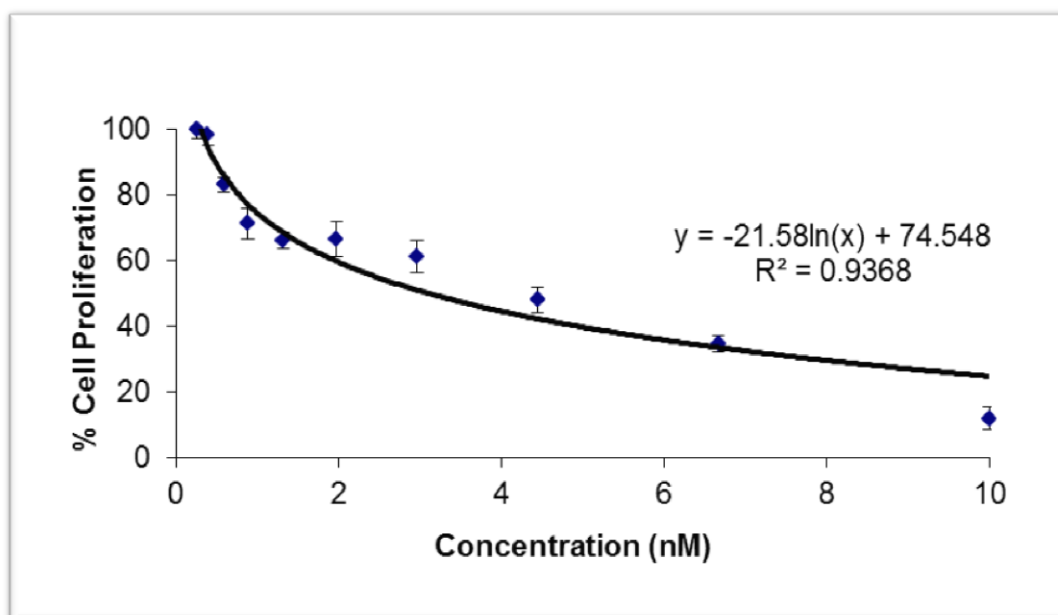


Figure 3.45. Cell proliferation profiles of SiHa ($IC_{50}=3$ nM) cells after exposure to increasing concentrations of Bortezomib loaded CS MNPs.

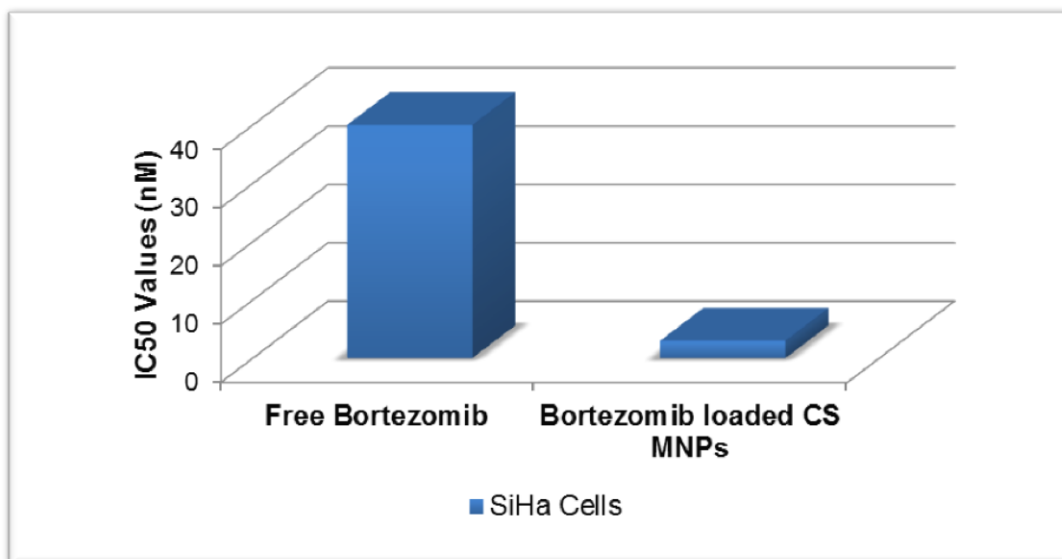


Figure 3.46. The comparison graph of IC₅₀ values of free Bortezomib and Bortezomib loaded CS MNPs on SiHa cells. When Bortezomib is loaded on CS MNPs, IC₅₀ values are decreasing. Since the efficiency of Bortezomib increases, required amount of the drug approximately 13 times decreases.

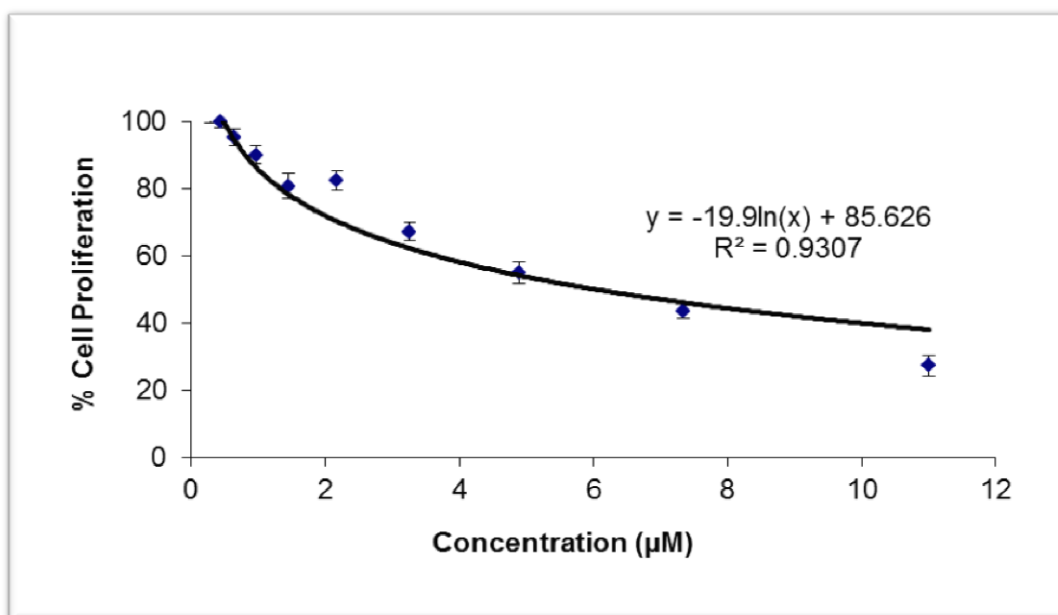


Figure 3.47. Cell proliferation profiles of HeLa (IC₅₀=6 µM) cells after exposure to increasing concentrations of Bortezomib.

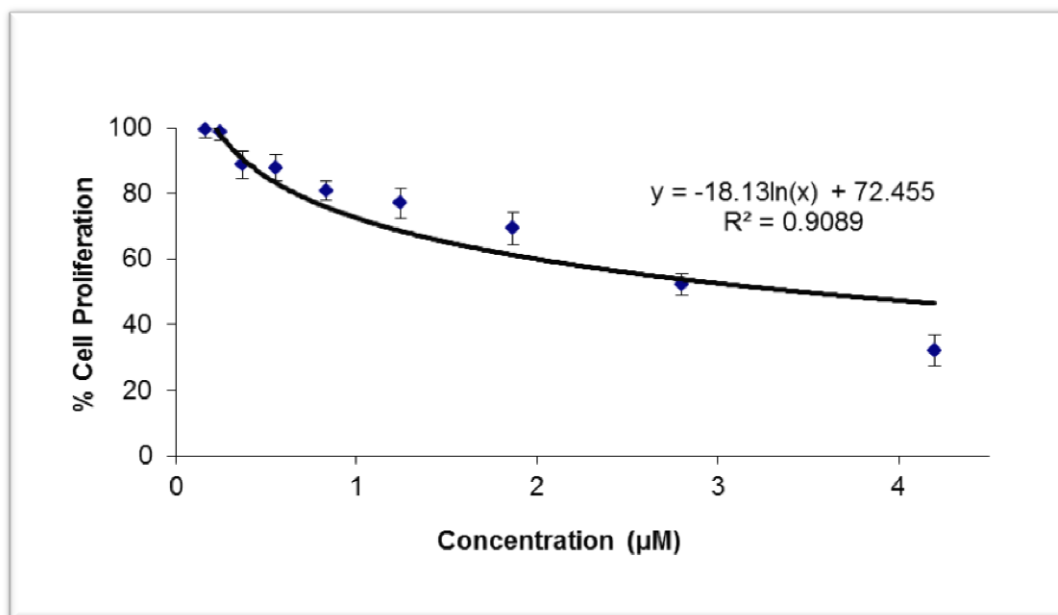


Figure 3.48. Cell proliferation profiles of HeLa ($IC_{50}=3.5 \mu M$) cells after exposure to increasing concentrations of Bortezomib loaded CS MNPs.

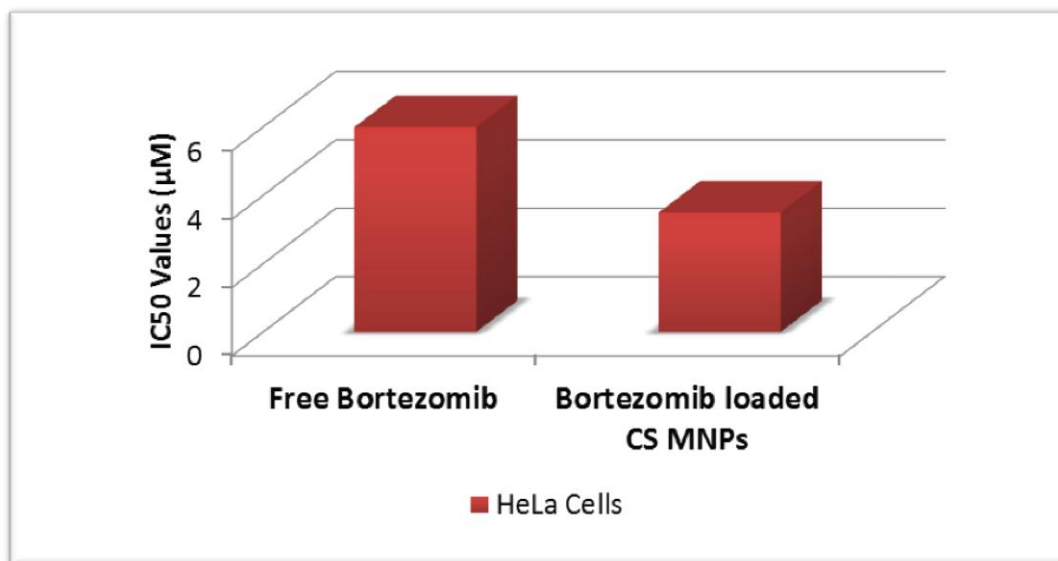


Figure 3.49. The comparison graph of IC_{50} values of free Bortezomib and Bortezomib loaded CS MNPs on HeLa cells. When Bortezomib is loaded on CS MNPs, IC_{50} values are decreasing. Since the efficiency of Bortezomib increases, required amount of the drug approximately 2 times decreases.

3.3. Effect of Drug Loaded CS MNPs on Apoptotic Gene Expressions

Quantitative PCR analyses were employed in order to investigate the effect of drug loaded/unloaded CS MNPs on apoptotic and antiapoptotic gene expression of MCF-7, MCF-7/Dox, SiHa and HeLa cells. For this purpose, the antiapoptotic *Bcl-2*, *Survivin*, *cIAP-2* and apoptotic *Noxa*, *Pumagenes* were chosen.

Bcl-2 (B cell lymphoma 2) is the founder member of the Bcl-2 family, which encodes various proteins that regulate stress-induced apoptosis and programmed cell death. There are antiapoptotic Bcl-2-like proteins (e.g., Bcl-2, Bcl-xL, Bcl-w, Mcl-1), proapoptotic Bax-like proteins (e.g., Bax, Bak) and proapoptotic BH3-only proteins (e.g., Bid, Bim/Bod, Bad, Bmf, Bik/Nbk, Blk, Noxa, Puma/Bbc3) in this family (Kvansakul *et al.*, 2008; Martinou and Youle 2011).

The extrinsic apoptotic pathway is triggered by cell-surface death receptors, while the intrinsic apoptotic pathway is modulated by the alterations of Bcl-2 family proteins in mitochondrial membrane. The release of cytochrome c and other apoptotic proteins from mitochondria is regulated by the Bcl-2 family of proteins. Some Bcl-2 family proteins can induce (proapoptotic members) or inhibit (antiapoptotic members) the release of cytochrome c to the cytosol, which activates caspase 9 and caspase 3, leading to apoptosis. Puma binds and inhibits all of the antiapoptotic Bcl-2 proteins. Noxa can function as a direct activator of Bak and Bax (Du *et al.*, 2011; Dai *et al.*, 2011).

Survivin and cIAP (Baculoviral IAP repeat-containing protein 3) are the members of the inhibitor of apoptosis (IAP) family. The survivin and cIAP proteins prevent the caspase activation, thereby leading to inhibition of apoptosis or programmed cell death.

3.3.1. Expression Levels of Doxorubicin Loaded CS MNP Treated Breast Cancer Cells

Gene expression studies by Q-PCR analyses revealed that the antiapoptotic *Bcl-2*, *Survivin* and *cIAP-2* genes were down regulated in free Doxorubicin treated or Doxorubicin loaded CS MNP treated MCF-7 cells as compared to untreated control and empty CS MNP treated MCF-7 cells (Figure 3.50).

At the same time, the expression levels of apoptotic *Puma* and *Noxa* genes were >13 times and >7 times up regulated, respectively in free Doxorubicin treated or Doxorubicin loaded CS MNP treated cells as compared to untreated control and empty CS MNP treated MCF-7 cells (Figure 3.50). These results confirm that the MCF-7 cells treated with drug loaded CS MNPs were routed to apoptosis with the aid of *Puma* and *Noxa* gene expressions.

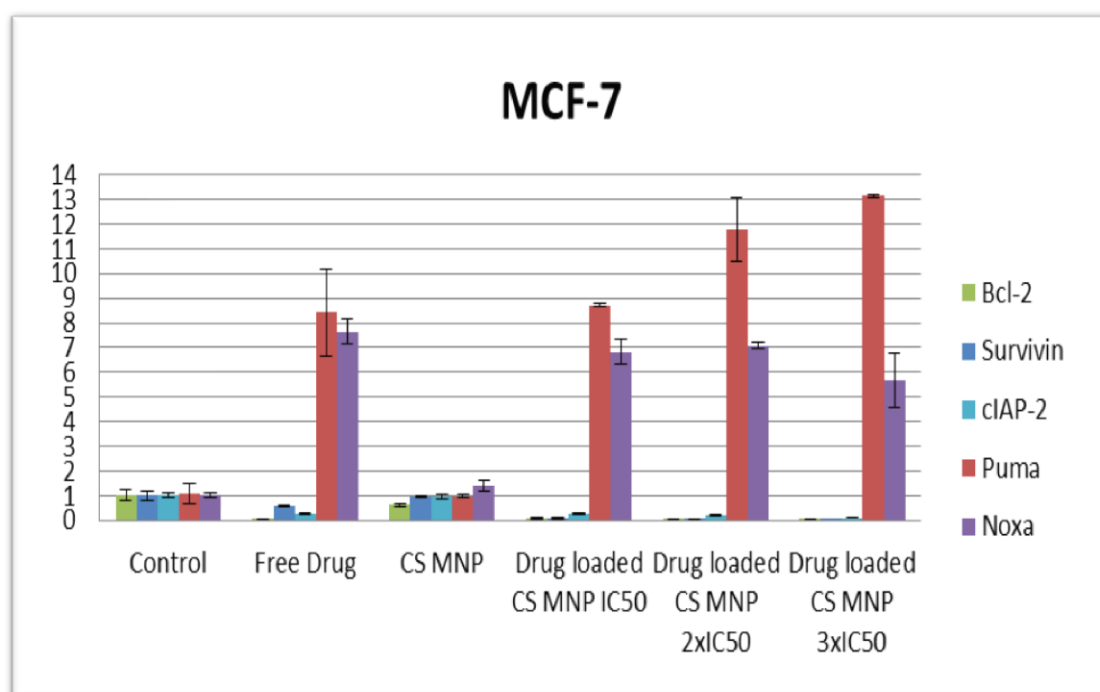


Figure 3.50. The expression levels of antiapoptotic (*Bcl-2*, *Survivin* and *cIAP-2*) and apoptotic (*Puma* and *Noxa*) genes at untreated control cells, and free Doxorubicin, empty CS MNP and Doxorubicin loaded CS MNP (at amounts corresponding to IC_{50} values, 2x and 3x) treated MCF-7 cells.

Gene expression levels of apoptotic *Puma* and *Noxa* genes were >8 times and >5 times up regulated, respectively in free Doxorubicin treated or Doxorubicin loaded CS MNP treated cells as compared to untreated and CS MNPtreated MCF-7/Dox cells (Figure 3.51).

In MCF-7/Dox cells, expressions of *Survivin* and *cIAP-2* genes were not up regulated. However, antiapoptotic *Bcl-2* expression was unexpectedly up regulated in CS MNPtreated and 3xIC₅₀ amounts of Doxorubicin loaded CS MNP treated MCF-7/Dox cells. (Figure 3.51). The 5 times up regulation of *Bcl-2* gene expression could be considered as a response of the resistant MCF-7/Dox cells against the CS MNPs, because in MCF-7 cells, *Bcl-2* gene expression was not up regulated. This should be further studied.

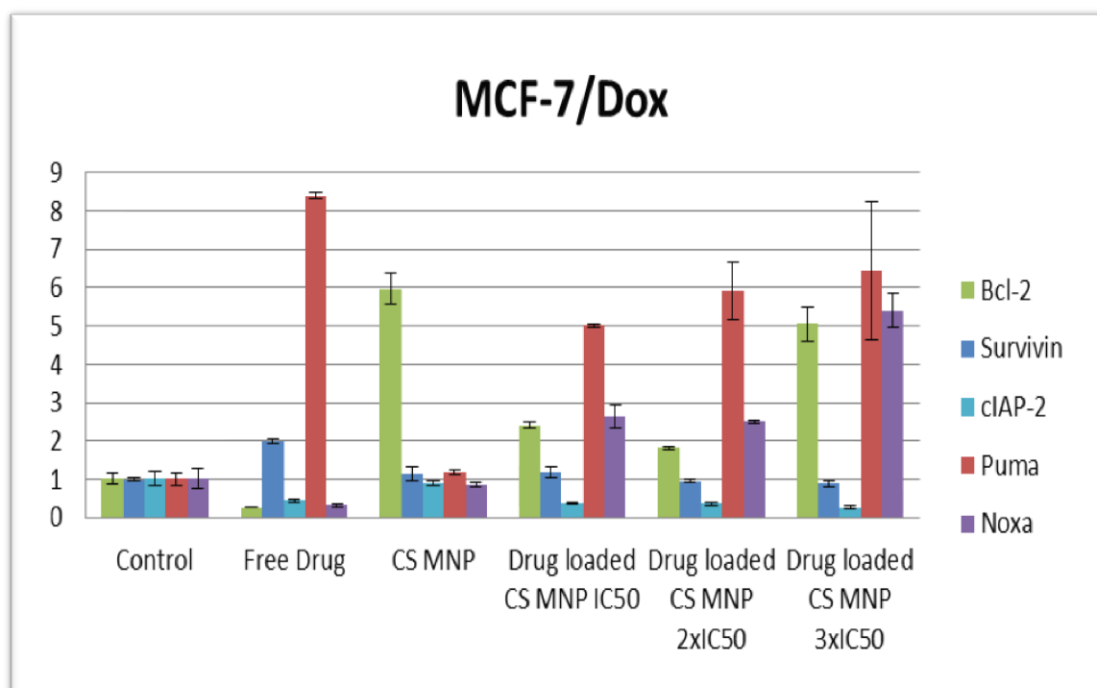


Figure 3.51. The expression levels of antiapoptotic (*Bcl-2*, *Survivin* and *cIAP-2*) and apoptotic (*Puma* and *Noxa*) genes at untreated control cells, and free Doxorubicin, empty CS MNP and Doxorubicin loaded CS MNP (at amounts corresponding to IC₅₀ values, 2x and 3x) treated MCF-7/Dox cells.

3.3.2. Expression Levelsof Bortezomib Loaded CS MNPTreated Cervical Cancer Cells

Gene expression analyses demonstrated that theexpression levels of apoptotic *Puma* and *Noxa* genes were >6.5 times and >8.5 times up regulated, respectively in free Bortezomib treated or Bortezomib loaded CS MNP treated cells as compared to control and CS MNPTreated SiHacells.

Furthermore, gene expressionlevels of antiapoptotic *Bcl-2*, *Survivin* and *cIAP-2* genes were down regulated in free Bortezomib or Bortezomib loaded CS MNP treated cells as compared to control and CS MNPTreated SiHa cells (Figure 3.52).

Smith et al., (2011) reported that *Bcl-2* inhibits Bortezomib induced *Noxa* mediated apoptosis. Therefore,according to the results of gene expression analyses, it can be concluded that Bortezomib or Bortezomib loaded CS MNPs inducesSiHa cells to apoptosis owing to the up regulation of *Noxa* and down regulation of *Bcl-2* genes.

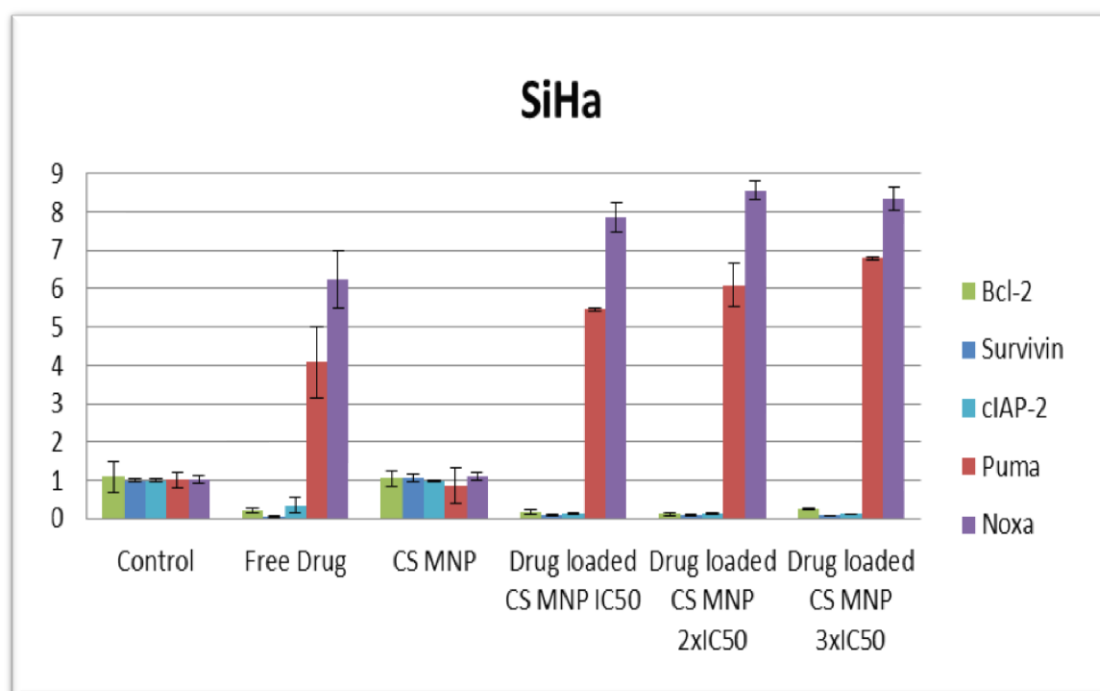


Figure 3.52. The expression levels of antiapoptotic (*Bcl-2*, *Survivin* and *cIAP-2*) and apoptotic (*Puma* and *Noxa*) genes at untreated control cells, and free Bortezomib, empty CS MNP and Bortezomibloaded CS MNP (at amounts corresponding to IC_{50} values, 2x and 3x) treated SiHa cells.

The expression of apoptotic *Puma* and *Noxa* genes were >11 times and >10 times up regulated, respectively in Bortezomib or Bortezomib loaded CS MNP treated cells. Besides, the antiapoptotic *Bcl-2*, *Survivin* and *cIAP-2* genes were down regulated in Bortezomib or Bortezomib loaded CS MNP treated HeLa cells (Figure 3.53). We can conclude as apoptosis was induced in Bortezomib or Bortezomib loaded CS MNP treated HeLa cells.

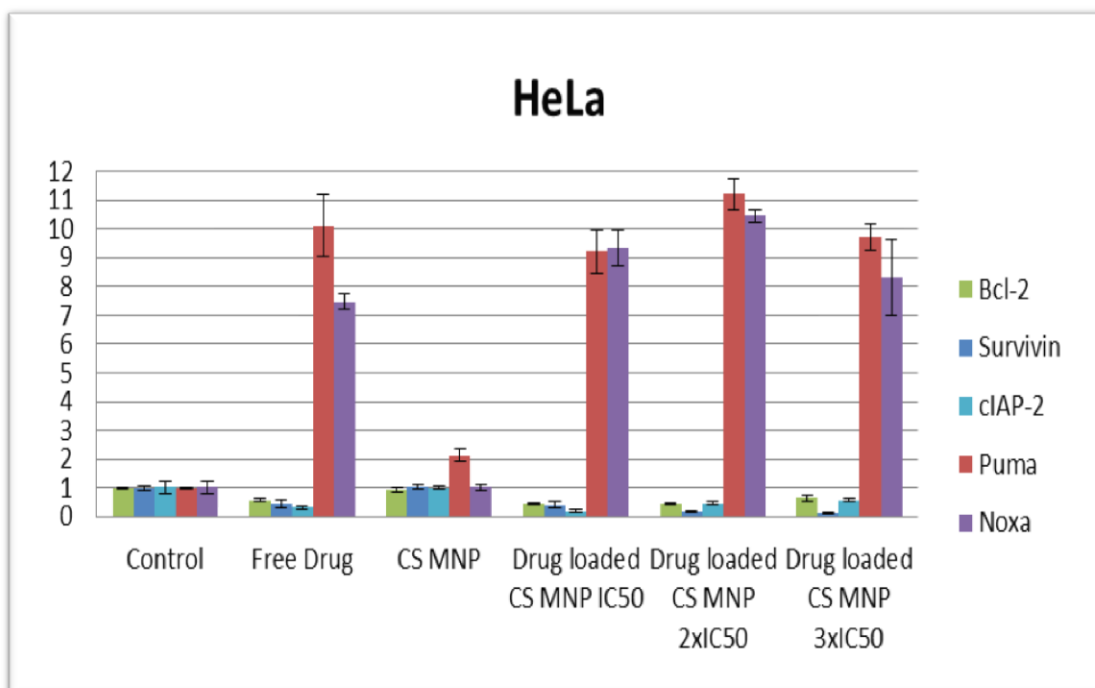


Figure 3.53. The expression levels of antiapoptotic (*Bcl-2*, *Survivin* and *cIAP-2*) and apoptotic (*Puma* and *Noxa*) genes at untreated control cells, and free Bortezomib, empty CS MNP and Bortezomib loaded CS MNP (at amounts corresponding to IC₅₀ values, 2x and 3x) treated HeLa cells.

CHAPTER4

CONCLUSION

Doxorubicin and Bortezomib loaded chitosan magnetic nanoparticles (CS MNPs) were synthesized to be used for targeting of tumor cells in the presence of magnetic field. Chitosan coat around the magnetic nanoparticles reduces the agglomeration, and provides internal cavities for loading of therapeutics and surface functional groups for modifications by signaling molecules.

Size tunable synthesis of chitosan magnetic nanoparticles at this small size range was firstly reported by Unsoy *et al.*, (2012). The average diameters of synthesized CS MNPs (S₁- S₄) are found in the range of 8 nm - 2 nm according to TEM images and 103 nm - 58 nm in DLS measurements. Bhattarai *et al.* (2008) reported that the difference between the diameters obtained by DLS and TEM reflects the size of chitosan layer for nanoparticles smaller than ≤200 nm (Unsoy *et al.*, 2012).

CS MNPs were synthesized at four different sizes by in situ precipitation method. This method is advantageous than the earlier published methods (Tiaboonchai and Limpeanchob 2007) because it is simple and carried out under mild conditions without using hazardous organic solvents, and nanoparticles obtained by this method are expected to have higher biocompatibility than covalently cross linked chitosan nanoparticles (Agnihotri *et al.*, 2004; Park *et al.*, 2010) as the chitosan was cross linked with looser, ionic interactions.

The characterization of synthesized nanoparticles was performed by X-ray diffraction (XRD), X-ray photoelectron spectroscopy (XPS/ESCA), Fourier transform infrared spectroscopy (FTIR), transmission electron microscopy (TEM), dynamic light scattering (DLS), thermal gravimetric analysis (TGA), and vibrating sample magnetometry (VSM) analyses. The XRD and XPS analyses proved that the synthesized iron oxide was magnetite (Fe₃O₄). The layer of chitosan on the magnetite surface was confirmed by FTIR. TGA results indicated that the chitosan content of CS MNPs were between 15 and 23 % by weight. CS MNPs were found noncytotoxic on cancer cell lines (MCF-7, MCF-7/Dox, SiHa and HeLa). Therefore, synthesized CS MNPs were superparamagnetic, biocompatible, biodegradable, hydrophilic and monodisperse nanoparticles that are appropriate nanocarriers for drug delivery and magnetic targeting applications such as MRI and hyperthermia.

The synthesis of chemotherapeutic loaded CS MNPs for magnetic field targeted drug delivery is a fairly novel subject of research. However, Yuan *et al.*, (2008) have synthesized Doxorubicin loaded chitosan grafted copolymer coated magnetic nanoparticles for targeted drug delivery; they did not perform a detailed investigation on nanoparticle characterization and their cellular uptake.

In this study, different sized CS MNPs were efficiently loaded with Doxorubicin for the *in vitro* targeted delivery applications on breast cancer cells. The optimum loading efficiency, stability and release profiles of Doxorubicin loaded nanoparticles were determined. The highest loading efficiency was obtained for CS MNP-S₁ nanoparticles (97-98%). This may be due to the highest chitosan content (obtained as 23% by TGA analyses) of CS MNP-S₁. The FTIR results supported that the Doxorubicin loading on CS MNPs was successfully achieved.

The Doxorubicin release profiles showed pH dependent, slow release pattern. The CS MNPs released most of the Doxorubicin load at pH 4.2, while the nanoparticles are highly stable at pH 7.4. Chitosan has primary amino groups with pKa values 6.3. At pH below pKa, most of the amino groups are protonated making chitosan a water soluble cationic polyelectrolyte. At pH above the pKa, the amino groups of chitosan are deprotonated, and this polymer becomes insoluble (Zemskova *et al.*, 2005). Thus, CS MNPs were stable at pH 7.4 and drug was not released at neutral pH, which is the pH of blood. The drug release profiles showed a pH dependent, slow release pattern. As the pH decreased, the drug release increased. Drug is released at the targeted cancer cells, because the pH of tumor tissue and endosomes are acidic.

Zeta potential of CS MNPs were positive at pH < 6.3 due to the presence of protonated amino groups of chitosan on particle surface. Protonated CS MNPs at acidic pH are water soluble and bioadhesive to negatively charged surfaces such as cell membrane. Chitosan coating enhances the cellular uptake of polar drugs across the cell surfaces. Results of Harush-Frenkel *et al.*, (2007) also show that cellular uptake of positively charged nanoparticles is 3 times higher than that of negatively charged nanoparticles, owing to the negatively charged cell surface. Fluorescence microscopy images have revealed that the Doxorubicin loaded CS MNPs were taken up by the cells and accumulated around the nucleus, so that Doxorubicin is successfully delivered near to the nucleus, where the drug shows its anticancer activity.

The efficacy of Doxorubicin loaded CS MNPs were higher than free Doxorubicin due to the higher uptake and slower release of drug inside the tumor cells and tissues. The lower amounts of Doxorubicin were enough to decrease the proliferation rates of cancer cells when loaded on CS MNPs.

Doxorubicin loaded CS MNPs were more toxic on Doxorubicin resistant MCF-7 cells than free drug. This confirms that the released drug is active. Application of Doxorubicin as loaded on CS MNPs caused the reversal of drug resistance by increasing the accumulation of Doxorubicin in the cells. Therefore, the Doxorubicin loaded CS MNPs, produced in this study, are pH sensitive and suitable nanocarriers for targeted drug delivery.

Another recent chemotherapeutic drug, Bortezomib, was loaded on CS MNPs to be applied on cervical cancer cells. Bortezomib loaded chitosan magnetic nanoparticles have not been reported in the literature, yet. For the optimization of Bortezomib loading efficiency, different buffer solutions were used at different pH values. The highest loading efficiency of Bortezomib was obtained in Phosphate Buffer (pH 6.0). The loading efficiency of Bortezomib in PBS Buffer (pH 7.4) was higher than the acetate buffer. The ionic strength in the neutral swelling medium is smaller than that in acidic and basic media, therefore having the higher swelling capacities. The swelling of nanoparticles results with the escape and release of loaded drug from the cavities of particles. The protonated amino groups of chitosan generate a swelling osmotic pressure at lower pHs and when these amino groups are deprotonated, the swelling osmotic pressure disappears at higher pHs. So, the most of the Bortezomib was released at pH 4.2. The Bortezomib loaded nanoparticles were highly stable at 37°C and 4°C, pH 7.4 up to 8 weeks.

Bortezomib loaded CS MNPs were efficiently internalized by the cells and accumulated both in the cytoplasm and nucleus of the cells, where Bortezomib shows its anticancer activity. Bortezomib loaded CS MNPs were more toxic on both SiHa and Hela cervical cancer cells than free drug, which is the evidence of Bortezomib release from the delivered CS MNPs. When Bortezomib was given as loaded on CS MNPs, required amount of drug to kill 50% of the cells (IC_{50} values) remarkably decreases due to the efficacy of drug highly increases. As it was also emphasized in the literature, application of drugs as loaded on nanoparticles increases the efficacy as compared to free drug by providing slow release rates of drugs inside the targeted cells.

Antiapoptotic Bcl-2 inhibits apoptosis by blocking the release of cytochrome c in control or empty CS MNP treated cells. However, the expression levels of Bcl-2 gene were so low in the free drug or drug loaded CS MNP treated cells. Antiapoptotic Survivin and cIAP inhibit apoptosis by restricting the caspase activation in control or empty CS MNP treated cells. The expression levels of Survivin and cIAP-2 genes were down regulated in the drug treated cells.

Proapoptotic Puma and Noxa initiate apoptosis by inhibiting antiapoptotic proteins and activating apoptotic proteins. The expression levels of proapoptotic Puma and Noxa genes were highly up regulated in the drug loaded CS MNP cells as well as free drug treated cells, which reflects the efficacy of drug as loaded on CS MNPs.

According to these results, it is inferred that the synthesized drug loaded chitosan magnetic nanoparticles has a high potential to be used as a pH responsive drug delivery system, which can be targeted to tumor cells under magnetic field. These CS MNPs may further be investigated for the delivery of other therapeutics.

REFERENCES

- Acharya, S., Dilnawaz, F., & Sahoo, S. K. (2009). Targeted epidermal growth factor receptor nanoparticle bioconjugates for breast cancer therapy. *Biomaterials*, 30(29), 5737-5750.
- Adams, J. (2004). The proteasome: a suitable antineoplastic target. *Nature Reviews Cancer*, 4(5), 349-360.
- Agnihotri, S. A., Mallikarjuna, N. N., & Aminabhavi, T. M. (2004). Recent advances on chitosan-based micro- and nanoparticles in drug delivery. *Journal of Controlled Release*, 100(1), 5-28.
- Allen, T. M. (2002). Ligand-targeted therapeutics in anticancer therapy. *Nature Reviews Cancer*, 2(10), 750-763.
- Al-Qadi, S., Grenha, A., Carrión-Recio, D., Seijo, B., & Remuñán-López, C. (2012). Microencapsulated chitosan nanoparticles for pulmonary protein delivery: in vivo evaluation of insulin-loaded formulations. *Journal of Controlled Release*, 157(3), 383-390.
- American Cancer Society. (2009) *Cancer Facts & Figures*. Atlanta.
- Amidi, M., Mastrobattista, E., Jiskoot, W., & Hennink, W. E. (2010). Chitosan-based delivery systems for protein therapeutics and antigens. *Advanced Drug Delivery Reviews*, 62(1), 59-82.
- Andrade, F., Antunes, F., Vanessa Nascimento, A., Baptista da Silva, S., das Neves, J., Ferreira, D., & Sarmento, B. (2011). Chitosan formulations as carriers for therapeutic proteins. *Current Drug Discovery Technologies*, 8(3), 157-172.
- Arbab, A. S., Bashaw, L. A., Miller, B. R., Jordan, E. K., Lewis, B. K., Kalish, H., & Frank, J. A. (2003). Characterization of Biophysical and Metabolic Properties of Cells Labeled with Superparamagnetic Iron Oxide Nanoparticles and Transfection Agent for Cellular MR Imaging. *Radiology*, 229(3), 838-846.
- Arruebo, M., Fernández-Pacheco, R., Ibarra, M. R., & Santamaría, J. (2007). Magnetic nanoparticles for drug delivery. *Nano Today*, 2(3), 22-32.
- Artursson, P., Lindmark, T., Davis, S. S., & Illum, L. (1994). Effect of chitosan on the permeability of monolayers of intestinal epithelial cells (Caco-2). *Pharmaceutical Research*, 11(9), 1358-1361.
- Asha Rani, P. V., Low Kah Mun, G., Hande, M. P., & Valiyaveetil, S. (2008). Cytotoxicity and genotoxicity of silver nanoparticles in human cells. *ACS Nano*, 3(2), 279-290.

Ashley, C. E., Carnes, E. C., Phillips, G. K., Padilla, D., Durfee, P. N., Brown, P. A., Hanna, T. N., Liu, J., Phillips, B., Carter, M. B., Carroll, N. J., Jiang, X., Dunphy, D. R., Willman, C. L., Petsev, D. N., Evans, D. G., Parikh, A. N., Chackerian, B., Wharton, W., Peabody, D. S., & Brinker, C. J. (2011). The targeted delivery of multicomponent cargos to cancer cells by nanoporous particle-supported lipid bilayers. *Nature Materials*, 10(5), 389-397.

Aslam, M., & Dent, A. (1998). *Bioconjugation: protein coupling techniques for the biomedical sciences*. London: Macmillan Reference.

Aydin, R., & Pulat, M. (2012). 5-Fluorouracil encapsulated chitosan nanoparticles for pH-stimulated drug delivery: evaluation of controlled release kinetics. *J Nanomaterials*, 42.

Baldrick P. (2010) The safety of chitosan as a pharmaceutical excipient. *Regul.Toxicol. Pharm.*, 56, 290–299

Bartlett, D. W., Su, H., Hildebrandt, I. J., Weber, W. A., & Davis, M. E. (2007). Impact of tumor-specific targeting on the biodistribution and efficacy of siRNA nanoparticles measured by multimodality in vivo imaging. *Proceedings of the National Academy of Sciences*, 104(39), 15549-15554.

Berger, J., Reist, M., Mayer, J. M., Felt, O., Peppas, N. A., & Gurny, R. (2004). Structure and interactions in covalently and ionically crosslinked chitosan hydrogels for biomedical applications. *European Journal of Pharmaceutics and Biopharmaceutics*, 57(1), 19-34.

Berry, D. A., Cirrincione, C., Henderson, I. C., Citron, M. L., Budman, D. R., Goldstein, L. J., Martino, S., Perez, E.A., Muss, H.B., Norton, L., Hudis, C., & Winer, E.P. (2006) Estrogen-receptor status and outcomes of modern chemotherapy for patients with node-positive breast cancer. *JAMA: the journal of the American Medical Association*, 295(14), 1658-1667.

Bhattacharai, S. R., Kc, R. B., Kim, S. Y., Sharma, M., Khil, M. S., Hwang, P. H., Chung, G.H., & Kim, H.Y. (2008) N-hexanoyl chitosan stabilized magnetic nanoparticles: implication for cellular labeling and magnetic resonance imaging. *J Nanobiotechnol*, 6(1), 1-9.

Bhumkar, D. R., & Pokharkar, V. B. (2006). Studies on effect of pH on cross-linking of chitosan with sodium tripolyphosphate: a technical note. *AAPS PharmSciTech*, 7(2), E138-E143.

Biophan Technologies, Inc., (2013) Guided Drug Delivery, Available at: http://www.biophan.com/index.php?option=com_content&task=view&id=260&Itemid=425 (Accessed: 22 August 2013)

Borchard, G., Lueßen, H. L., de Boer, A. G., Verhoef, J., Lehr, C. M., & Junginger, H. E. (1996). The potential of mucoadhesive polymers in enhancing intestinal peptide drug absorption. III: Effects of chitosan-glutamate and carbomer on epithelial tight junctions in vitro. *Journal of Controlled Release*, 39(2), 131-138.

Boyle P, Levin B. (2008) World Cancer Report. Lyon:World Health Organization Press.

Bray, F., Ren, J. S., Masuyer, E., & Ferlay, J. (2013). Global estimates of cancer prevalence for 27 sites in the adult population in 2008. *International Journal of Cancer*, 132(5), 1133-1145.

Bumb A, Brechbiel M W, Choyke P L, Fugger L, Eggeman A, Prabhakaran D, Hutchinson J, Dobson P J (2008) Synthesis and characterization of ultra-small superparamagnetic iron oxide nanoparticles thinly coated with silica. *Nanotechnology*. August 20; 19(33): 335601.

Carrstensen, H., Müller, R. H., & Müller, B. W. (1992). Particle size, surface hydrophobicity and interaction with serum of parenteral fat emulsions and model drug carriers as parameters related to RES uptake. *Clinical Nutrition*, 11(5), 289-297.

Cavaillès, V., Gompel, A., Portois, M. C., Thenot, S., Mabon, N., & Vignon, F. (2002). Comparative activity of pulsed or continuous estradiol exposure on gene expression and proliferation of normal and tumoral human breast cells. *Journal of molecular endocrinology*, 28(3), 165-175.

Chabner, B. A., & Longo, D. L. (2011). *Cancer chemotherapy and biotherapy: principles and practice*. Wolters Kluwer Health.

Chakeres, D. W., & de Vocht, F. (2005). Static magnetic field effects on human subjects related to magnetic resonance imaging systems. *Progress in biophysics and molecular biology*, 87(2), 255-265.

Chatterjee, K., Zhang, J., Honbo, N., & Karliner, J. S. (2009). Doxorubicin cardiomyopathy. *Cardiology*, 115(2), 155-162.

Chen, D., Frezza, M., Schmitt, S., Kanwar, J., & Dou, Q.P. (2011). Bortezomib as the first proteasome inhibitor anticancer drug: current status and future perspectives. *Curr Cancer Drug Targets*. March; 11(3): 239–253.

Chithrani, B. D., Ghazani, A. A., & Chan, W. C. (2006). Determining the size and shape dependence of gold nanoparticle uptake into mammalian cells. *Nano letters*, 6(4), 662-668.

Cho, Y., Jang, J., Park, C., & Ko, S. (2000). Preparation and solubility in acid and water of partially deacetylated chitins. *Biomacromolecules*, 1, 609–614.

Cho, E. C., Xie, J., Wurm, P. A., & Xia, Y. (2009). Understanding the role of surface charges in cellular adsorption versus internalization by selectively removing gold nanoparticles on the cell surface with a I2/KI etchant. *Nano letters*, 9(3), 1080-1084.

Coates, J. (2000). Interpretation of infrared spectra, a practical approach. *Encyclopedia of analytical chemistry*. Wiley, Chichester, pp 10815–10837

Conforti, R., Boulet, T., Tomasic, G., Taranchon, E., Arriagada, R., Spielmann, M., Ducourtieux, M., Soria, J.C., Tursz, T., Delalogue, S., Michiels, S., & Andre, F. (2007). Breast cancer molecular subclassification and estrogen receptor expression to predict efficacy of adjuvant anthracyclines-based chemotherapy: a biomarker study from two randomized trials. *Annals of Oncology*, 18(9), 1477-1483.

Conner, S., Schmid, S.L. (2003). Regulated portals of entry into the cell. *Nature*, 422, 37–44.

Crawford, L.J., Walker, B., Ova, H., Chauhan, D., & Anderson, K.C. (2006). Comparative selectivity and specificity of the proteasome inhibitors, PS-341, and MG-132. *Cancer Res*, 66:6379–86.

Dai, H., Smith, A., Meng, X. W., Schneider, P. A., Pang, Y. P., & Kaufmann, S. H. (2011). Transient binding of an activator BH3 domain to the Bak BH3-binding groove initiates Bak oligomerization. *The Journal of Cell Biology*, 194(1), 39-48.

Dandan, Z., Yuquan, Z., Yuqin, J., Zuo, Z.Y., & Zuo, M.Z. (2011). Effects of bortezomib on inhibition of human cervical cancer SiHa cells and its mechanism. *Progress in Obstetrics and Gynecology*, Vol:20 (2):113-115,120

Daou, T. J., Pourroy, G., Begin-Colin, S., Greneche, J. M., Ulhaq-Bouillet, C., Legaré, P., Bernhardt, P., Leuvre, C., & Rogez, G. (2006). Hydrothermal synthesis of monodisperse magnetite nanoparticles. *Chemistry of Materials*, 18(18), 4399-4404.

Dash, M.; Chiellini, F.; Ottenbrite, R.M., & Chiellini, E. (2011). Chitosan-A versatile semi-synthetic polymer in biomedical applications. *Prog. Polym. Sci.*, 36, 981–1014.

De Campos, A., Sánchez, A., Alonso, M.J. (2001). Chitosan nanoparticles: a new vehicle for the improvement of the ocular retention of drugs. Application to cyclosporin A. *Int J Pharm.*, 224:159–68.

De Villiers, E. M., Fauquet, C., Broker, T. R., Bernard, H. U., & zur Hausen, H. (2004). Classification of papillomaviruses. *Virology*, 324(1), 17-27.

Decuzzi, P., & Ferrari, M. (2007). The role of specific and non-specific interactions in receptor-mediated endocytosis of nanoparticles. *Biomaterials*, 28:2915–22

Dodane, V., & Vilivalam, V.D. (1998). Pharmaceutical applications of chitosan. *Pharmaceutical Sciences and Technology Today*, 1(6):246-253.

Doerfler, W. (1991). Patterns of DNA methylation--evolutionary vestiges of foreign DNA inactivation as a host defense mechanism. A proposal. *Biological chemistry Hoppe-Seyler*, 372(8), 557.

Dönmez, Y., Akhmetova, L., İşeri, Ö. D., Kars, M. D., & Gündüz, U. (2011 a). Effect of MDR modulators verapamil and promethazine on gene expression levels of MDR1 and MRP1 in doxorubicin-resistant MCF-7 cells. *Cancer chemotherapy and pharmacology*, 67(4), 823-828.

Dönmez, Y., & Gündüz, U. (2011 b). Reversal of multidrug resistance by small interfering RNA (siRNA) in doxorubicin-resistant MCF-7 breast cancer cells. *Biomedicine & Pharmacotherapy*, 65(2), 85-89.

Dönmez Y. (2010) Reversal of multidrug resistance by small interfering RNAs (sirna) in Doxorubicin resistant MCF-7 breast cancer cells, M.Sc. Thesis, METU, Ankara, Turkey

Drugs.com (2013) Bortezomib Side Effects, Available at: <http://www.drugs.com/sfx/bortezomib-side-effects.html> (Accessed: 22 August 2013)

Du, H., Wolf, J., Schafer, B., Moldoveanu, T., Chipuk, J. E., & Kuwana, T. (2011). BH3 domains other than Bim and Bid can directly activate Bax/Bak. *Journal of Biological Chemistry*, 286(1), 491-501.

Ducry, L., & Stump, B. (2009). Antibody– drug conjugates: linking cytotoxic payloads to monoclonal antibodies. *Bioconjugate Chemistry*, 21(1), 5-13.

El-Sherbiny, I. M., & Smyth, H. D. (2011). Controlled release pulmonary administration of curcumin using swellable biocompatible microparticles. *Molecular Pharmaceutics*, 9(2), 269-280.

Engin, K., Leeper, D. B., Cater, J. R., Thistlethwaite, A. J., Tupchong, L., & McFarlane, J. D. (1995). Extracellular pH distribution in human tumours. *International Journal of Hyperthermia*, 11(2), 211-216.

Estrella, V., Chen, T., Lloyd, M., Wojtkowiak, J., Cornell, H.H., Hashim, A.I., Bailey, K., Balagurunatham, Y., Rothberg, J.M., Sloane, B.F., Johnson, J., Gatenby, R.A., Gillies, R.J. (2013). Acidity Generated by the Tumor Microenvironment Drives Local Invasion. *Cancer Res*; 73:1524-1535

Fernandes, J. V., de Vasconcellos Meissner, R., de Carvalho, M. G. F., de Medeiros Fernandes, T. A. A., de Azevedo, P. R. M., & Villa, L. L. (2009). Prevalence of HPV infection by cervical cytologic status in Brazil. *International Journal of Gynecology & Obstetrics*, 105(1), 21-24.

Fernandes, J. V., Fernandes T. A. A. M. (2012). Human Papillomavirus: Biology and Pathogenesis, Human Papillomavirus and Related Diseases - From Bench to Bedside - A Clinical Perspective, Dr. Davy Vanden Broeck (Ed.), ISBN: 978-953-307-860-1, InTech.

Fernández-Urrusuno, R., Calvo, P., Remuñán-López, C., Vila-Jato, J. L., & Alonso, M. J. (1999). Enhancement of nasal absorption of insulin using chitosan nanoparticles. *Pharmaceutical research*, 16(10), 1576-1581.

Ferrari, M. (2005). Cancer nanotechnology: opportunities and challenges. *Nature Reviews Cancer*, 5(3), 161-171.

Fonte, P., Andrade, F., Araujo, F., Andrade, C., Neves, J., & Sarmiento, B. (2012). Chitosan-coated solid lipid nanoparticles for insulin delivery. *Methods in Enzymology*, 508, 295-314.

Frazer, I. H. (2004). Prevention of cervical cancer through papillomavirus vaccination. *Nat Rev Immunol*; 4: 46-54.

Füssel, F. (1997). Dissertation, Aachen: Rheinisch-Westfälische Technische Hochschule Aachen.

Gao, F., Pan, B. F., Zheng, W. M., Ao, L. M., & Gu, H. C. (2005). Study of streptavidin coated onto PAMAM dendrimer modified magnetite nanoparticles. *Journal of Magnetism and Magnetic materials*, 293(1), 48-54.

Gaur, U., Sahoo, S. K., De, T. K., Ghosh, P. C., Maitra, A., & Ghosh, P. K. (2000). Biodistribution of fluoresceinated dextran using novel nanoparticles evading reticuloendothelial system. *International journal of pharmaceutics*, 202(1), 1-10.

Ge, Y., Zhang, Y., He, S., Nie, F., Teng, G., & Gu, N. (2009). Fluorescence modified chitosan-coated magnetic nanoparticles for high-efficient cellular imaging. *Nanoscale research letters*, 4(4), 287-295.

Gillies, E. R., & Fréchet, J. M. (2005). pH-responsive copolymer assemblies for controlled release of Doxorubicin. *Bioconj Chem* 16: 361-368.

Gonçalves, C., Torrado, E., Martins, T., Pereira, P., Pedrosa, J., & Gama, M. (2010). Dextrin nanoparticles: Studies on the interaction with murine macrophages and blood clearance. *Colloids and Surfaces B: Biointerfaces*, 75(2), 483-489.

Gottesman, M. M., Fojo, T., & Bates, S. E. (2002). Multidrug resistance in cancer: role of ATP-dependent transporters. *Nature Reviews Cancer*, 2(1), 48-58.

Goya, G.F., Grazu, V., & Ibarra, M. R. (2008). Magnetic nanoparticles for cancer therapy. *Current Nanoscience*, 4 1-16.

Green, J. A., Kirwan, J. M., Tierney, J. F., Symonds, P., Fresco, L., Collingwood, M., & Williams, C. J. (2001). Survival and recurrence after concomitant chemotherapy and radiotherapy for cancer of the uterine cervix: a systematic review and meta-analysis. *The Lancet*, 358(9284), 781-786.

Grenha, A. (2012). Chitosan nanoparticles: a survey of preparation methods. *J. Drug Target.*, 20, 291–300.

Gupta, A. K., & Gupta, M. (2005). Synthesis and surface engineering of iron oxide nanoparticles for biomedical applications. *Biomaterials* 26:3995–4021.

Gupta, A. K., Naregalkar, R. R., Vaidya, V.D., Gupta, M. (2007). Recent advances on surface engineering of magnetic iron oxide nanoparticles and their biomedical applications. *Nanomedicine* 2:23–39.

Haik, Y., Pai, V., & Chen, C. J. (2001). Apparent viscosity of human blood in a high static magnetic field. *J. Magn. Magn. Mater.*, 225: 180-186.

Harris, R.A., Yang, A., Stein, R.C., Lucy, K., Brusten, L., Herath, A., Parekh, R., Waterfield, M.D., O'Hare, M.J., Neville, M.A., Page, M.J., & Zvelebil, M.J. (2002) Cluster analysis of an extensive human breast cancer cell line protein expression map database. *Proteomics* 2, 212-223.

Harush-Frenkel, O., Debotton, N., Benita, S., & Altschuler, Y. (2007). Targeting of nanoparticles to the clathrin-mediated endocytic pathway. *Biochemical and biophysical research communications*, 353(1), 26-32.

Hathout, Y., Riordan, K., Gehrman, M., & Fenselau, C. (2002). Differential protein expression in the cytosol fraction of an MCF-7 breast cancer cell line selected for resistance toward melphalan. *Journal of proteome research*, 1(5), 435-442.

zur Hausen, H. (2009). Papillomaviruses in the causation of human cancers—a brief historical account. *Virology*, 384(2), 260-265.

Hebner, C. M., & Laimins, L. A. (2006). Human papillomaviruses: basic mechanisms of pathogenesis and oncogenicity. *Reviews in medical virology*, 16(2), 83-97.

Hermanson, G. (1996). *Bioconjugate techniques*, Academic Press, San Diego.

Hougardy, B. M. T., & Maduro, J. H. (2005). Clinical potential of inhibitors of survival pathways and activators of apoptotic pathways in treatment of cervical cancer: changing the apoptotic balance. *Lancet Oncol*; 6: 589–98.

Hritcu, D., Popa, M. I., Popa, N., Badescu, V., & Balan, V. (2009). Preparation and characterization of magnetic chitosan nanospheres. *Turk J Chem*, 33, 785-796.

- Hu, M., Li, Y., Decker, E. A., Xiao, H., & McClements, D. J. (2009). Influence of tripolyphosphate cross-linking on the physical stability and lipase digestibility of chitosan-coated lipid droplets. *Journal of Agricultural and Food Chemistry*, 58(2), 1283-1289.
- Huang, M., Ma, Z., Khor, E., & Lim, L. Y. (2002). Uptake of FITC-chitosan nanoparticles by A549 cells. *Pharmaceutical research*, 19(10), 1488-1494.
- Meijer, E. W., Jansen, J. F. G. A., & De Brabander-van den Berg, E. M. M. (1994). Encapsulation of guest molecules into a dendritic box. *Science*, 266, 1226-1229.
- Jemal, A., Siegel, R., Xu, J., & Ward, E. (2010). *Cancer statistics, 2010*. CA: a cancer journal for clinicians, 60(5), 277-300.
- Jiang, X., Musyanovych, A., Röcker, C., Landfester, K., Mailänder, V., & Nienhaus, G. U. (2011). Specific effects of surface carboxyl groups on anionic polystyrene particles in their interactions with mesenchymal stem cells. *Nanoscale*, 3(5), 2028-2035.
- Kalantari, M., Calleja-Macias, I. E., Tewari, D., Hagmar, B., Lie, K., Barrera-Saldana, H. A., Wiley, DJ, & Bernard, H. U. (2004). Conserved methylation patterns of human papillomavirus type 16 DNA in asymptomatic infection and cervical neoplasia. *Journal of virology*, 78(23), 12762-12772.
- Kamer, S., Ren, Q., & Dicker, AP. (2009). Differential radiation sensitization of human cervical cancer cell lines by the proteasome inhibitor velcade (bortezomib, PS-341) *Arch Gynecol Obstet.*, 279(1):41-6
- Kane, R. C., Bross, P. F., Farrell, A. T., & Pazdur, R. (2003). Velcade®: US FDA approval for the treatment of multiple myeloma progressing on prior therapy. *The oncologist*, 8(6), 508-513.
- Kane, R. C., Dagher, R., Farrell, A., Ko, C. W., Sridhara, R., Justice, R., & Pazdur, R. (2007). Bortezomib for the treatment of mantle cell lymphoma. *Clinical Cancer Research*, 13(18), 5291-5294.
- Kangarlu, A., & Robitaille, P. M. L. (2000). Biological effects and health implications in magnetic resonance imaging. *Concept Magnetic Res*, 12: 321-359.
- Kars, M. D., İşeri, Ö. D., Gündüz, U., Ural, A. U., Arpacı, F., & Molnar, J. (2006). Development of rational in vitro models for drug resistance in breast cancer and modulation of MDR by selected compounds. *Anticancer research*, 26(6B), 4559-4568.
- Kavaz, D., Odabaş, S., Güven, E., Demirbilek, M., & Denkbaş, E. B. (2010). Bleomycin loaded magnetic chitosan nanoparticles as multifunctional nanocarriers. *Journal of Bioactive and compatible polymers*, 25(3), 305-318.

Keskin, T. (2012). Preparation of Polyethylene Glycol Coated Magnetic Nanoparticles for Targeting of Cancer Cells, MSc Thesis, Middle East Technical University, Turkey.

Khodadust, R., Unsoy, G., Yalcin, S., Gunduz, G., & Gunduz, U. (2013). PAMAM Dendrimer Coated Iron Oxide Nanoparticles: Synthesis and Characterization of Different Generations. *J Nanopart Res* 15:1488-1501.

Kim, Y., Dalhaimer, P., Christian, D. A., & Discher, D. E. (2005). Polymeric worm micelles as nano-carriers for drug delivery. *Nanotechnology*, 16(7), S484.

Kirpotin, D. B., Drummond, D. C., Shao, Y., Shalaby, M. R., Hong, K., Nielsen, U. B., Marks, J. D., Benz, C. C., & Park, J. W. (2006). Antibody targeting of long-circulating lipidic nanoparticles does not increase tumor localization but does increase internalization in animal models. *Cancer Research*, 66(13), 6732-6740.

Kjaer, A. (2006). Molecular imaging of cancer using PET and SPECT. In *New trends in Cancer for the 21st century* (pp. 277-284). Springer Netherlands.

Kocic, B., Filipovic, S., Petrovic, B., Mijalkovic, D., Rancic, N., & Poultsidi, A. (2010). Clinical and biological characteristics of breast cancer. *Journal of BUON., Official Journal of the Balkan Union of Oncology*, 15(4), 660-667.

Kostarelos, K., Lacerda, L., Pastorin, G., Wu, W., Wieckowski, S., Luangsivilay, J., Godefroy, S., Pantarotto, D., Briand, J. P., Muller, S., Prato, M., & Bianco, A. (2007). Cellular uptake of functionalized carbon nanotubes is independent of functional group and cell type. *Nature Nanotechnology*, 2(2), 108-113.

Kremer, L. C., & Caron, H. N. (2004). Anthracycline cardiotoxicity in children. *The New England Journal of Medicine*, 351(2), 120-121.

Kuerer, H. M., Newman, L. A., Smith, T. L., Ames, F. C., Hunt, K. K., Dhingra, K., Theriault, R. L., Singh, G., Binkley, S. M., Sneige, N., Buchholz, T. A., Ross, M. I., McNeese, M. D., Buzdar, A. U., Hortobagyi, G. N., & Singletary, S.E. (1999). Clinical course of breast cancer patients with complete pathologic primary tumor and axillary lymph node response to Doxorubicin-based neoadjuvant chemotherapy. *J Clin Oncol*, 17: 460-469.

Kuo, S.R., Liu, J.S., Broker, T.R., & Chow, L.T. (1994). Cell-free replication of the human papillomavirus DNA with homologous viral E1 and E2 proteins and human cell extracts. *J. Biol. Chem.*, 269, 24058.

Kvansakul, M., Yang, H., Fairlie, W.D., Czabotar, P.E., Fischer, S.F., Perugini, M.A., Huang, D.C., and Colman, P.M. (2008). Vaccinia virus anti-apoptotic F1L is a novel Bcl-2-like domain-swapped dimer that binds a highly selective subset of BH3-containing death ligands. *Cell Death Differ.*, 15, 1564-1571.

- Kwok, T. T., Mok, C. H., & Menton-Brennan L. (1994). Up-regulation of a mutant form of p53 by Doxorubicin in human squamous carcinoma cells. *Cancer Res.*, Jun 1;54(11):2834-6.
- Labhasetwar, V., Song, C., Humphrey, W., Shebuski, R., & Levy, R. J. (1998). Arterial uptake of biodegradable nanoparticles: effect of surface modifications. *Journal of Pharmaceutical Sciences*, 87(10), 1229-1234.
- Lagaru, A., Chen, X.Y. & Gambhir, S.S. (2007). Molecular imaging can accelerate anti-angiogenic drug development and testing. *Nature Clinical Practice Oncology*, 4, 556-557.
- Laurent, S., Bridot, J. L., Elst, L. V., & Muller, R. N. (2010). Magnetic iron oxide nanoparticles for biomedical applications. *Future medicinal chemistry*, 2(3), 427-449.
- Lee, H. S., Hee Kim, E., Shao, H., & Kook Kwak, B. (2005). Synthesis of SPIO-chitosan microspheres for MRI-detectable embolotherapy. *Journal of Magnetism and Magnetic Materials*, 293(1), 102-105.
- Lee, J. Y., Choi, Y. S., Suh, J. S., Kwon, Y. M., Yang, V. C., Lee, S. J., , Chung, C. P. & Park, Y. J. (2011). Cell-penetrating chitosan/doxorubicin/TAT conjugates for efficient cancer therapy. *International Journal of Cancer*, 128(10), 2470-2480.
- Lee, S. T., Mi, F. L., Shen, Y. J., & Shyu, S. S. (2001). Equilibrium and kinetic studies of copper (II) ion uptake by chitosan-tripolyphosphate chelating resin. *Polymer*, 42(5), 1879-1892.
- Lehr CM.; Bouwstra JA.; Schacht EH.; Junginger HE. (1992) In vitro evaluation of mucoadhesive properties of chitosan and some other natural polymers. *Int. J. Pharm.*, 78, 43-48.
- Lenz, H. J. (2003). Clinical update: proteasome inhibitors in solid tumors. *Cancer Treat. Rev.*, 29 (Suppl. 1):41-48.
- Leroueil, P. R., Berry, S. A., Duthie, K., Han, G., Rotello, V. M., McNerny, D. Q., Baker, J. R., Orr, B. G., & Banaszak Holl, M. M. (2008). Wide varieties of cationic nanoparticles induce defects in supported lipid bilayers. *Nano Letters*, 8(2), 420-424.
- Leroueil, P. R., Hong, S., Mecke, A., Baker Jr, J. R., Orr, B. G., & Banaszak Holl, M. M. (2007). Nanoparticle interaction with biological membranes: does nanotechnology present a Janus face?. *Accounts of chemical research*, 40(5), 335-342.
- Leung, L. K., & Wang, T. T. (1999). Differential effects of chemotherapeutic agents on the Bcl-2/Bax apoptosis pathway in human breast cancer cell line MCF-7. *Breast Cancer Res Treat*; 55: 73-83.

- Li, G. Y., Jiang, Y. R., Huang, K. L., Ding, P., & Chen, J. (2008). Preparation and properties of magnetic Fe₃O₄-chitosan nanoparticles. *Journal of Alloys and Compounds*, 466(1), 451-456.
- Li, M. C., Liu, C., Xin, M. H., Zhao, H., Wang, M., Feng, Z., & Sun, X. L. (2005). Preparation and characterization of acylated chitosan. *Chem Res Chinese U*, 21(1), 114-116.
- Li, K. C., Pandit, S. D., Guccione, S., & Bednarski, M. D. (2004). Molecular imaging applications in nanomedicine. *Biomedical Microdevices*, 6(2), 113-116.
- Lim, E. K., Huh, Y. M., Yang, J., Lee, K., Suh, J. S., & Haam, S. (2011). pH-Triggered Drug-Releasing Magnetic Nanoparticles for Cancer Therapy Guided by Molecular Imaging by MRI. *Advanced Materials*, 23(21), 2436-2442.
- Lin, J., Zhang, H., Chen, Z., & Zheng, Y. (2010). Penetration of lipid membranes by gold nanoparticles: insights into cellular uptake, cytotoxicity, and their relationship. *ACS Nano*, 4(9), 5421-5429.
- Lipshultz, S. E. (2006). Exposure to anthracyclines during childhood causes cardiac injury. *Semin Oncol*; S: 04-019.
- Liu, R., Zhao, Y., Huang, R., Zhao, Y., & Zhou, H. (2010). Shape evolution and tunable properties of monodisperse magnetite crystals synthesized by a facile surfactant-free hydrothermal method. *Eur J Inorg Chem*, (28):4499-4505.
- Liu, S., Wei, X., Chu, M., Peng, J., & Xu, Y. (2006). Synthesis and characterization of iron oxide/polymer composite nanoparticles with pendent functional groups. *Colloids and Surfaces B: Biointerfaces*, 51(2), 101-106.
- Liu, X., Chen, Y., Li, H., Huang, N., Jin, Q., Ren, K., & Ji, J. (2013). Enhance Retention and Cellular Uptake of Nanoparticles in Tumor by Controlling Their Aggregation Behavior. *ACS Nano*, 7 (7), pp 6244-6257.
- Longhi, A., Ferrari, S., Bacci, G., & Specchia, S. (2007). Long-term follow-up of patients with doxorubicin-induced cardiac toxicity after chemotherapy for osteosarcoma. *Anticancer Drugs*, 18: 737-744.
- Lu, G., Kong, L., Sheng, B., Wang, G., Gong, Y., & Zhang, X. (2007). Degradation of covalently cross-linked carboxymethyl chitosan and its potential application for peripheral nerve regeneration. *European Polymer Journal*, 43(9), 3807-3818.
- Lü, S., & Wang, J. (2013). The resistance mechanisms of proteasome inhibitor bortezomib. *Biomarker Research*, 1(1), 13.

- Lunov, O., Syrovets, T., Röcker, C., Tron, K., Ulrich Nienhaus, G., Rasche, V., Mailander, V., Landfester, K., & Simmet, T. (2010). Lysosomal degradation of the carboxydextran shell of coated superparamagnetic iron oxide nanoparticles and the fate of professional phagocytes. *Biomaterials*, 31(34), 9015-9022.
- Ma, W., Ya, F., Han, M., & Wang, R. (2007). Characteristics of equilibrium, kinetics studies for adsorption of fluoride on magnetic-chitosan particle. *J Hazard Mater*, 143:296–302.
- Macaroff, P. P., Simioni, A. R., Lacava, Z. G., Lima, E. C., Morais, P. C., & Tedesco, A. C. (2006). Studies of cell toxicity and binding of magnetic nanoparticles with blood stream macromolecules. *Journal of Applied Physics*, 99(8), 08S102-08, p102.
- Maduro, J. H., Pras, E., Willemsse, P. H. B., & De Vries, E. G. E. (2003). Acute and long-term toxicity following radiotherapy alone or in combination with chemotherapy for locally advanced cervical cancer. *Cancer Treatment Reviews*, 29(6), 471-488.
- Maeda, H. (2001). The enhanced permeability and retention (EPR) effect in tumor vasculature: the key role of tumor-selective macromolecular drug targeting. *Adv Enzyme Regul.*, 41: 189-207.
- Maeda, H. (2010). Tumor-selective delivery of macromolecular drugs via the EPR effect: background and future prospects. *Bioconjug Chem*. 19;21(5):797-802.
- Maeda, H., Wu, J., Sawa, T., & Matsumura, Y. (2000). Tumor vascular permeability and the EPR effect in macromolecular therapeutics: a review, *J. of Controlled Release* 65 271–284.
- Mamot, C., Drummond, D. C., Noble, C. O., Kallab, V., Guo, Z., Hong, K., Kirpotin, D. B., & Park, J. W. (2005). Epidermal growth factor receptor-targeted immunoliposomes significantly enhance the efficacy of multiple anticancer drugs in vivo. *Cancer Research*, 65(24), 11631-11638.
- Martell, A. E., & Smith, R. M. (2004). NIST critically selected stability constants of metal complexes database. NIST standard reference database 46 version 8.0. Gaithersburg, MD: US Department of Commerce, National Institute of Standards and Technology.
- Martinou, J. C., & Youle, R. J. (2011). Mitochondria in apoptosis: Bcl-2 family members and mitochondrial dynamics. *Developmental Cell*, 21(1), 92-101.
- Matsumura, Y., Maeda, H. (1986). A new concept for macromolecular therapeutics in cancer chemotherapy: mechanism of tumoritropic accumulation of proteins and the antitumor agent smancs. *Cancer Research* 46 (12 Pt 1): 6387–92.
- Maya-Mendoza, A., Tang, C. W., Pombo, A., & Jackson, D. A. (2009). Mechanisms regulating S phase progression in mammalian cells. *Front Biosci*, 14: 419.

McBain, S. C., Yiu, H. H., & Dobson, J. (2008). Magnetic nanoparticles for gene and drug delivery. *International Journal of Nanomedicine*, 3(2), 169-180.

Meissner, J. D. (1999). Nucleotide sequences and further characterization of human papillomavirus DNA present in the CaSki, SiHa and HeLa cervical carcinoma cell lines *Journal of General Virology*, 80, 1725–1733.

Mellman, I., Fuchs, R., & Helenius, A. (1986). Acidification of the endocytic and exocytic pathways. *Annu Rev Biochem.*, 55:773–800.

Moghimi, S. M., (2005) Nanomedicine: current status and future prospects. *FASEB J.*, 19, 311.

Moreno, D., Zalba, S., Navarro, I., Tros de Ilarduya, C., & Garrido, M. J. (2010). Pharmacodynamics of cisplatin-loaded PLGA nanoparticles administered to tumor-bearing mice. *European Journal of Pharmaceutics and Biopharmaceutics*, 74(2), 265-274.

Muraoka, S., Miura, T. (2004). Thiol oxidation induced by oxidative action of adriamycin. *Free Radic Res.*, 38(9): 963-8.

National Institute of Health (2012) Targeted therapies for breast cancer tutorial, Available at: http://www.cancer.gov/cancertopics/understandingcancer/targetedtherapies/breastcancer_htmlcourse (Accessed: 22 August 2013)

Nativo, P., Prior, I. A., & Brust, M. (2008). Uptake and intracellular fate of surface-modified gold nanoparticles. *ACS Nano*, 2, 1639–1644.

Neuberger, T., Schöpf, B., Hofmann, H., Hofmann, M., & Von Rechenberg, B. (2005). Superparamagnetic nanoparticles for biomedical applications: Possibilities and limitations of a new drug delivery system. *J. Magn. Magn. Mater.*, 293:483–496.

Ojugo, A. S., McSheehy, P. M., McIntyre, D. J., McCoy, C., Stubbs, M., Leach, M. O., Judson, I. R., & Griffiths, J. R. (1999). Measurement of the extracellular pH of solid tumours in mice by magnetic resonance spectroscopy: a comparison of exogenous ¹⁹F and ³¹P probes. *NMR in Biomedicine*, 12(8), 495-504.

Paama, L., Pitkänen, I., Halttunen, H., & Perämäki, P. (2003). Infrared evolved gas analysis during thermal investigation of lanthanum, europium and samarium carbonates. *Thermochimica Acta*, 403(2), 197-206.

Pajeva, I., Todorov, D. K., Seydel, J. (2004). Membrane effects of the antitumor drugs Doxorubicin and thaliblastine: comparison to multidrug resistance modulators verapamil and trans-flupentixol. *Eur J Pharm Sci.*, 21(2-3): 243-50.

- Pan, Y., Neuss, S., Leifert, A., Fischler, M., Wen, F., Simon, U., Schmid, G., Brandau, W., & Jahnen-Dechent, W. (2007). Size-Dependent Cytotoxicity of Gold Nanoparticles. *Small*, 3(11), 1941-1949.
- Paramore, A., & Frantz, S., (2003) Fresh From The Pipeline: Bortezomib, *Nature Reviews Drug Discovery*, 2, 611-612 (August).
- Park, J. S., Han, T. H., Lee, K. Y., Han, S. S., Hwang, J. J., Moon, D. H., Kim, S. Y., & Cho, Y. W. (2006). N-acetyl histidine-conjugated glycol chitosan self-assembled nanoparticles for intracytoplasmic delivery of drugs: Endocytosis, exocytosis and drug release. *Journal of Controlled Release*, 115(1), 37-45.
- Park, Y., Kang, E., Kwon, O. J., Park, H. K., Kim, J. H., & Yun, C. O. (2010). Tumor targeted adenovirus nanocomplex ionically crosslinked by chitosan. *Journal of Controlled Release*, 148(1), e124.
- Pati, F., Adhikari, B., Dhara, S. (2011). Development of chitosan-tripolyphosphate fibers through pH dependent ionotropic gelation. *Carbohydr Res.*, 29;346(16):2582-8.
- Paul, D., & Cowan, K.H. (1999). Drug resistance in breast cancer. In: *Breast Cancer Molecular Genetics, Pathogenesis and Therapeutics*. Ed. Bowcock AM. Totowa: Humana Press. p481-517.
- Peng, Z.G. Hidajat, K., & Uddin, M. S. (2004). Adsorption of bovine serum albumin on nanosized magnetic particles. *Journal of Colloid and Interface Science*, 271 277–283.
- Pieróg, M., Gierszewska-Drużyńska, M., & Ostrowska-Czubenko, J. (2009). Effect of ionic crosslinking agents on swelling behavior of chitosan hydrogel membranes. *Jaworska MM (ed), Progress on Chemistry and Application of Chitin and its Derivatives. Vol. XIV, Polish Chitin Society, Łódź 2009, 75-82.*
- Pison, U., Welte, T., Giersig, M., & Groneberg, D. A. (2006). Nanomedicine for respiratory diseases. *European Journal of Pharmacology*, 533(1), 341-350.
- Portero, A., Remuñán-López, C., & Nielsen, H. M. (2002). The potential of chitosan in enhancing peptide and protein absorption across the TR146 cell culture model-an in vitro model of the buccal epithelium. *Pharmaceutical Research*, 19(2), 169-174.
- Prego, C., Garcia, M., Torres, D., & Alonso, M. J. (2005). Transmucosal macromolecular drug delivery. *Journal of Controlled Release*, 101(1), 151-162.
- Pritchard, J. E., Dillon, P. M., Conaway, M. R., Silva, C. M., & Parsons, S. J. (2012). A mechanistic study of the effect of doxorubicin/adriamycin on the estrogen response in a breast cancer model. *Oncology*, 83(6), 305-320.

- Rahbari, R., Sheahan, T., Modes, V., Collier, P., Macfarlane, C., & Badge, R. M. (2009). A novel L1 retrotransposon marker for HeLa cell line identification. *BioTechniques*, 46(4), 277.
- Ravi Kumar, M. N. (2000). A review of chitin and chitosan applications. *Reactive and Functional Polymers*, 46(1), 1-27.
- Rejman, J., Oberle, V., Zuhorn, I., & Hoekstra, D. (2004). Size-dependent internalization of particles via the pathways of clathrin- and caveolae-mediated endocytosis. *Biochem. J.*, 377, 159-169.
- Rinaudo, M. (2008). Main properties and current applications of some polysaccharides as biomaterials. *Polym. Int.*, 57, 397-430.
- Rinehart-Kim, J., Johnston, M., Birrer, M., Bos, T., (2000). Alterations in the gene expression profile of MCF-7 breast tumor cells in response to c-Jun. *Int. J. Cancer*, 88, 180-190.
- Robert, J., & Larsen, A. K. (1998). Drug resistance to topoisomerase II inhibitors. *Biochimie.*, 80: 247-254.
- Rodrigues, S., Dionísio, M., López, C. R., & Grenha, A. (2012). Biocompatibility of chitosan carriers with application in drug delivery. *Journal of Functional Biomaterials*, 3(3), 615-641.
- Roiter, Y., Ornatska, M., Rammohan, A. R., Balakrishnan, J., Heine, D. R., & Minko, S. (2008). Interaction of nanoparticles with lipid membrane. *Nano Letters*, 8(3), 941-944.
- Rumpold, H., Salvador, C., Wolf, A. M., Tilg, H., Gastl, G., & Wolf, D. (2007). Knockdown of P-gP resensitizes leukemic cells to proteasome inhibitors. *Biochemical and biophysical research communications*, 361(2), 549-554.
- Sahu, S. K., Mallick, S. K., Santra, S., Maiti, T. K., Ghosh, S. K., & Pramanik, P. (2010). In vitro evaluation of folic acid modified carboxymethyl chitosan nanoparticles loaded with doxorubicin for targeted delivery. *Journal of Materials Science: Materials in Medicine*, 21(5), 1587-1597.
- Sannan, T., Kurita, K., & Iwakura, Y. (1976). Studies on chitin, 2. Effect of deacetylation on solubility. *Die Makromolekulare Chemie*, 177(12), 3589-3600.
- Schenck, J. F. (2005). Physical interactions of static magnetic fields with living tissues. *Progress in Biophysics and Molecular Biology*, 87(2), 185-204.
- Scherer, W. F., Syverton, J. T., & Gey, G. O. (1953). Studies on the propagation in vitro of poliomyelitis viruses IV. Viral multiplication in a stable strain of human malignant epithelial

cells (strain HeLa) derived from an epidermoid carcinoma of the cervix. *The Journal of Experimental Medicine*, 97(5), 695-710.

Shackelford, J., & Pagano, J. S. (2004). Tumor viruses and cell signaling pathways: deubiquitination versus ubiquitination. *Molecular and Cellular Biology*, 24(12), 5089-5093.

Shi, Y., Moon, M., Dawood, S., & McManus, B. (2011). Mechanisms and management of doxorubicin cardiotoxicity. *Herz*, 36(4), 296-305.

Shu, X. Z., & Zhu, K. J. (2002). The influence of multivalent phosphate structure on the properties of ionically cross-linked chitosan films for controlled drug release. *European Journal of Pharmaceutics and Biopharmaceutics*, 54(2), 235-243.

Shubayev, V. I., Pisanic II, T. R., & Jin, S. (2009). Magnetic nanoparticles for theragnostics. *Advanced Drug Delivery Reviews*, 61(6), 467-477.

Singh, D. K., & Ray, A. R. (2000). Biomedical applications of chitin, chitosan, and their derivatives. *Journal of Macromolecular Science, Part C: Polymer Reviews*, 40(1), 69-83.

Smith, A. J., Dai, H., Correia, C., Takahashi, R., Lee, S. H., Schmitz, I., & Kaufmann, S. H. (2011). Noxa/Bcl-2 protein interactions contribute to bortezomib resistance in human lymphoid cells. *Journal of Biological Chemistry*, 286(20), 17682-17692.

Sorensen, K., Levitt, G. A., Bull, C., Dorup, I., & Sullivan, I. D. (2003). Late anthracycline cardiotoxicity after childhood cancer. *Cancer*, 97(8), 1991-1998.

Souhami, R., & Tobias, J. (2005). Bone and Soft-Tissue Sarcomas. *Cancer and its Management, Fifth Edition*, 386-404.

Strebhardt, K., & Ullrich, A. (2008). Paul Ehrlich's magic bullet concept: 100 years of progress. *Nature Reviews Cancer*, 8(6), 473-480.

Strober, W. (2001). Trypan blue exclusion test of cell viability. *Current protocols in immunology*, Appendix 3B.

Sun, C., Lee, J. S., & Zhang, M. (2008). Magnetic nanoparticles in MR imaging and drug delivery. *Advanced Drug Delivery Reviews*, 60(11), 1252-1265.

Sun, X., Rossin, R., Turner, J. L., Becker, M. L., Joralemon, M. J., Welch, M. J., & Wooley, K. L. (2005). An assessment of the effects of shell cross-linked nanoparticle size, core composition, and surface PEGylation on in vivo biodistribution. *Biomacromolecules*, 6(5), 2541-2554.

Sunwoo, J. B., Chen, Z., Dong, G., Yeh, N., Bancroft, C. C., Sausville, E., Adams, J., Elliott, J., & Van Waes, C. (2001). Novel proteasome inhibitor PS-341 inhibits activation of nuclear

factor- κ B, cell survival, tumor growth, and angiogenesis in squamous cell carcinoma. *Clinical Cancer Research*, 7(5), 1419-1428.

Tan, M. L., Choong, P. F., & Dass, C. R. (2009). Review: doxorubicin delivery systems based on chitosan for cancer therapy. *Journal of Pharmacy and Pharmacology*, 61(2), 131-142.

Teixeira, C., Reed, J. C., & Pratt, M. C. (1995). Estrogen promotes chemotherapeutic drug resistance by a mechanism involving Bcl-2 proto-oncogene expression in human breast cancer cells. *Cancer Research*, 55(17), 3902-3907.

Teng, X., Black, D., Watkins, N. J., Gao, Y., & Yang, H. (2003). Platinum-maghemite core-shell nanoparticles using a sequential synthesis. *Nano Letters*, 3(2), 261-264.

Tiyaboonchai, W., & Limpeanchob, N. (2007). Formulation and characterization of amphotericin B-chitosan-dextran sulfate nanoparticles. *International Journal of Pharmaceutics*, 329(1), 142-149.

Treuel, L., Jiang, X., & Nienhaus, G. U. (2013). New views on cellular uptake and trafficking of manufactured nanoparticles. *Journal of The Royal Society Interface*, 10(82).

Unsoy, G., Yalcin, S., Khodadust, R., Gunduz, G., & Gunduz, U. (2012). Synthesis optimization and characterization of chitosan-coated iron oxide nanoparticles produced for biomedical applications. *Journal of Nanoparticle Research*, 14(964), 1-13.

van Sluis, R., Bhujwala, Z. M., Raghunand, N., Ballesteros, P., Alvarez, J., Cerdan, S., Galons, J. P., & Gillies, R. J. (1999). In vivo imaging of extracellular pH using ^1H MRSI. *Magnetic Resonance in Medicine*, 41(4), 743-750.

Varadan, V. K., Chen, L., & Xie, J. (2008). *Nanomedicine: design and applications of magnetic nanomaterials, nanosensors and nanosystems*. Wiley.com., ISBN 978-0-470-03351-7.

Vercoutter-Edouart, A. S., Lemoine, J., Le Bourhis, X., Louis, H., Boilly, B., Nurcombe, V., Révillion, F., Peyrat, j. P., & Hondermarck, H. (2001). Proteomic analysis reveals that 14-3-3 σ is down-regulated in human breast cancer cells. *Cancer Research*, 61(1), 76-80.

Verma, A., Uzun, O., Hu, Y., Hu, Y., Han, H. S., Watson, N., Chen, S., Irvine, D. J., & Stellacci, F. (2008). Surface-structure-regulated cell-membrane penetration by monolayer-protected nanoparticles. *Nature Materials*, 7(7), 588-595.

Vila A.; Sánchez A.; Janes K.; Behrens I.; Kissel T.; Jato JLV.; Alonso MJ. (2004) Low molecular weight chitosan nanoparticles as new carriers for nasal vaccine delivery in mice. *Eur. J. Pharm. Biopharm.*, 57, 123–131.

- Voorhees, P. M., Dees, E. C., O'Neil, B., & Orlowski, R. Z. (2003). The proteasome as a target for cancer therapy. *Clinical Cancer Research*, 9(17), 6316-6325.
- Walker, P.R., Smith, C., Youndale, T., Leblanc, J., Whitfield, J.F., & Sikorska, M. (1991). Topoisomerase II-reactive chemotherapeutic drugs induce apoptosis in thymocytes. *Cancer Res*, 51, 1078–1085.
- Wan, Y., Creber, K. A., Peppley, B., & Bui, V. T. (2003). Synthesis, characterization and ionic conductive properties of phosphorylated chitosan membranes. *Macromolecular Chemistry and Physics*, 204(5-6), 850-858.
- Wang, T., Bai, J., Jiang, X., & Nienhaus, G. U. (2012). Cellular uptake of nanoparticles by membrane penetration: a study combining confocal microscopy with FTIR spectroelectrochemistry. *ACS Nano* 6, 1251–1259.
- Wang, Y., Li, B., Zhou, Y., & Jia, D. (2009). In situ mineralization of magnetite nanoparticles in chitosan hydrogel. *Nanoscale Research Letters*, 4(9), 1041-1046.
- Wang, Y., Wang, X., Luo, G., & Dai, Y. (2008). Adsorption of bovin serum albumin (BSA) onto the magnetic chitosan nanoparticles prepared by a microemulsion system. *Bioresource Technology*, 99(9), 3881-3884.
- Whiteside, M. A., Siegel, E. M., & Unger, E. R. (2008). Human papillomavirus and molecular considerations for cancer risk. *Cancer*, 113(S10), 2981-2994.
- Wood, J. (2002). Doxorubicin, in *The cytotoxic Handbook, Fourth Edition.*, by M. Allwood, A. Stanley, P. Wright (Radcliffe Medical Press Ltd, Oxon, UK.), pp. 322–329.
- Woodman, C. B., Collins, S. I., & Young, L. S. (2007). The natural history of cervical HPV infection: unresolved issues. *Nature Reviews Cancer*, 7(1), 11-22.
- Wu, Y., Wang, Y., Luo, G., & Dai, Y. (2009). In situ preparation of magnetic Fe₃O₄ chitosan nanoparticles for lipase immobilization by cross-linking and oxidation in aqueous solution. *Bioresource Technology*, 100(14), 3459-3464.
- Yang, P. F., & Lee, C. K. (2007). Hyaluronic acid interaction with chitosan-conjugated magnetite particles and its purification. *Biochemical Engineering Journal*, 33(3), 284-289.
- Ye, X. R., Daraio, C., Wang, C., Talbot, J. B., & Jin, S. (2006). Room temperature solvent-free synthesis of monodisperse magnetite nanocrystals. *Journal of Nanoscience and Nanotechnology*, 6(3), 852-856.
- Yerlikaya, A., Okur, E., & Ulukaya, E. (2012). The p53-independent induction of apoptosis in breast cancer cells in response to proteasome inhibitor bortezomib. *Tumor Biology*, 33(5), 1385-1392.

Yezhelyev, M. V., Gao, X., Xing, Y., Al-Hajj, A., Nie, S., & O'Regan, R. M. (2006). Emerging use of nanoparticles in diagnosis and treatment of breast cancer. *The Lancet Oncology*, 7(8), 657-667.

Yu, J., Patel, S. A., & Dickson, R. M. (2007). In Vitro and Intracellular Production of Peptide-Encapsulated Fluorescent Silver Nanoclusters. *Angewandte Chemie*, 119(12), 2074-2076.

Yuan, Q., Venkatasubramanian, R., Hein, S., & Misra, R. D. K. (2008). A stimulus-responsive magnetic nanoparticle drug carrier: Magnetite encapsulated by chitosan-grafted-copolymer. *Acta Biomaterialia*, 4(4), 1024-1037.

Yuwei, C., & Jianlong, W. (2011). Preparation and characterization of magnetic chitosan nanoparticles and its application for Cu (II) removal. *Chemical Engineering Journal*, 168(1), 286-292.

Zemskova, L. A., Voit, A. V., Nikolenko, Y. M., Sergienko, V. I., Troshkina, I. D., Plevaka, A. V., Maiboroda, S. B., & Chekmarevb, A. M. (2005). Sorption of Rhenium on Carbon Fibrous Materials Modified with Chitosan. *Journal of Nuclear and Radiochemical Sciences*, 6(3), 221-222.

Zhang, L. Y., Zhu, X. J., Sun, H. W., Chi, G. R., Xu, J. X., & Sun, Y. L. (2010). Control synthesis of magnetic Fe₃O₄ chitosan nanoparticles under UV irradiation in aqueous system. *Current Applied Physics*, 10(3), 828-833.

Zhao, H., Chen, C., Zhang, H., Zhou, X., Mei, L., Chen, C., Chen, L., Cao, Z., & Dong, Q. (2012). Is Order the Defining Feature of Magnitude Representation? An ERP Study on Learning Numerical Magnitude and Spatial Order of Artificial Symbols. *PloS One*, 7(11), e49565.

Zhao, Y., Sun, X., Zhang, G., Trewyn, B. G., Slowing, I. I., & Lin, V. S. Y. (2011). Interaction of mesoporous silica nanoparticles with human red blood cell membranes: size and surface effects. *ACS Nano*, 5(2), 1366-1375.

Zheng, Z. M., & Baker, C. C. (2006). Papillomavirus genome structure, expression, and post-transcriptional regulation. *Frontiers in Bioscience: a Journal and Virtual Library*, 11, 2286.

CURRICULUM VITAE

PERSONAL INFORMATION

Surname, Name: Ünsoy (Baydar), Gözde
Nationality: Turkish Republic
Date and Place of Birth: 2nd June 1979, Ankara
Marital Status: Married with one child
Phone: +90 536 612 69 36
e-mail: gozdeunsoy@hotmail.com

EDUCATION

Ph.D.: Middle East Technical University (METU), Biotechnology
M.Sc.: Middle East Technical University (METU), Biotechnology
B.Sc.: Gazi University, Biology
High School: Yükseliş College

FOREIGN LANGUAGES

Advanced English
Intermediate German

PUBLICATIONS

Papers Published in International Journals

1. Unsoy, G., Yalcin, S., Khodadust, R., Gunduz, G., & Gunduz, U. (2012). Synthesis optimization and characterization of chitosan-coated iron oxide nanoparticles produced for biomedical applications. *Journal of Nanoparticle Research*, 14 (964), 1-13.
2. Khodadust, R., Unsoy, G., Yalcin, S., Gunduz, G., & Gunduz, U. (2013). PAMAM dendrimer coated iron oxide nanoparticles: synthesis and characterization of different generations. *Journal of Nanoparticle Research*, 15 (3), 1-13.
3. Khodadust, R., Mutlu, P., Yalcin, S., Unsoy, G., & Gunduz, U. (2013). Doxorubicin loading, release, and stability of polyamidoamine dendrimer-coated magnetic nanoparticles. *Journal of Pharmaceutical Sciences*, 102 (6), 1825–1835.

4. Khodadust, R., Mutlu, P., Yalcin, S., Unsoy, G., & Gunduz, U. (2013). Polyinosinic: polycytidylic acid loading onto different generations of PAMAM dendrimer-coated magnetic nanoparticles. *Journal of Nanoparticle Research*, 15(8), 1-12.
5. Unsoy, G., Khodadust, R., Yalcin, S., Mutlu, P., & Gunduz, U. pH Responsive release of doxorubicin from chitosan coated magnetic nanoparticles for targeted drug delivery. *Journal of Controlled Release*, (Submitted).
6. Unsoy, G., Yalcin, S., Mutlu, P., Khodadust, R., & Gunduz, U. Chitosan magnetic nanoparticles for pH responsive bortezomib release in cancer therapy. *Journal of Controlled Release*, (under revision).
7. Yalcin, S., Unsoy, G., Khodadust, R., Mutlu, P., & Gunduz, U. Poly-hydroxy butyrate (PHB) coated magnetic nanoparticles for doxorubicin release. *International Journal of Nanomedicine*, (Submitted).
8. Yalcin, S., Khodadust, R., Unsoy, G., Garip, I. C., Mumcuoğlu, Z. D., Gündüz, U. Synthesis and characterization of Poly-hydroxybutyrate (PHB) coated magnetic nanoparticles: toxicity analyses on different cell lines. *Synthesis and Reactivity in Inorganic, Metal-Organic, and Nano-Metal Chemistry*, ID LSRT-2013-0374.R1 (Accepted).
9. Keskin, T., Tansik, G., Yakar, A., Unsoy, G., Khodadust, R., & Gunduz, U. (2010) In Vitro Cytotoxic Studies of Polymer Coated Magnetic Nanoparticles for Anti-cancer Drug Delivery. *International Journal of Material Science and Electronics Research (IJMSER)*, 1(2) 45-47.

Full Papers Published in International Conferences

1. Unsoy, G., Yalcin, S., Khodadust, R., Mutlu, P., & Gunduz, U. (2012). In situ synthesis and characterization of chitosan coated iron oxide nanoparticles and loading of doxorubicin. *NANOCON 2012*, October, 23-25, Brno, Czech Republic. EU, PE11.
2. Yalcin, S., Unsoy, G., Khodadust, R., Mutlu, P., Taghavi, N. P., & Gunduz, U. (2012). The cytotoxicity analysis of PHB coated magnetic nanoparticles on sensitive and doxorubicin resistant MCF-7 cell lines. *NANOCON 2012*, October, 23-25, Brno, Czech Republic. EU, PD5.
3. Khodadust, R., Mutlu, P., Yalcin, S., Unsoy, G., Taghavi, N. P., & Gunduz, U. (2012). Loading efficiency and optimization of doxorubicin on dendrimer coated magnetic nanoparticles using different buffers. *NANOCON 2012*, October, 23-25, Brno, Czech Republic. EU, PA72.

Abstracts Published in International Conferences

1. Unsoy, G., Yalcin, S., Khodadust, R., Mutlu, P., & Gunduz, U. (2012). Determination of loading and release efficiencies of doxorubicin by using chitosan coated of magnetic nanoparticles designed for targeted drug delivery. Poster presentation, *Nanomedicine: From Molecules to Diagnosis and Therapy*, October, 1-3, Consiglio Nazionale Delle Ricerche, Rome, Italy, P26.
2. Unsoy, G., Yalcin, S., Khodadust, R., Mutlu, P., & Gunduz, U. (2012). In situ synthesis and characterization of chitosan coated iron oxide nanoparticles. Poster presentation, *Nanocon Conference. 4th International Conference*, October, 23-25, Brno, Czech Republic, EU, p128.
3. Unsoy, G., Khodadust, R., Yalcin, S., Gunduz, G., & Gunduz, U. (2011). Characterization of Etoposide Loaded Magnetic Nanoparticles Prepared for Drug Delivery. Poster presentation, *BIOMED 2011, XVIIth International Symposium on Biomedical Science and Technology*, November, 23-25, Ankara, Turkey, p.P-16.
4. Unsoy, G., Yalcin, S., Khodadust, R., Mutlu, P., Gunduz, G., & Gunduz, U. (2012). Cellular internalization of chitosan coated magnetic nanoparticles by MCF-7 cells. Poster presentation, *ISOPS 10th International Symposium on Pharmaceutical Sciences*, June, 26-29, Ankara, Turkey, P240.
5. Unsoy, G., Gündüz, G., & Gündüz, U. (2011). The cytotoxic analyses of synthesized bare and chitosan coated superparamagnetic nanoparticles for targeted drug delivery. Poster presentation, *EACR, Anticancer Drugs Research Congress*, October, 13-16, Antalya, Turkey, p.115.
6. Khodadust, R., Unsoy, G., Yalcin, S., Mutlu, P., & Gunduz, U. (2012). Synthesis of dendrimeric magnetic nanoparticles and imaging studies using IgG-FITC. Oral presentation, *Nanomedicine: From Molecules to Diagnosis and Therapy*, October, 1-3, Consiglio Nazionale Delle Ricerche, Rome, Italy, SL4.
7. Yalcin, S., Unsoy, G., Mutlu, P., Khodadust, R., & Gunduz, U. (2012). Loading, Release, Stability of Anticancer Drug From in situ Formation PHB Coated Magnetic Nanoparticles. Poster presentation, *Nanomedicine: From Molecules to Diagnosis and Therapy*, October, 1-3, Consiglio Nazionale Delle Ricerche, Rome, Italy, P28.
8. Yalcin, S., Unsoy, G., Mutlu, P., Khodadust, R., & Gunduz, U. (2012). Preparation of antibody-FITC binding dextran coated magnetic nanoparticles for imaging and cancer therapy. Poster presentation, *Nanomedicine: From Molecules to Diagnosis and Therapy*, October, 1-3, Consiglio Nazionale Delle Ricerche, Rome, Italy, P29.
9. Yalcin, S., Unsoy, G., Mutlu, P., Khodadust, R., & Gunduz, U. (2012). The identification of cytotoxicity of various polymers coated magnetic iron oxide nanoparticles in MCF-7 cells. Poster presentation, *Nanomedicine: From Molecules to Diagnosis and Therapy*, October, 1-3, Consiglio Nazionale Delle Ricerche, Rome, Italy, P30.

10. Khodadust, R., Yalcin, S., Unsoy, G., Gunduz, G., & Gunduz, U. (2011). Synthesis and Characterization of Dendrimer Coated Magnetic Nanoparticles for Drug Delivery. Oral presentation, *BIOMED 2011, XVIIth International Symposium on Biomedical Science and Technology*, November, 23-25, Ankara, Turkey, p.O-22.
11. Yalcin, S., Unsoy, G., Khodadust, R., Gunduz, G., & Gunduz, U. (2011). Synthesis and Characterization of Dextran Coated Magnetic Nanoparticles for Anti-Cancer Agent Delivery in Cancer Therapy. Poster presentation, *BIOMED 2011, XVIIth International Symposium on Biomedical Science and Technology*, November, 23-25, Ankara, Turkey, p.P-20.
12. Khodadust, R., Unsoy, G., Yalcin, S., Mutlu, P., Gunduz, G., & Gunduz, U. (2012). Synthesis of IgG Monoclonal Antibody Conjugated Fluorescent Dendrimer Coated Magnetic Nanoparticles for Cancer Therapy. Poster presentation, *ISOPS 10th Internatinal Symposium on Pharmaceutical Sciences*, June, 26-29, Ankara, Turkey, P271.
13. Yalcin, S., Khodadust, R., Unsoy, G., Mutlu, P., Garip, C., & Gunduz, U. (2012). Synthesis and Characterization of Polyhydroxybutyrate (PHB) Coated Magnetic Nanoparticles for Anti-Cancer Agent Delivery in Cancer Therpay. Poster presentation, *ISOPS 10th Internatinal Symposium on Pharmaceutical Sciences*, June, 26-29, Ankara, Turkey, P256.
14. Baydar, G., & Kocabiyik, S. (2005). Biochemical characterization of thermoplasma volcanium recombinant 20S proteasome and its regulatory subunit. Poster presentation, *30th FEBS Congress and 9th IUBMB Conference*, The FEBS Journal, B4-007P, July, 2-7, Budapest, Hungary, p.176.
15. Kocabiyik, S., Demirok, B., & Baydar, G. (2006). Programmed proteolytic machinerics of Thermoplasma volcanium. Oral presentation, *20th IUBMB International Congress of Biochemistry and Molecular Biology*, June, 18-23 Kyoto , Japan", (2006), p.696.

Abstracts Published in National Conferences

1. Baydar, G., Kocabıyık, S., & Özdemir, İ., (2004). Recombinant 20S Proteasome of *Thermoplasma volcanium* and its Regulation. Sözlü sunum, *31th Türk Mikrobiyoloji Kongresi*, September, 19-23, Kuşadası, Aydın, Turkey, p.252.
2. Unsoy, G., Yalcin, S., Khodadust, R., Mutlu, P., & Gunduz, U. (2012). Preparation of fluorescent IgG monoclonal antibody conjugated chitosan coated magnetic nanoparticles for cancer theranostics. Poster sunumu, *NANOTR VIII, 8th Nanoscience and Nanotechnology Conference & 3th World Congress IANM*, June, 25-29, Hacettepe University, Ankara, Turkey, pp-342.
3. Unsoy, G., Gunduz, G., Yakar, A., & Gunduz, U. (2011). Synthesis of iron-oxide nanoparticles for targeted drug delivery and their characterization. Poster sunumu, *NANOTR VII, 7th Nanoscience and Nanotechnology Conference*, June 27-July 01, Sabancı University, Istanbul, Turkey, s.64.
4. Yalcin, S., Unsoy, G., Khodadust, R., Mutlu, P., Mumcuoğlu, D., & Gunduz, U. (2012). Cellular Internalization of Polyhydroxybutyrate (PHB) Coated Magnetic Nanoparticles in MCF-7 Cell Lines. Poster sunumu, *NANOTR VIII, 8th Nanoscience and Nanotechnology Conference & 3th World Congress IANM*, June, 25-29, Hacettepe University, Ankara, Turkey, pp-264.
5. Khodadust, R., Mutlu, P., Yalcin, S., Unsoy, G., & Gunduz, U. (2012). The Cytotoxic Analysis of Free Doxorubicin and Doxorubicin Loaded Dendrimer Coated Magnetic Nanoparticles on Sensitive and Doxorubicin Resistant MCF-7 Cell Lines. Poster sunumu, *NANOTR VIII, 8th Nanoscience and Nanotechnology Conference & 3th World Congress IANM*, June, 25-29, Hacettepe University, Ankara, Turkey, pp-262.
6. Yakar, A., Unsoy, G., Khodadust, R., Tansık, G., Keskin, T., & Gunduz, U. (2010). Preparation of PLGA and Chitosan-modified PLGA Coated Magnetite Nanoparticles. Poster sunumu, *NANOTR VI, 6th Nanoscience and Nanotechnology Conference*, June 15-18, Çeşme, İzmir, Turkey, s.477.
7. Keskin, T., Tansık, G., Yakar, A., Unsoy, G., Khodadust, R., & Gunduz, U. (2010). In vitro Cytotoxic Studies of Polymer Coated Magnetic Nanoparticles for Anti-Cancer Drug Delivery. Poster sunumu, *NANOTR VI, 6th Nanoscience and Nanotechnology Conference*, June 15-18, Çeşme, İzmir, Turkey, s.470.
8. Yakar, A., Tansık, G., Khodadust, R., Keskin, T., Unsoy, G., & Gunduz, U. (2010). Synthesis of Magnetic Nanoparticles as a Targeting System for Drug Delivery. Poster sunumu, *NANOTR VI, 6th Nanoscience and Nanotechnology Conference*, June 15-18, Çeşme, İzmir, Turkey, s.476.

PROJECTS INVOLVED

1. *METU - Gülhane Military School of Medicine Partner Project* (Researcher): Immunocytochemistry analysis of Doxorubicin loaded chitosan-coated magnetic nanoparticles on cancer cell line. BAP-08-11-2013-018.
2. *METU - Gülhane Military School of Medicine Partner Project* (Researcher): The in vivo cytotoxicity analysis of synthesized polymer coated magnetic nanoparticles prepared for targeted cancer therapy application purposes. BAP-08-11-2012-012.
3. *METU - TÜBİTAK* (Researcher): Idarubicin loaded magnetic nanoparticles synthesis and cytotoxicity analysis on MCF-7 breast cancer cell line. TBAG: 109T949, (2010-2012).
4. *METU Interdisciplinary Research Foundation Project* (Researcher): Suppression of *Survivin* gene expression in cancer cell line with siRNA loaded magnetic nanoparticles. BAP-07-02-2012-001.
5. *METU Interdisciplinary Research Foundation Project* (Researcher): Dendrimer coated magnetic nanoparticles application for drug targeting in cancer therapy. BAP-07-02-2010-06.
6. *METU Research Foundation Project* (Researcher): Biochemical characterization of recombinant 20S proteasome from *Tp.volcanium* and cloning of it's regulatory subunit gene. BAP-2005-07-02-00-17.

COURSES& CONGRESSPARTICIPATED

1. Applied Mesenchymal Stem Cell Course (Uygulamalı Mezenkimal Kök Hücre Kursu). *Dokuz Eylül University-Cellular Therapy and Regenerative Medicine Society*, February 2011, İzmir, Turkey.
2. *Ulusal Hücresel Tedavi ve Rejeneratif Tıp Kongresi*. (2011). February11-13, İzmir, Turkey.